TECHNISCHE UNIVERSITÄT MÜNCHEN

Physik-Department
Lehrstuhl für Funktionelle Materialien
Forschungsneutronenquelle Heinz Maier-Leibnitz

Material Selection of UMo Fuel for Research Reactors: Swift Heavy Ion Irradiation Studies

Hsin-Yin Chiang, M.Sc.

Contents

Abstract

In order to optimize the irradiation performance of uranium molybdenum (UMo) fuel, an investigation of material selection is focused in the present work. Instead of using in-pile irradiation, swift heavy ion irradiation has been utilized to test the fuel stability. The reproducibility of swift heavy ion irradiation (^{127}I at 80 MeV) has been studied: an amorphous IDL, with the similar structure as the one produced during in-pile irradiation, in a UMo/Al diffusion couple can be successfully reproduced. Furthermore, the U-Mo-Al interactions under swift heavy ion irradiation at different irradiation temperatures have been investigated using advanced characterization methods: Rutherford backscattering spectrometer (RBS), scanning transmission electron microscopy (STEM), and nano X-ray diffraction (nano-XRD).

In order to suppress the severe U-Mo-Al interdiffusion reactions, modifications of UMo fuels have been carried out by i) replacing the Al matrix with the alternative matrix material Mg and ii) applying a diffusion barrier between the UMo and the Al matrix using transition metals Ti, Zr, Nb, and Mo. Both modifications of the UMo fuel have been tested under swift heavy ion irradiation. In the investigation of the alternative matrix material, the UMo/Mg bilayers have been irradiation at 140°C and 200°C and then characterized using STEM and micro-XRD. Results show that using Mg as the matrix material the interdiffusion reaction and the amorphous region of the UMo fuel decrease in comparison to those in the UMo/Al bilayer. Besides, at the higher irradiation temperature, spinodal decomposition can occur at the UMo/Mg interface. In the study of applying a diffusion barrier, after swift heavy ion irradiation the UMo/X/Al trilayer (X = Ti, Zr, Nb, and Mo) has been characterized by RBS and micro-XRD. Atomic mixing at interfaces resolved by RBS indicates that Ti interacts strongly with UMo while Zr does that with Al as predicted by enthalpies of mixing. Micro-XRD reveals Ti and Zr as diffusion barrier might reduce the stability of γ-UMo. However, the formation of intermetallic AlX compounds which could detain further intermixing. The impact of the irradiation-induced phases on the properties of the UMo/X/Al trilayer along with the effectiveness of diffusion barriers will be present.

Chapter 1

Motivation

Fuel technology has been investigated in order to convert nuclear fuels of research and test reactors worldwide from a highly enriched uranium (HEU) fuel to fuels based on low-enrichment uranium (LEU). The fuel conversion program of the neutron source Forschungsneutronenquelle Heinz Maier-Leibnitz (FRM II) in Garching, Germany has been launched at 2003. FRM II has engaged on replacing its highly-enriched U_3Si_2 fuel (^{235}U content: 93 at%) to a low-enriched fuel ($\leq$50 at% [1]). Fuel conversion studies at FRM II aims on fuel modifications: the current geometry of the fuel element will be kept to avoid enormous costs and a long reactor shutdown. Therefore, developing U-based fuels with a high U density will be necessary to compensate the loss in the neutron flux and in the cycle length of a single fuel element.

The fuel currently used at FRM II consists of three layers: a fuel meat[1] sandwiched between cladding layers of AlFeNi[2]. The fuel meat is composed of a mixture of U_3Si_2 and Al powder embedded in an Al matrix and the overall U density is up to 3 g/cm^3. To conduct the fuel conversion by limiting the ^{235}U enrichment to less than 50%, the minimum U density inside the fuel meat of FRM II must exceed 8 g/cm^3 based on calculations. There are two types of fuel meat, the monolithic and the dispersed, can be potentially utilized in the fuel conversion of FRM II. The fuel meat of the dispersed type is heterogeneous and composed of U-based powders embedded in a matrix, which is similar to the fuel meat currently applied in FRM II. On the other hand, in the monolithic type the fuel meat is homogeneous and made of a single composition, e.g. U-based alloys. Due to the dissimilar compositions, the maximum producible fuel volume loading of the monolithic type and of the dispersed type are 100 vol% and 55 vol% [2], respectively. Note that the U density of a fuel meat is given as the bulk U density of the pure fuel materials times the fuel volume loading. In other words, in order to reduce the ^{235}U enrichment down to $\leq$50 at%, the U density of the dispersed type and of the monolithic type have to exceed 15 g/cm^3 and 8 g/cm^3, respectively. The framework of fuel conversion in FRM II focuses on reaching the U density $\geq$ 15 g/cm^3 so that either the dispersed or the monolithic type can be applied. Indeed, by applying the monolithic type the ^{235}U enrichment can be greatly less than 50 at%.

The highest U density, i.e. 19 g/cm^3 of the fuel material can be achieved by using

---

[1]The fuel meat denotes the part of fuel consisting of fissile isotopes.

[2]An Al alloy consists of Al (95.2-97.1 wt%), Fe (0.8-1.2 wt%), Ni (0.8-1.2 wt%), Mg (0.8-1.2 wt%), Cr (0.2-0.5 wt%), Mn (0.2-0.6 wt%), and Zr (0.06-0.14 wt%).

the pure U. However, the pure U at room temperature crystallizes in an orthorhombic structure (α-U) [3]. This anisotropic structure is not appropriate in terms of a nuclear fuel due to its poor resistance of radiation and thermal cycling damage [4]. Alternatives such as U-based intermetallic compounds can greatly raise the U density and some examples are shown in Table 1.1 [6, 7, 8]. However, only intermetallics with a U density $\geq 15 \ g/cm^3$ meet the requirements for reaching a dispersed U density of 8 g/cm^3. In-pile tests of U_6Mn and U_6Fe powder dispersed in an Al matrix revealed the poor irradiation stability via exhibiting a severe fuel deformation [9, 10]. This fuel deformation might result from the anisotropicity of their lattices (tetragonal structure)[3]. Accordingly, U-based intermetallics with a cubic structure (i.e. γ-U) are preferred in terms of nuclear fuels [12].

Intermetallics	U density (g/cm^3)	Crystal system
U_3Si_2	11.3	tetragonal
U_2Ti	13.7	hexagonal
U_2Mo	13.8	tetragonal
U_6Fe	17.0	tetragonal
U_6Mn	17.1	tetragonal

Table 1.1: A comparison between the current fuel in FRM II, i.e. U_3Si_2 [5], and the other possible candidates [6, 7, 8] has been made. This shows that using U-based intermetallics the U density can be greatly increased.

Transition metals such as Mo can form a U-Mo solid solution in the cubic structure (γ-UMo) with a high stability. Besides, Mo enables a high U density as shown in Table 1.2. U-Mo solid solutions (denoted as UMo) show a good irradiation behavior and therefore they are the material of interest in the international fuel developing community. The addition of 7 - 10 wt% of Mo in UMo has been found as the best compromise between a high U density and a good γ-U stability [13, 14, 15]. The advantages of the UxMo (x = 7 - 10 wt%) alloy are the followings:

1. UMo grains can perfectly accommodate non-solvable fission gases up to a high fission density;

2. the desired cubic γ-UMo phase is stabilized during in-pile irradiation;

3. this alloy allows a high U density of 8.5 g/cm^3 for UMo powders dispersed in Al [15] and about 16 g/cm^3 for monolithic UMo/Al foils [16].

A typical fuel element of UMo powder dispersed in an Al matrix is shown in Figure 1.1 where the fuel meat (UMo powder dispersed in an Al matrix) sandwiched with Al cladding.

However, several in-pile tests of fuel plates prepared with UMo powder dispersed in an Al matrix experienced severe swelling and pillowing which finally lead to rupture of the

---

[3]For materials crystallized in anisotropic system (e.g. BCT, HCP), under irradiation they will undergo prevalent irradiation growth, i.e. a shape change caused by the interaction of point defects with microstructural sinks [11].

Intermetallics	U-density (g/cm^3)
U4wt%Mo	17.4
U5wt%Mo	17.0
U8wt%Mo	16.0
U9wt%Mo	15.5
U10wt%Mo	15.3

Table 1.2: The U densities of UMo solid solutions with different Mo addition are listed.
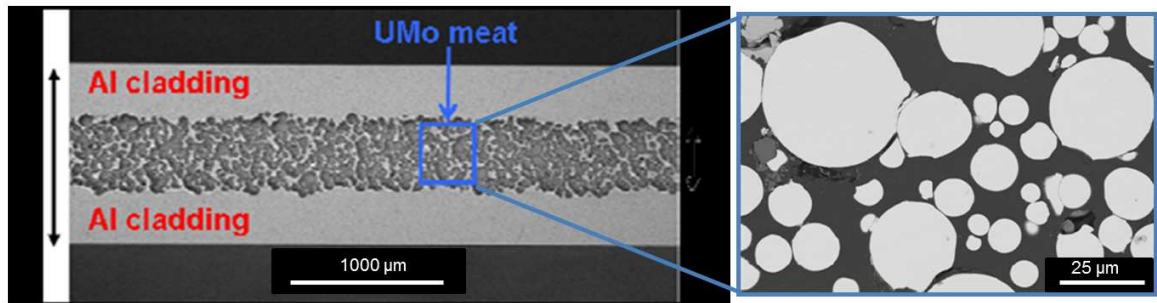

Figure 1.1: An overview of the UMo fuel: the fuel meat (UMo powders dispersed in an Al matrix) sandwiched by Al cladding [17]

fuel plate [18, 19, 20] as shown in Figure 1.2. One of the main reasons accounting for this abnormal swelling is the growth of an interdiffusion layer (IDL) at the interface between UMo and the surrounding Al matrix. The IDL is mainly composed of U-Al compounds and, most of time, exhibits an amorphous structure [21]. It has a smaller density than that of Al and of UMo, which can introduce a volume expansion and fuel swelling. Furthermore, because of the amorphous nature fission gases, e.g. Xe, Kr, cannot be accommodated inside the IDL and consequently they tend to accumulate along the outer mantle of the IDL. Figure 1.3 shows the correlation between the UMo-Al interactions and the burn-up. In the macroscopic images (the left column), the UMo powder is displayed as the dark gray rotundity, the white area denotes the Al matrix, and the gray layer is the IDL. On the other hand, the right column shows the microscopic images where the white rotundity denotes the UMo powder, the dark gray area is the Al matrix, and the gray layer is the IDL. At the low burnup[4], the IDL forms at the interface between the UMo powder and the Al matrix. The accumulation of fission gases at the IDL/Al interface appears as the black area. In contrast, fission gases are well-accommodated inside the crystalline UMo grains as the black spots as shown in the microscopic images. With the increasing burnup, the amount of IDL grows towards the UMo and the Al which limits the accommodation sites of fission gases. Consequently, several local accumulations of fission gases merged into a large hollow. This large hollow will induce the local hot-spots due to the inefficient heat transport among the UMo particle, the Al matrix, and the cladding and then the break down of thermal conductivity. Furthermore, the cladding temperature rises abruptly

---

[4]Burnup denotes the percentage of the initial fissile isotope inventory that has been consumed by fission.

which accelerating the cladding oxidation. After the first two or three cycles, the fuel plate deformation occurs and finally lead to rapture of UMo fuel as seen in Figure 1.2.
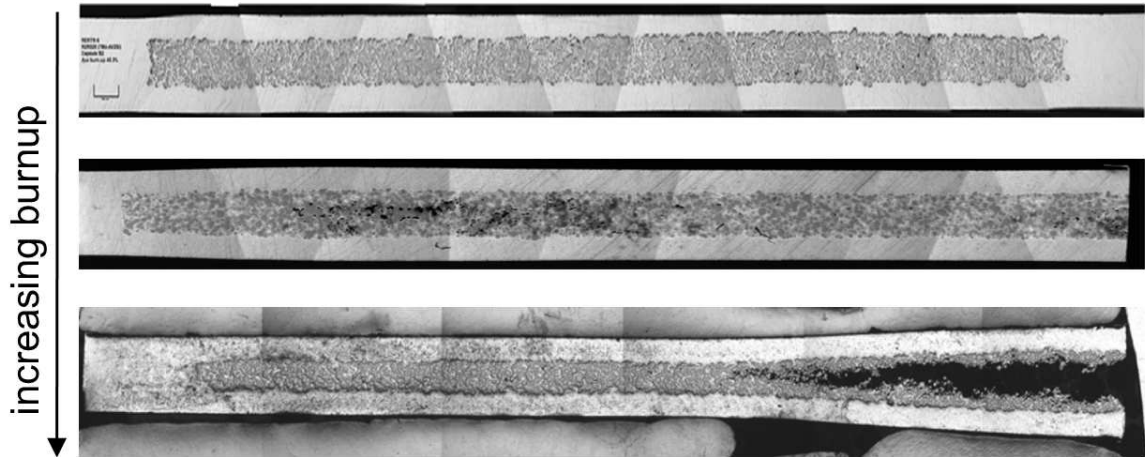
Figure 1.2: In-pile tests shows that with the increasing burnup the UMo/Al fuel can encounter a severe swelling and even rapture [19].
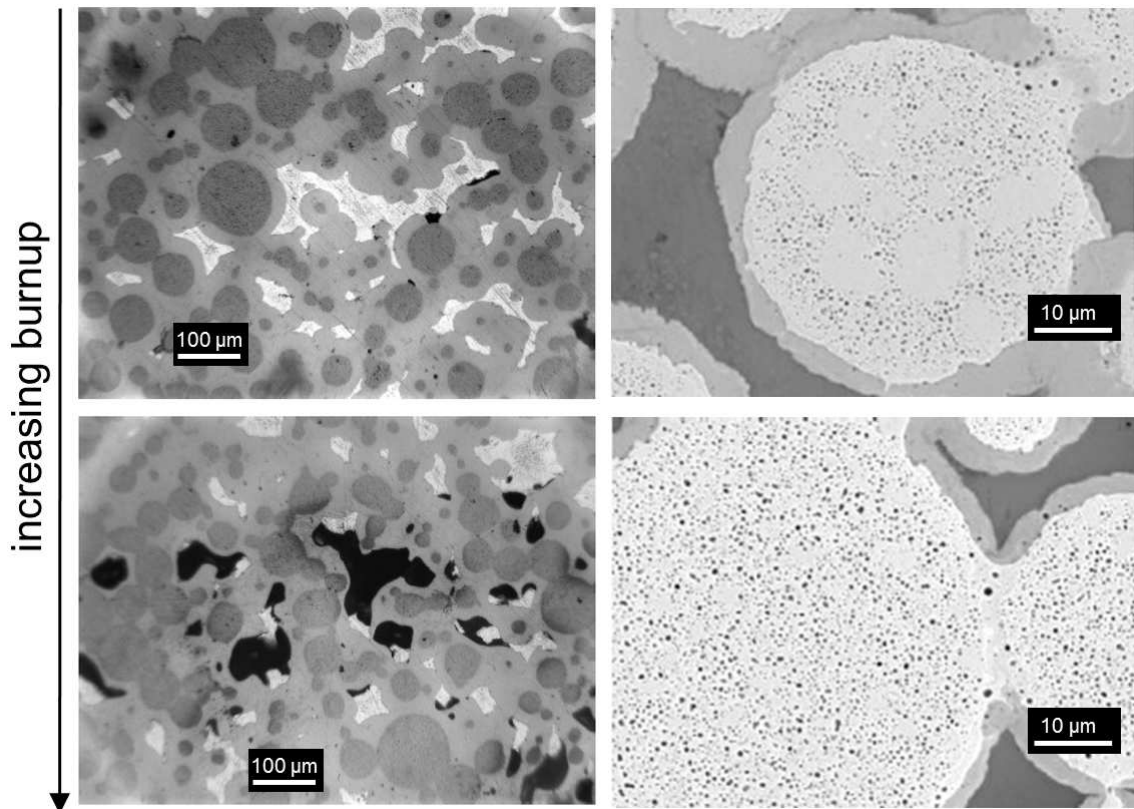
Figure 1.3: The UMo-Al interactions corresponding to the burn-up are shown in two magnifications [19, 24].

In order to optimize the UMo fuels, fuel modifications against the formation of IDL are necessary. Several ideas have been proposed to improve the UMo fuel performance:

1. *alloying the third element into UMo*: instead of using the binary U-Mo solid

solution, adding a third element such as Si [25] and Ti [26] to form a ternary U-Mo-X alloy to suppress the UMo-Al interactions;

2. *an addition to the Al matrix*: an Al matrix with few at% addition of other non-soluble elements such as Si in order to form a protective layer under heat and/or irradiation, i.e. Si-rich layer (SiRL) [27, 28], against the severe interdiffusion;

3. *applying directly a diffusion barrier between UMo and Al*: a direct barrier between UMo and Al to suppress their interactions [29, 30];

4. *using alternative matrix material*: replacing the Al matrix by another matrix material such as Mg which is less interactive with UMo [31].

Studies on *application of a diffusion barrier in the UMo/Al system* and *the alternative matrix material* will be presented in this thesis. The irradiation test of UMo fuels has been performed using swift heavy ion irradiation, e.g. ^{127}I at 80 MeV. It has been reported that swift heavy ion irradiation is able to reproduce the IDL, which has similar properties as the one produced during in-pile irradiation, at the interface of UMo and Al [30, 32]. Besides, the samples will not be activated during swift heavy ion irradiation so that the post-irradiation examination can be carried out with normal laboratory equipments. Moreover, the cost and the duration of swift heavy ion irradiation experiment are much less than that of in-pile irradiation.

Chapter 2

Scientific Backgrounds

In this chapter, theories and definitions utilized in this work will be introduced. First of all, the physics of fission will be mentioned to introduce which type of radiation damage a fuel element can experienced during in-reactor operation, which also explain the reason this work applies swift heavy ion irradiation in testing fuels. The second part includes the basic physics of ion-solid interactions and the atomic transport induced by ion irradiation. Furthermore, the microstructural modifications driven by ion irradiation such as spinodal decomposition and amorphization will be covered. Finally, the material selection including the criteria and thermodynamic consideration will be presented.

2.1   Fission and fission fragments

Fission is a form of nuclear transmutation which describes a compound nucleus decays by fissioning into two lighter nuclei and often these two nuclei are with comparable sizes. The stability of heavy nuclei against spontaneous fission is based on the short-range nuclear forces within the nucleus giving rise to a potential energy barrier and this fission barrier is typically 6 - 9 MeV in most heavy nuclei. Fission will take place only until the fission barrier has been overcome by adding a sufficient amount of energy to the heavy nucleus. A common scheme of fission is the heavy nucleus capture a neutron and then the binding energy of the neutron might be sufficient to overcome the fission barrier. For nuclides that can be induced to fission with neutrons of zero or very small kinetic energies, e.g. thermal neutrons, are referred to as fissile nuclides such as ^{233}U, ^{235}U, ^{239}Pu, and ^{241}Pu. On the other hand, for most heavy nuclides, the additional binding energy provided by a captured neutron is not sufficient to overcome the fission barrier. Their fission barrier can be exceeded by extra energy such as kinetic energy of the neutron. Nuclides that can be fissioned with fast neutrons are referred to as fissionable, e.g. ^{232}Th, ^{238}U, and ^{240}Pu. Although such fissionable nuclides do play an important role as nuclear fuels they are unstable to sustain by themselves a stable fission chain reaction. Therefore, fission in fissile nuclides is mainly focused.

A typical nuclear fission such as ^{235}U undergoes

$$_{0}^{1}n +_{92}^{235}U \rightarrow (_{92}^{236}U^*) \rightarrow \quad \text{fission reaction products}$$
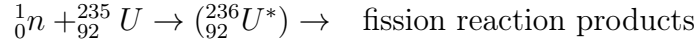
fission fragments FF (Figure 2.1), γ-, β-, neutrino- and neutron-radiation come along [33]. Their average values of the released energy are given in Table 2.1. In the case that fission is triggered by fast neutrons the mass numbers A of two fission fragments will be similar whereas for thermal fission the mass numbers will be around A = 95 and 137. The mass distribution of fission fragments in thermal fission is illustrated in Figure 2.2. The fission fragment nuclei (denoted as FF) produced by the fission reaction are both highly charged and highly energetic. They carry approximately 80% of the total fission energy ($E_{fission}$) in form of kinetic energy. Based on the conservation of momentum, fission fragment 1 (denoted as FF1) received the kinetic energy of $E_{FF1} = E_{fission} \cdot 80\% \cdot \frac{m_{FF2}}{m_{FF1}+m_{FF2}}$ where m_{FF1} and m_{FF2} are the mass numbers of fission fragment 1 and 2, respectively. The lighter fission fragment has averaged kinetic energy of 98 MeV and the heavier one receives 68 MeV. They slow down via collisions with adjacent atoms and lose their energy and charged (picking up electrons) in the process. This is the principal mechanism by which the fission energy eventually appears as heat generated in the fuel material. Besides, the fission products are inherently unstable and consequently emit γ, β, neutrino and neutron radiation [33, 36].

Reaction products	Energy (MeV)
fission fragments	167±5
neutrons	5
β-particles	8±1.5
γ-radiation (prompt from fission)	6±1
γ-radiation (from fission fragments)	6±1
neutrinos	12±2.5

Table 2.1: The average energies of fission fragments, neutrons, beta particles, neutrinos and gamma radiation released during ^{235}U fission are tabulated [34].

During fission, radiation damage[1] inside a nuclear fuel majorly results from collisions of fission fragments. The damages caused by fission fragments can be simulated by using ion beam techniques such as swift heavy ion irradiation. Ion beam techniques have been widely applied in simulating radiation damages because they are easy to operate, i.e. little or no activation, fast (e.g. a high fluence can be accumulated in hours or days), and cheap. In addition, they offer more experimental parameters to be manipulated during irradiation, e.g. temperature, dose, and energy. Swift heavy ion irradiation with the atomic number ranges from ^{84}Kr to ^{131}Xe and the incident energy around 70 - 90 MeV can well reproduce the damages induced by fission fragments in reactors.

---

[1]Lattice atoms are displaced by incident ions with knock-on process (e.g. primary, secondary knock-on) and defects such as vacancies, interstitials and other lattice disorder are formed around the ion trajectory (See 2.2.2).
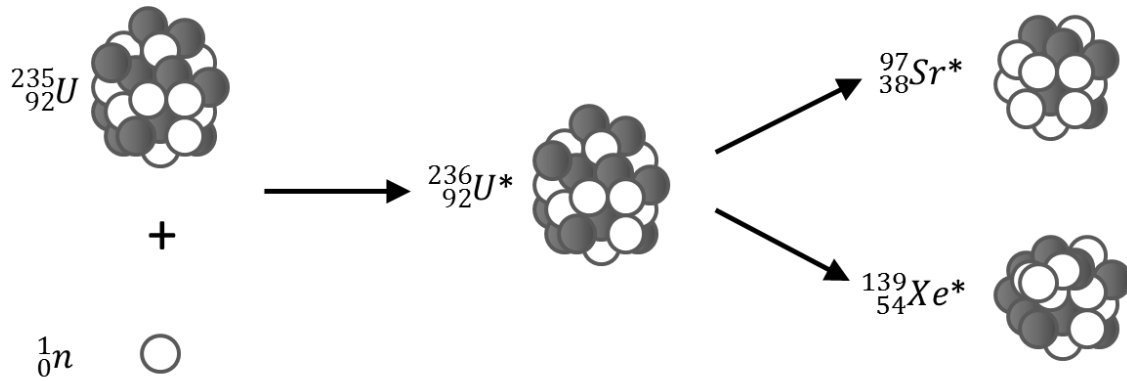
Figure 2.1: An example of fission
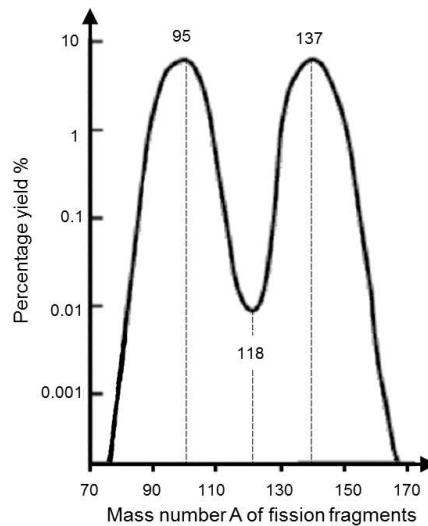
Figure 2.2: The mass distribution of fission fragments during thermal fission [35]

2.2   Swift heavy ion irradiation

2.2.1   Basic physics

When an energetic ion enters a solid, collisions of the ion with atoms and electrons take place in the target. The interactions between the incoming ion and the target, i.e. atoms and electrons, depend mainly on the ion velocity and, for near the surface (few nanometers), on the charges of the ion. Energy loss of the incident ion is determined by screened Coulomb interactions with the target atoms and electrons. There are two interactions describing the energy loss-rate $\frac{dE}{dX}$ of an incident ion in a target:

1. *Nuclear collisions*: a moving particle lost it energy due to elastic collisions per unit length traveled in the target. This interaction is called nuclear collision. When the ion velocity v is significantly lower than the Bohr velocity of the atomic electrons v_0, the ion carries its electrons and tends to neutralize by electron capture. At this velocity regime, elastic collision with the target nuclei, so called

nuclear energy loss (i.e. nuclear stopping) dominates. Nuclear collisions involve large energy discrete losses and significant angular deflection of the ion trajectory. This process accounts for the lattice disorder by displacements of atoms in the lattice.

2. *Electronic collisions*: electronic collision describes a particle excites or ejects atomic electrons by its energy loss. As the ion velocity increases, energy loss by nuclear collisions diminishes as $\frac{1}{E}$ where E is the energy of the incoming ion. Electronic energy loss considering inelastic collisions becomes the main interaction. In the low-ion-velocity regime from $v \sim v_0$ to $Z_1^{\frac{2}{3}} v_0$, the electronic energy loss is approximately proportional to velocity or $E^{\frac{1}{2}}$. At high velocities $v \gg v_0$, the charge state of the ion increases, and finally the ion is fully stripped of its electrons. Electronic collisions involve much smaller energy losses per collision, negligible deflection of the ion trajectory, and lattice disorder.

The energy-loss rate dE/dx can be expressed as

$$\frac{dE}{dx} = \frac{dE}{dx}|_n + \frac{dE}{dx}|_e \tag{2.1}$$

where the subscripts n and e denote nuclear and electronic collisions, respectively.

As the energy of incoming ions is completely deposited into the target, the ions stop at the depth R. The penetration depth R, it can be determined by the rate of energy loss along the path of ion,

$$R = \int_{E_0}^{0} \frac{1}{dE/dx} dE \tag{2.2}$$

where E_0 is the incident energy of the ions. The main parameters determining the range or energy-loss rate are the energy E_0 and the atomic number Z_1 of the incident ion and Z_2 of the substrate. As the ion enters the solid, the distance traveled between collisions and the amount of energy lost per collision are random. Therefore, ions with the same incident energy do not have the same range but a broad distribution in the depth where individual ions penetrate. It is due to statistical fluctuations in the number of collision processes. The distribution in ranges is referred to as the range distribution or range straggling.

2.2.2 Radiation damage

As the incident ion slows down and rests in a crystal, several collisions with the lattice atoms occur. In these collisions, atoms can be displaced from their lattice sites by sufficient energy transferred from the incident ions. Lattice atoms which are displaced by incident ions are primary knock-on atoms (PKAs). A PKA loses energy in both electronic and nuclear collisions as it slows down and it can displace other atoms by secondary knock-on, tertiary knock-on, etc., and thus a cascade of atomic collisions form. This cascade leads to a distribution of vacancies, interstitial atoms and other lattice disorder around the ion tracks. This is so-called radiation damage. Radiation damage theories are based on the assumption that a lattice atom is struck by an energetic ion or recoiling target atom must receive a minimum amount of energy in the
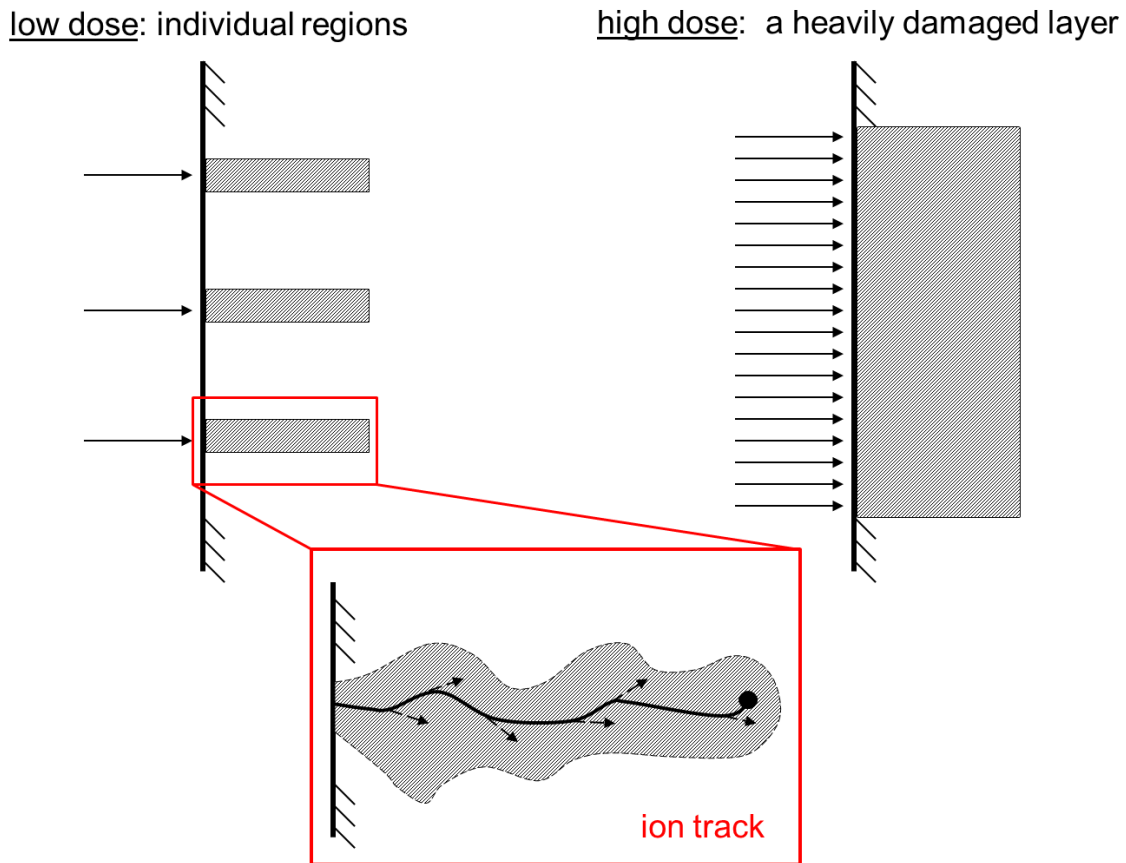
Figure 2.3: A schematic representation of the disorder produced by heavy ion irradiation. At low doses, the highly disordered regions around the tracks of the ions are spatially separated from one another. The volume of the disordered region is determined primarily by the stopping point of the ion and the range of the displaced lattice atom (dashed arrows). At high doses, the disordered region starts to overlap and finally a heavily damaged layer forms [37].

collision to be displaced from its lattice site. As the number of incident ion increases, the individual disordered regions begin to overlap. At some point, a heavily damaged layer is formed as shown in Figure 2.3.

Displacement energy and Frenkel pairs   The threshold energy to displace a lattice atom is called displacement energy E_d. When the energy transferred to the lattice atom is less than E_d, the struck atom undergoes large-amplitude vibrations around its lattice site. The vibrational energy of the struck atom is quickly shared with nearest neighbors and becomes a localized source of heat. When a displaced atom leaves a vacancy and then occupies an interstitial site in lattice, this vacancy-interstitial defect is called as a Frenkel pair.

A commonly used measure of irradiation damage is displacement per atom (dpa). A unit of 1 dpa means that, on average, every atom in the irradiated volume has been displaced once from its equilibrium lattice site. For an ion dose ϕ and an ion range R

, the approximated dpa in the implanted region is given by

$$dpa \cong \frac{\phi \cdot N_d^{1ion} \cdot M_{mol}}{\rho \cdot R \cdot N_A} \tag{2.3}$$

where N_d^{1ion} is the number of displacements per ion and the ion penetration depth R (cm) are provided by the SRIM calculations (see 3.4.1), ϕ is the ion fluence $(ions/cm^2)$, M_{mol} the target's molar mass (g/mol), ρ is the density of the target (g/cm^3) and N_A is Avogadro's constant.

Thermal spikes A spike is defined as a highly-dense cascade with a limited volume where the majority of atoms are temporarily in motion [38, 39]. These atoms have insufficient energy to cause further displacement. Therefore, the energy transfer will be at sub-threshold levels and shared between neighboring atoms. Afterwards, dissipation takes place as lattice vibrations or heat. After approximately 10^{-12} s, a dynamic equilibrium of the vibration energy distribution is reached in a form of Maxwell-Boltzmann function. This period of lattice heating is known as the thermal spike of collision cascades, and may last for several ps before being quenched to ambient temperature. As shown in Figure 2.4, inside the cascade a region with a depleted central core, essentially consisting of one large vacancy, and the outer shell is rich with interstitial atoms. In most metals the concentration of interstitial atoms gives rise to a pressure wave, with values up to 10 GPa. The region enclosing the interstitial atoms will be heated well above the melting temperature of the target, producing a thermal spike [40, 41]. Without a constraining solid lattice, the atoms are free to flow back into the depleted zone, annihilating a large fraction of the initial Frenkel pairs. As a result, most of the crystal structure will be repaired.

2.3   Ion-irradiation enhanced diffusion

Ion irradiation can effectively produce atomic displacements such as vacancies, interstitials, etc. These defects are highly concentrated into a small localized region in excess of the equilibrium value. The steady state of excess defect concentration depends on the balance between the rate of formation and of annihilation. Since the atomic diffusivity is proportional to the defect concentration, an enhancement in the diffusional process can be achieved by ion irradiation [46, 47, 48].

2.3.1   Diffusion mechanism

Interstitial   Solute atoms which are considerably smaller than the solvent atoms are incorporated on interstitial sites of the host lattice thus forming an interstitial solid solution. An interstitial solute can diffuse by jumping from one interstitial site to one of its neighboring sites as illustrated in Figure 2.5A. This is so-called interstitial diffusion mechanism. The interstitial atom does not need to wait for a defect to perform a jump so the diffusion for atoms migrating by the interstitial mechanism is independent of the defect concentration and the formation energy of defects. Consequently, the diffusion coefficient tends to be high.
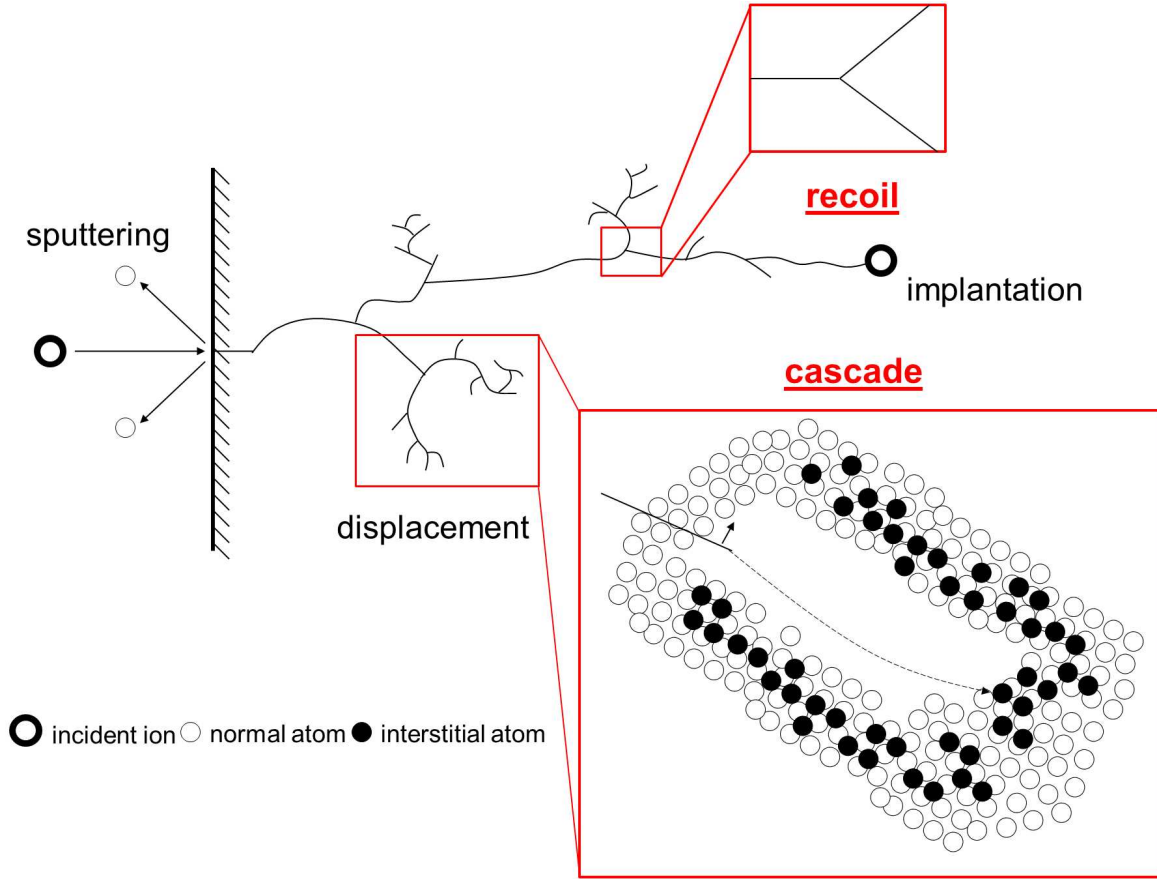
Figure 2.4: The ballistic interactions of an energetic ion with a solid [37].

Vacancy   The vacancy mechanism describes an atom diffuses by jumping into a neighboring vacancy (Figure 2.5B). Each atom moves through the crystal by making a series of exchanges with vacancies, which from time to time are in its vicinity. The atomic jump frequency Γ in vacancy mechanism is given by $\Gamma = f_V C_V \Gamma_V$ where C_V is the vacancy concentration, Γ_V is the vacancy jump frequency and f_V is a correlation factor [44]. The vacancy jump frequency Γ_V is proportional to $exp\left(-E_m^V/k_B T\right)$ where E_m^V is the vacancy migration energy. The atomic diffusion coefficient D can then be expressed as $D = f_V C_V D_V$, where D_V is the vacancy diffusion coefficient. This indicates that an enhancement in the vacancy concentration directly increases the atomic diffusivity.

During ion irradiation, in addition to a vacancy driven process diffusion is also enhanced by the formation and diffusion of other irradiation defects, e.g. self-interstitials, divacancies. A general statement for the atomic diffusion coefficient can be written in

$$D = f_V D_V C_V + f_{2V} D_{2V} C_{2V} + f_i D_i C_i + \cdots \tag{2.4}$$

where C_i is the concentration of interstitials, C_{2V} is the divacancy concentration and D_i and D_{2V} are the corresponding diffusion coefficients. As shown in Eq. 2.4, an irradiation induced enhancement in the vacancy, interstitial, or divacancy concentrations will result in a corresponding increase in D.
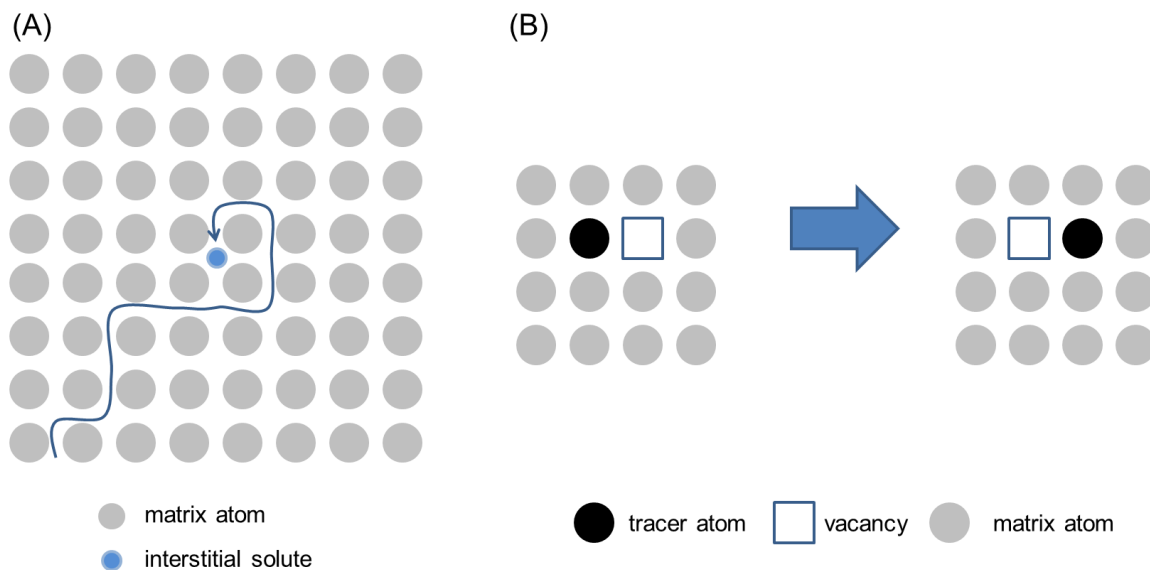
Figure 2.5: The sketches of diffusion mechanisms (A) interstitial and (B) vacancy mechanisms [49]

2.3.2 Ion beam mixing

Ion beam mixing is a phenomenon describing materials under ion irradiation substantially undergo atomic rearrangements such as atomic intermixing and alloying at the interface. At early stage of irradiation, ion tracks are isolated from one another and every incident ion can initiate a collision cascade surrounding the ion track. During irradiation atoms located in a cascade are mobile and will then experience rearrangement for a short period of time, resulting in an intermixed region near the interface [42]. In the early stage of ion beam mixing the interfacial reaction is considered to be composed of many localized regions. For higher doses a continuous intermixed region can be formed. With the increasing dose, the intermixed region grows at the interface as shown in Figure 2.6.

Figure 2.6: The correlation between ion beam mixing and the irradiation dose is sketched.

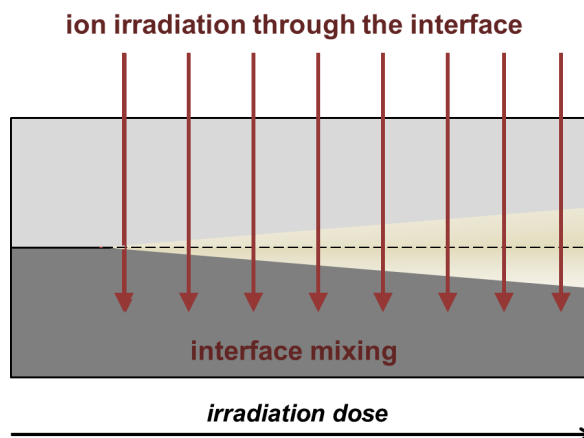**Ballistic mixing**   As an incident ion strikes a target atom near the interface, some of its kinetic energy will be transferred to the target atom. For high-energy collisions, the target atoms recoil far from their initial location. This single-collision process is known as recoil mixing. Nevertheless, atomic mixing induced by recoil mixing is small due to the limited probability of head-on collision, i.e. $\theta = 0°$. On the other hand, enhanced atomic mixing can occur in the multiple displacement process, i.e. collision cascade. Atoms in a collision cascade undergo several low-energy displacements and relocations. The resulting atomic mixing is referred as cascade mixing.

Collisional mixing factors in ion beam mixing has been gained by the use of embedded marker studies. The effective diffusion coefficient observed during marker ion mixing has been found to be proportional to ion mixing dose, ϕ, and the damage energy deposited per unit length, F_D. These results lead to the definition of an *effective mixing parameter k*, which is defined as $\frac{Dt}{\phi F_D}$ or simply as $\frac{Dt}{\phi}$ where D is diffusion coefficient and t is the irradiation duration [43].

Thermodynamic effects   The importance of chemical or thermodynamical factors in ion beam mixing has been found in the temperature-independent regime (e.g. T < 100°C), where the mixing is underestimated by ballistic mixing models. This result reveals the importance of chemical or thermodynamical factors, which are not considered in ballistic modes, in ion mixing when concentrated alloys are formed. For an A/B bilayer system, the chemical interdiffusion coefficient of an ideal solution is defined as [44]

$$\tilde{D}_{AB} = D_A X_B + D_B X_A$$

where $\tilde{D}$ is the chemical interdiffusion coefficient, D_i is the intrinsic diffusivity and X_i is the molar fraction of element i. For example, in Xe ion-irradiated bilayers a linear relationship between $4\tilde{D}t$ and ϕ has been observed[45]. Furthermore, the heat of mixing can be taken as an indicator of the element's attractiveness to each other. The enthalpy of mixing ΔH_{mix} results from the chemical joining of A and B atoms and the formation A-B bonds during alloying. The more negative the heat of mixing, the greater the tendency to form an A-B alloy. The enthalpy of mixing ΔH_{mix} can be derived by using the Miedema model (Sec. 2.5.2).

2.3.3   Radiation enhanced diffusion (RED)

After the cascade lifetime ($t > 10^{-11}s$), the remaining vacancy-interstitial pairs can contribute to atomic diffusion processes. This process is called radiation enhanced diffusion (RED). When the primary point defects formed during irradiation are vacancies and interstitials, their concentration can be determined by the rate of formation and the annihilation by recombination or by diffusing to sinks (e.g. dislocations, grain boundaries). The rate equations of this balance between the formation and annihilation of defects are given by [47]

$$\frac{dC_V}{dt} = K_d + K_{th} - D_V C_V k_V^2 - \alpha C_i C_V \tag{2.5}$$

$$\frac{dC_i}{dt} = K_d - D_i C_i k_i^2 - \alpha C_i C_V \tag{2.6}$$

where K_d is the atomic displacement rate (i.e. dpa in Sec. 2.2.2), K_{th} is the rate of thermal vacancy creation, α is the vacancy-interstitial recombination coefficient, k_V^2 and k_i^2 are the fixed sink strength for vacancies and interstitials, receptively.

At high temperatures $(T \geq 0.6T_m)$, the defect mobility is sufficiently high so that the irradiation induced defects are annealed quickly[2]. The thermal equilibrium vacancy concentration is large compared with the irradiation-induced vacancy concentration, i.e. $K_{th} > K_d$. In this regime, temperature-driven diffusion dominates the diffusion process. Diffusion coefficient D is unaltered by irradiation and this diffusion process has an activation energy E_a of $E_f^V + E_m^V$ where E_f^V and E_m^V are the vacancy formation energy and the vacancy migration energy, respectively. At intermediate temperatures $(0.25T_m > T > 0.6T_m)$, where the steady-state concentration of mobile defects is due to irradiation, irradiation produced vacancies and interstitials begin to prevail the diffusion process (i.e. $K_{th} < K_d$). In this regime, the activation energy E_a is often close to zero and diffusion is dominated by radiation enhanced diffusion. At lower temperatures $(T \cong 0.25T_m)$, the concentrations of irradiation produced defects become high enough that recombination between vacancies and interstitials begin to dominate over diffusion to fixed sinks. The activation energy E_a for this diffusion is $\frac{E_m^V}{2}$. In this regime, diffusion is predominately due to interstitials. The correlation between D and $\frac{1}{T}$ is shown schematically in Figure 2.7 for different damage rates.
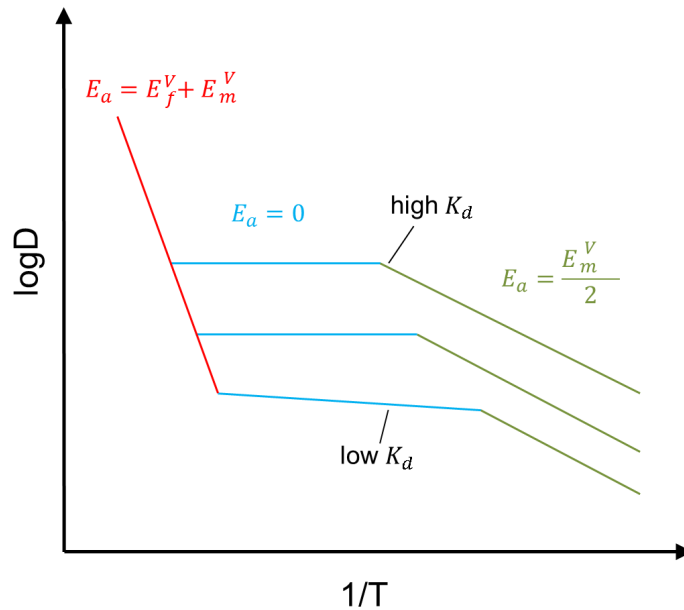
Figure 2.7: Schematic activation plot for diffusion in an irradiated metal. There characteristic regions in the plot are shown, as in the effect of atomic displacement rate [47].

2.3.4   Diffusion in thermal spikes

In high-density cascades, each of the atoms within the cascade volume can receive total energy transfers greater than 1 eV/atom. If the energetic atom motion is treated

---

[2]T_m denotes the melting point of the material.

as thermal motion with an averaged energy $k_B T$, the local temperatures can exceed thousands of degrees. This high temperature gives rise to thermal spikes (see Sec. 2.2.2). The collective movement of atoms in a thermal spike induced by bombardment of energetic ions can be considered as a diffusional process locally. Molecule Dynamics (MD) simulations point out that ion cascades exhibit liquid-like properties [50, 51]. The interdiffusion coefficient in a binary liquid system can be expressed by the Enskog kinetic model [52] as

$$D_{liq} = D_{kin} \left(1 - \frac{2\Delta H_{mix}^L}{k_B T} \right) \tag{2.7}$$

where D_{kin} is the MD-corrected Enskog kinetic diffusion coefficient and ΔH_{mix}^L is the compositional-dependent liquid heat of mixing. The term $\left(1 - 2\triangle H_{mix}^L/k_B T \right)^3$ is the thermodynamic factor and accounts for the non-ideal solutions. In this case, diffusion time is small (i.e. the lifetime of the spike), but the transient temperature is high. Diffusion in thermal spikes has no apparent activation energy and thermodynamic quantities (i.e. $\triangle H_{mix}^L$) play a role.

2.4   Ion-irradiation induced modifications

2.4.1   Amorphization

Ion beam techniques (e.g. ion implantation, ion mixing, and ion irradiation) can be used to produce amorphous metallic systems by irradiating a crystalline compound with inert ions. When the ion beam is terminated, the highly energetic state, induced by ion-atom interactions, begins to relax towards equilibrium within a short time (e.g. 10^{-10} s). This process results in similar effects as quenching the system from high temperatures. The effective quench rates of different surface processes are listed in Table 2.2.

It has been observed that thermodynamic factors are related to the glass-forming (i.e. amorphization) ability of a system. The immiscibility seems to be one of the prerequisites for amorphization. Brinhall et al. reported that irradiation-induced compounds with limited compositional range or solubility tend to become amorphous; in contrary to those compounds with wide solubility remain crystalline [54]. A correlation between the formation of amorphous phase and the compositional range is consistent with the concept of a threshold of defect concentration for amorphization. It is assumed that the structure would transform or relax into the amorphous state spontaneously if the irradiation could produce a critical defect concentration, i.e. whenever the total free energy of defect crystalline state is greater than that of the amorphous state. The increase in free energy is due to the inability of the compound to exist in equilibrium

---

[3]The term $\left(1 - 2\triangle H_{mix}^L/k_B T \right)$ is similar to Darken's second equation $\tilde{D} = [D_1^* X_1 + D_2^* X_2] \left(1 + \frac{d\ln\gamma_1}{d\ln X_1} \right)$.

process	quench rate (°C/s)
melt quench	
splat	$10^5 - 10^8$
laser pulse	$10^9 - 10^{12}$
condensation	
vapor	
sputter	10^{12}
chemical	
particle irradiation	
ion bombardment	
ion implantation	10^{12}
ion mixing	

Table 2.2: Effective quench rates of surface processes [53]

outside the designated composition. In addition, it also has been stated that an amorphization can occur by ion mixing if the elements have different equilibrium lattice structures [55]. Naguib and Kelly proposed a rule of ionicity to predict the probability of amorphization [56]. This N-K rule of ionicity takes into account the response of solids to ion impact on the basis of bond-type, i.e. ionicity, as the criterion for amorphization in the A-B binary system:

$$ionicity = 1 - exp\left[-0.25\left(X_A - X_B\right)^2\right] \leq 0.1 \tag{2.8}$$

where X_A and X_B are the electronegativities of atoms A and B. This criterion is derived empirically based on the importance of bond type.

2.4.2   Spinodal decomposition

When irradiating an alloy having limited solubility or a miscible gap in the phase diagram, spinodal decomposition might take place and consequently changes the properties of the alloy (strength, ductility, etc.). Spinodal decomposition describes a solution of two or more components separating into distinct phases with different chemical compositions [57]. This mechanism differs from classic nucleation[4]: spinodal-decomposed phase separation is more defined and occurs uniformly throughout the material.

Spinodal decomposition can occur whenever a material transits into the unstable region of the phase diagram. The boundary of the unstable region is denoted as binode or coexistence curve which can be obtained by performing a common tangent of the free-energy diagram. Inside binode there is a region called spinode which corresponds to the negative-curvature region, i.e. $\frac{d^2G}{dc^2} < 0$ in the free energy diagram. The point where the binodal and spinodal meet is the so-called critical point.

A phase diagram containing a miscibility gap has been illustrated in the upper part of Figure 2.8 whereas the lower part is the schematic free energy curve of temperature

---

[4]Nucleation is a nonlinear instability that requires the formation of a large enough nucleus of the nucleating phase.

T_2. When the system is quenched from a high temperature T_1 in to a lower temperature T_2, an alloy with composition c_0 will become unstable and this corresponds to G_0 in the free energy diagram. Then small fluctuations in composition (α_1 and α_2) take place to decrease the total free energy. Consequently, "up-hill" diffusion occurs until the equilibrium compositions c_1 and c_2, correspond to the free energy minima, are reached. For compositions within the spinode, a homogeneous solution is unstable against microscopic fluctuations in density or composition, and there is no thermodynamic barrier against the new phase formation: the phase transformation is solely diffusion controlled. In comparison, if an alloy with composition of c'_0, i.e. outside the spinode, is quenched from T_1 to T_2, the alloy become metastable and small variations in composition will lead to an increase in free energy. In this case, the free energy can only be decreased by forming nuclei with a composition different from the matrix.
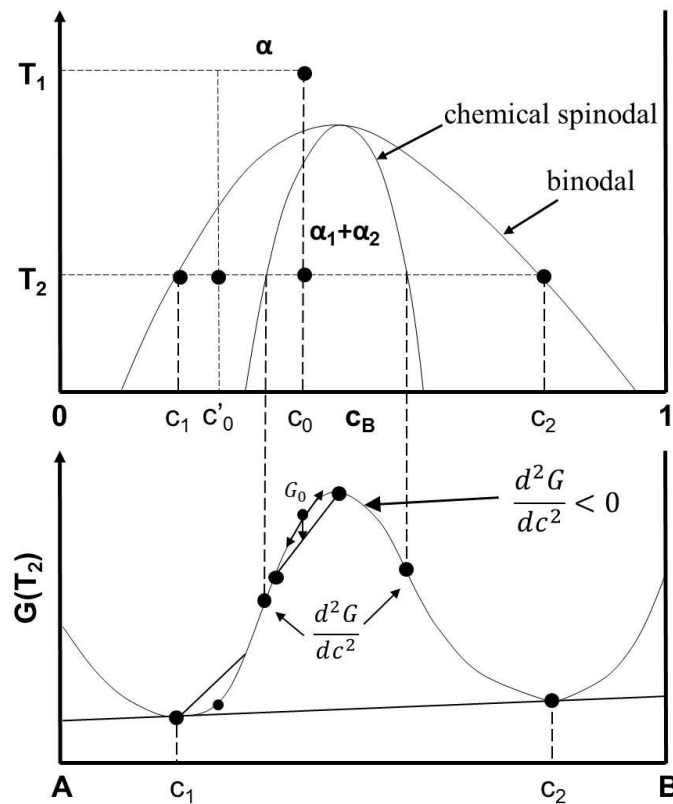

Figure 2.8: The A-B binary system with a miscible gap can experience spinodal decomposition when an alloy with a composition c_0 is quenched from T_1 to T_2. The corresponding free energy diagram at T_2 is illustrated as well [58].

2.5 Material selection

2.5.1 Criteria

Material selection for *applying a diffusion barrier into UMo/Al fuel* and *using an alternative matrix material* are the focus in the present work. Materials such as ceramics,

metals, and metalloids are the potential candidates and to be utilized in a nuclear fuel they should meet the following criteria:

1. thermal neutron cross-sections of materials should be within an acceptable value to minimize the loss of neutron flux;

2. materials should have the ability to suppress the UMo-Al diffusion reactions: inert or relatively less-reactive to UMo (or even to Al for the diffusion barrier);

3. materials should have suitable physical properties, e.g. ductility, thermal conductivity, thermal expansion coefficient, in order to accommodate high irradiation doses;

4. materials should have good processibility for the sake of fabrication;

5. materials should be reprocessed easily for fuel recycling;

In terms of the alternative matrix material, Cu and Mg have been considered due to their good physical properties and relatively low thermal neutron cross-sections (Figure 2.9). The influence of different matrix materials on neutron flux and begin of life reactivity have been studied. Results show that there is no significant difference between the use of Mg and Al as the matrix material. However, Cu has a higher absorption cross-section, including a number of resonances, in comparison to Al and Mg. This results in an increased absorption of thermal neutrons in the fuel, which disqualifies Cu from Criterion 1. The evaluation of Mg as the matrix material in the UMo fuel will be presented in Chap. 5.

As for the material of the diffusion barrier, transition metals meet all these criteria. Even though transition metals tend to form intermetallics with Al, yet with the vacant d shells they can form a stronger semi-covalent bond with Al to prevent further collisions. Ceramic materials such as ZrN and TiN have been often used as diffusion barriers due to their chemical inertness and high strengths. However, they are not qualified with respect to Criterion 3 and 5. Studies show that ZrN coating on UMo powder completely suppress the UMo-Al interactions, but with the limited ductility the ZrN coating was easily cracked during manufacturing and by irradiation-induced deformation [30]. Furthermore, ceramic coatings make the fuel reprocessing difficult by the inability of dissolving the ceramics protective layer. Metalloid material such as Si has been widely applied in UMo/Al fuels as the addition to matrix [29, 30] or as the third element in alloying [25]. Si as the diffusion barrier of the UMo/Al fuel has been studied by in-pile irradiation [59]. The result shows that with a limited wt% of Si, the UMo-Al interactions can be well-detained without sacrificing the overall physical properties. In the present work, the application of transition metals Ti, Zr, Nb, and Mo as the diffusion barrier in UMo/Al fuels will be discussed in Chap. 6.

2.5.2   Thermodynamic consideration: Miedema's model

It has been shown that chemical potentials have a certain contribution to radiation damages caused by fission fragments. Therefore, material selection of UMo fuels should
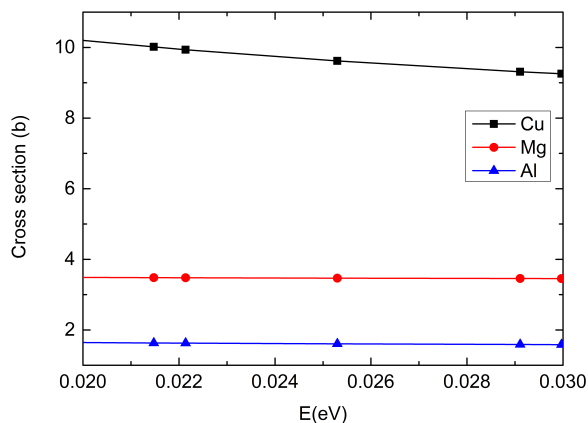
Figure 2.9: The thermal neutron cross-sections of Cu, Mg, and Al are illustrated [60].

take thermodynamics into account. Speaking of thermodynamic it is straightforward to consider the binary or ternary phase diagrams. However, one should keep in mind that phase diagrams only hold in an equilibrium status. The system of ion irradiation or in-pile irradiation are in a non-equilibrium status which makes it difficult to predict the possible irradiation-induced phases. Nevertheless, thermodynamics is essential in estimating the tendency of interactions and often has been applied as a guideline in the material selection of the UMo fuel.

A semi-quantitative model has been developed by Miedema et al. in 1970s to predict the phase formation using thermodynamics by combining the intrinsic properties of the constituent elements, i.e., the work functions, molar volumes and electron densities at the boundary of the Wigner-Seitz cell. In Miedema's semi-empirical model [61, 62], atoms are considered as blocks of the element. When two dissimilar atoms (blocks) were brought into contact, enthalpy effect occurs at the interface. In an A-B binary solid solution with elements A and B, an atom A is solved in infinite dilute in an excess of B atoms. At the A-B interface, the enthalpy effect takes place and is proportional to the contacting area. The quantity of area can be expressed by $V^{\frac{2}{3}}$, where V is the molar volume. In addition, work function φ is taken into consideration in the enthalpy change upon alloying. Work function φ is a potential felt by the outer electrons of the atom, which is similar to electronegativity [63]. When $\varphi_A > \varphi_B$ electronic charge will be transferred from B to A. This gives rise to a negative contribution to the enthalpy when A is solved in B. This enthalpy is proportional to $-(\varphi_A - \varphi_B)^2$, because an amount of electronic charge $|\Delta Z| \propto |\varphi_A - \varphi_B|$ is transferred under this potential difference with a corresponding enthalpy gain of $-|\Delta Z \times \Delta \varphi|$. The enthalpy is also contributed from the average electron density at the boundary of the Wigner-Seitz cell n_{ws}. This effect originates when solving an A atom in B a discontinuity appears in n_{ws}. The discontinuity is not allowed and should be smoothed at the boundary by bringing electrons to higher energy levels. The enthalpy change is proportional to $\left(n_{wsA}^{\frac{1}{3}} - n_{wsB}^{\frac{1}{3}}\right)^2$.

Miedema's model indicates that the quantities V, φ, and n_{ws} determine enthalpy changes upon alloying. The enthalpy ΔH^{inter} can then be expressed as

$$\triangle H^{inter} = \frac{V_A^{2/3}}{\frac{1}{2}\left(\frac{1}{n_{wsA}^{\frac{1}{3}}} + \frac{1}{n_{wsB}^{\frac{1}{3}}}\right)}\left\{-P\left(\triangle\varphi\right)^2 + Q\left(\triangle n_{ws}^{\frac{1}{3}}\right)^2\right\} \qquad (2.9)$$

where P and Q are experimental constants. Based on Miedema's model, the enthalpy of mixing can be calculated.

As mentioned, transition metals have been considered as the most promising candidate as the diffusion barrier in the UMo/Al fuels. To limit down the number of candidates, Eq. 2.9 has been utilized to calculate the enthalpy of mixing as shown in Table 2.3. The enthalpies of mixing with U, Mo, and Al of transition metals are denoted as ΔH_U^m, ΔH_{Mo}^m, ΔH_{Al}^m, respectively. Binary systems with positive enthalpies of mixing are not in favor of intermixing while systems with negative enthalpies imply the atoms tend to intermix with each other. According to the calculations using Miedema's model, four elements have been selected: Ti, Zr, Nb, and Mo. The evaluation of these materials will be present in Chap. 6.

(kJ/mol)	Sc	Ti	V	Cr	Mn	Fe	Co	Ni	Cu	Zn
ΔH_U^m	14	-1	3	-9	-17	-36	-73	-92	-22	-84
ΔH_{Mo}^m	50	-15	0	1	18	-7	-18	-32	68	17
ΔH_{Al}^m	-209	-165	-102	-73	-106	-77	-103	-123	-38	

	Y	Zr	Nb	Mo		Ru	Rh	Pd	Ag	Cd
ΔH_U^m	50	6	15	8		-122	-182	-207	1	-69
ΔH_{Mo}^m	127	37	-23	0		-55	-72	-57	152	88
ΔH_{Al}^m	-237	-218	-122	-65		-122	-181	-221	-24	

	Hf	Ta	W	Re	Os	Ir	Pt	Au	
ΔH_U^m	-7	12	4	-60	-113	-171	-260	-156	
ΔH_{Mo}^m	-18	-20	-1	-27	-53	-82	-123	14	
ΔH_{Al}^m	-221	-126	-54	-78	-112	157	-233	-101	

Table 2.3: The enthalpies of mixing of transition metals with U, Mo, and Al denoted ΔH_U^m, ΔH_{Mo}^m, and ΔH_{Al}^m as are calculated using Miedema's model [64, 65].

Chapter 3

Experimental Methods

The experiment methods in the present work includes sample preparation, fuel testing using swift heavy ion irradiation, post-irradiation examinations, and computer simulations. After swift heavy ion irradiation, several post-irradiation examinations have been performed to obtain an overall understanding of swift heavy ion irradiation induced modifications such as atomic mixing at the interfaces (by confocal microscopy, Rutherford backscattering spectroscopy, and energy-dispersive X-ray spectroscopy), irradiation-induced phases (using scanning electron microscopy, focused ion beam milling, X-ray diffraction, and X-ray fluorescence), and microstructural evolution (by scanning transmission electron microscopy). As for simulations, two binary collision approximation codes, i.e. TRIM and TRIDYN, have been applied to investigate the insight of swift heavy ion irradiation and the possible mechanisms dominating atomic transport.

3.1 Sample preparation

Sample preparation includes substrate cleaning and thin-film coating. Two materials Al and Mg have been applied as substrates. The Al substrate[1] has a purity of 99.9995% and a thickness of 0.5 mm. After tailoring into a dimension of $10 \times 10 \ mm^2$, the Al substrate is polished to a mirror-like surface[2]. Confocal microscopy characterization shows that the average grain size of the Al substrate is around 400 μm in diameter. The Mg substrate[3] has a purity of 99.95% and a thickness of 0.3 mm. After tailoring, the Mg substrate has a dimension of $15 \times 15 \ mm^2$. Due to the highly reactive nature of Mg, the surface of Mg was not treated.

The thin-film coating has been carried out by DC-magnetron sputtering and the sputtering device has been sketched in Figure 3.1 [66]. A sputter target (e.g. U8wt%Mo, transition metals) with a dimension of $122 \times 54 \times 10 \ mm^3$ is fastened to a copper plate with attached cooling tubes. To improve the thermal contact a graphite foil is inserted between target and plate. On top of the plate, an assembly of permanent magnets is

---

[1]Supplier: Alfa Assar

[2]The polishing process involves Si sand paper (up to 1200) and diamond paste polishing (down to 1 μm)

[3]Supplier: Alfa Assar

used to generate a magnetic field at the lower side of the target. The cooling is carried out by channels circulating through a flange cover. The whole setup is mounted inside a vacuum chamber which is evacuated to a pressure of 10^{-4} mbar. To initiate plasma reactions, argon gas is purged to reach a pressure of about 3×10^{-3} mbar and the sputtering process starts at the system power of 240 W. When a negative DC voltage is applied on the target arrangement, a few electrons in the argon gas are accelerated in the electric field and collide with other atoms. Once the electric field and the pressure meet the plasma ignition condition, the electrons will gain enough energy for further ionization. The presence of a magnetic field confines electrons and increases the discharge plasma density, which leads to a significant increase in erosion rate. This magnetron discharge in a closed magnetic field leads to a stable plasma. The plasma is burning right under the target in a toroidal geometry defined by the magnetic field; the argon atoms are accelerated towards the negatively charged target and knock target atoms out of the surface. These target atoms are falling down onto the substrate and rearrange themselves in a solid film.

The UMo thin film is produced by sputtering a depleted U8wt%Mo ingot upon a substrate (Al or Mg). For samples used in the diffusion barrier study, a layer of transition metals X is made by sputtering the metal ingot X upon an Al substrate and then subsequently a UMo layer is sputtered upon the X/Al bilayer. One should note that during the coating process, a great number of strains can be induced by DC magnetron sputtering technique. As seen in an annealing experiment, the sample prepared by DC-magnetron sputtering completely deformed as shown in Figure 3.2. This result indicates that the sample is highly strained prior to swift heavy ion irradiation and the induced strains can later enhance recrystallization process.
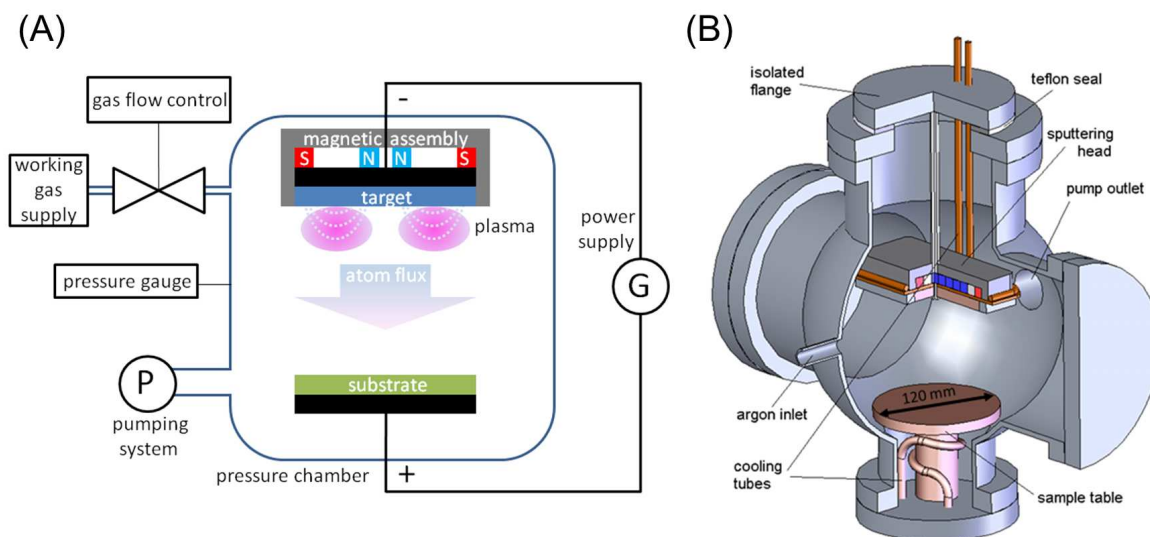

Figure 3.1: (A) basic assembly of a diode sputtering setup; (B) partial cut of the vacuum chamber with installed sputtering head and sample table that displays gas inlet and pump outlet. The chamber can be accessed only via the front and back flanges [66].
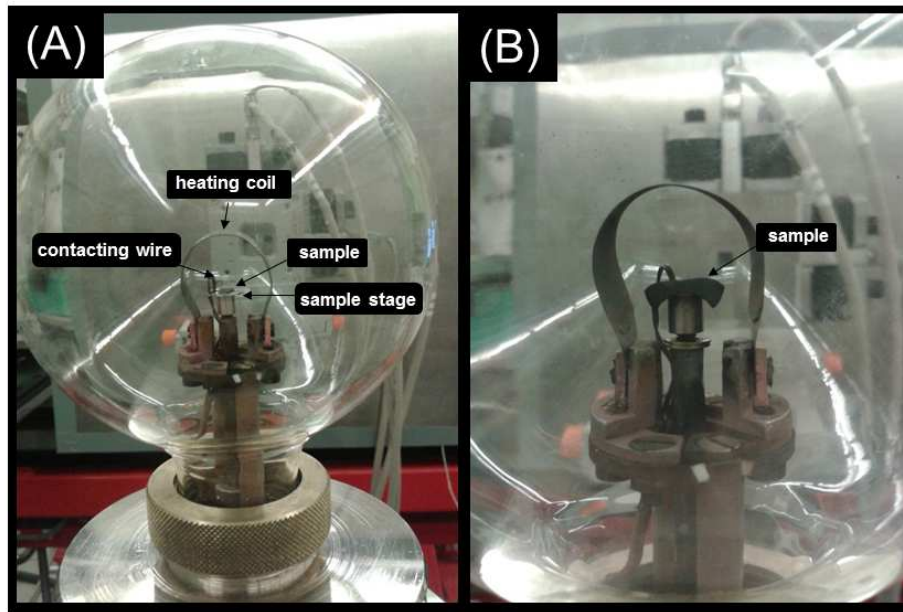
Figure 3.2: The annealing experiment has been performed in a glass chamber which consists of a heating coil with a contacting wire and a sample stage (A). The system pressure has been kept during the experiment at P = 10^{-3} mbar. After the heat treatment up to 480°C, the sample prepared by DC-magnetron sputtering exhibits strong deformation (B) due to the release of internal strains.

3.2   Swift heavy ion irradiation

Swift heavy ion irradiation experiment has been performed at the tandem accelerator Maier-Leibnitz-Labor (MLL) in Garching, Germany. The layout of MLL is shown in Figure 3.3. The accelerator laboratory is equipped with a negative-ion injector which allows to use a variety of ions. The ion injector consists of a Cs oven, an ionizer, and the ion source (e.g. ^{127}I in our case) as shown in Figure 3.4A. By heating up the Cs oven, Cs vapor is produced and deposited upon the ionizer which has been heated up to 1400°C. By applying an electric voltage V_1, Cs^+ ions are sputtered onto the the ion source by knocking out the target atoms ^{127}I and forming a Cs layer on the surface. During the knocked-out process, every target atom (i.e. the ion source) takes an electron from the outermost electron shell of the Cs atoms and becomes negatively charged. The charged target atoms (denotes as I^-) are then accelerated by the other electric potential V_2 and leave the ion injector.

Afterwards, I^- ions are further accelerated in the tank by the electric field by the positive terminal voltage $V_{terminal}$ applied in the middle of the accelerator tank and receive the kinetic energy $eV_{terminal}$ (see Figure 3.4B). As I^- ions pass through the middle of the tank, their charge state will be modified by the stripper, e.g. foil stripper[4], gas stripper[5]. Their final charge state (denotes as I^{n+}) depends on the kinetic energy, i.e. $eV_{terminal}$, the atomic number, and the stripping material. After passing the stripper, I^{n+} ions are accelerated by the terminal voltage $V_{terminal}$ again and have

---

[4]A thin graphite foil with an areal density of 4×10^{-6} g/cm^2.

[5]A volume filled with air at a pressure of $\sim 5 \times 10^{-4}$ mbar.

the final kinetic energy of $neV_{terminal}$. The I^{n+} ion beam usually consists of ions with different charge states and energies. With the analyzing 90° magnet, the ion beam is split into different lines and the assigned ion energy and charge state can be selected.
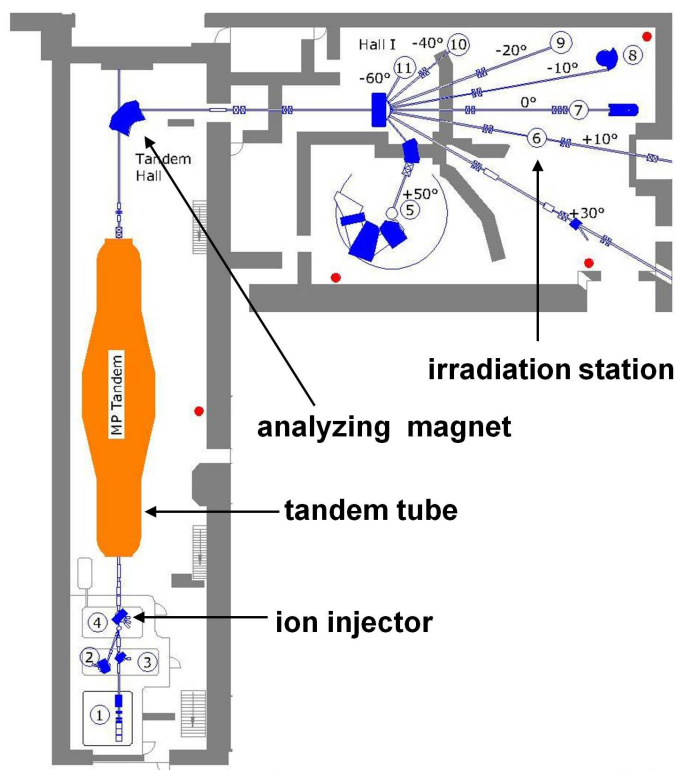

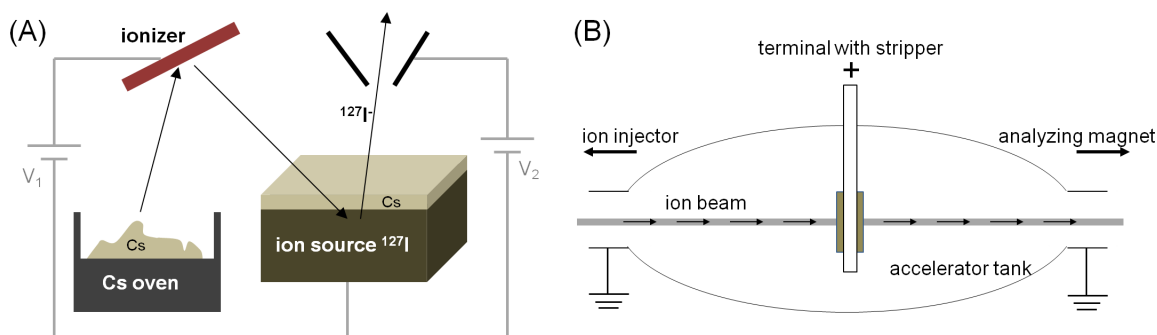**Figure 3.3:** The layout of the MLL accelerator facility in Garching [67]

Figure 3.4: (A) working principle of the ion injector; (B) tandem accelerator

As shown in Figure 3.3, the irradiation station locates at +10° beamline. The experiment chamber and the sample holders used for the irradiation experiment are shown in Figure 3.5. The experiment chamber (see Figure 3.5A) consists of a motor-driven sample holder (including a feedthrough, a cooling element, and a sample holder wheel), an external heating via an electric feedthrough, a fluorescent crystal for calibrating the beam position, and a cooling system with a water entry. The present work applies two types of copper-based sample holder: the sample holder wheel (Figure 3.5B) and the plain sample holder (Figure 3.5C). The wheel one has a capability to mount 7 samples and an alignment holder (the metal sheet with a hole in the center as shown in Figure

3.5B) at once and the cooling is done by water cooling. The other sample holder, the plain one (Figure 3.5C), is mounted at the position 5 in Figure 3.5A, where the fluorescent crystal is. This sample holder is able to mount 3 samples in the same time and the cooling system is managed by pressurized air which flows through a cooling tube on the back of the sample holder. To achieve a stable irradiation temperature, samples are mounted on the sample holder and fixed by an Al sheet and screws. Between the sample holder and the Al sheet, a Pt100 thermal sensor is mounted next to the beam spot for an accurate temperature measurement. Heating of the samples is accomplished on the one hand by the constant beam power of 5 W (which equals to 0.28 W/cm^2), and on the other hand by an electrical heating directly coupled to the copper holder, which can deliver a power up to 20 W.

Samples are irradiated perpendicularly to the surface by $^{127}I^{6+}$ ions at 80 MeV. The ion flux is set to 1.7×10^{12} $ions/s \cdot cm^2$ and the final ion fluence reached 1×10^{17} $ions/cm^2$ after 17 hours of irradiation. This ion fluence is equivalent to the low burnup (below 10% of the peak burnup) of the FRM II fuel element [30]. The irradiation has been carried out at 140°C and 200°C, which correspond to the maximum temperature in the meat of plate-like [69] and pin type fuel of research reactors during operation [70], respectively. The experimental setup is able to keep a designated irradiation temperature within a deviation of $\pm$ 2°C [32].

3.3   Characterization

3.3.1   Confocal microscopy

Confocal microscopy is an optical imaging technique which increases optical resolution and contrast of a micrograph by point illumination and a spatial pinhole [71]. It enables a reconstruction of 3D structures so that the morphology of specimens can be obtained. A schematic representation of a confocal microscope setup is shown in Figure 3.6. The light originating from an focal plane will pass through the confocal pinhole, whereas the out of focus light will be blocked. The light coming from the laser passes the illumination pinhole and is reflected by a dichroic mirror. Afterwards, the laser light is focused by an objective to a small spot on the sample. Olympus LEXT OLS4000 laser scanning confocal microscope has been applied in both ways. Examples of surface roughness measured by confocal microscopy: the virgin Al substrate, the UMo/Al bilayer, and the UMo/Mo/Al trilayer. The corresponding morphology has been processed by program Gwyddion are presented in Figure 3.7 in 3D [72].

3.3.2   Rutherford backscattering spectroscopy (RBS)

RBS has been widely applied for the near surface layer analysis of solids: a target is elastically bombarded with ions at an energy in the MeV range (e.g. 0.5 – 4 MeV), and the energy of the backscattered projectiles is recorded with an energy sensitive detector (Figure 3.8). This characterization allows the quantitative determination of the composition of a material and depth profiling of individual elements [73]. RBS measurements have been performed at a 3 MV tandem accelerator of the Max-Planck
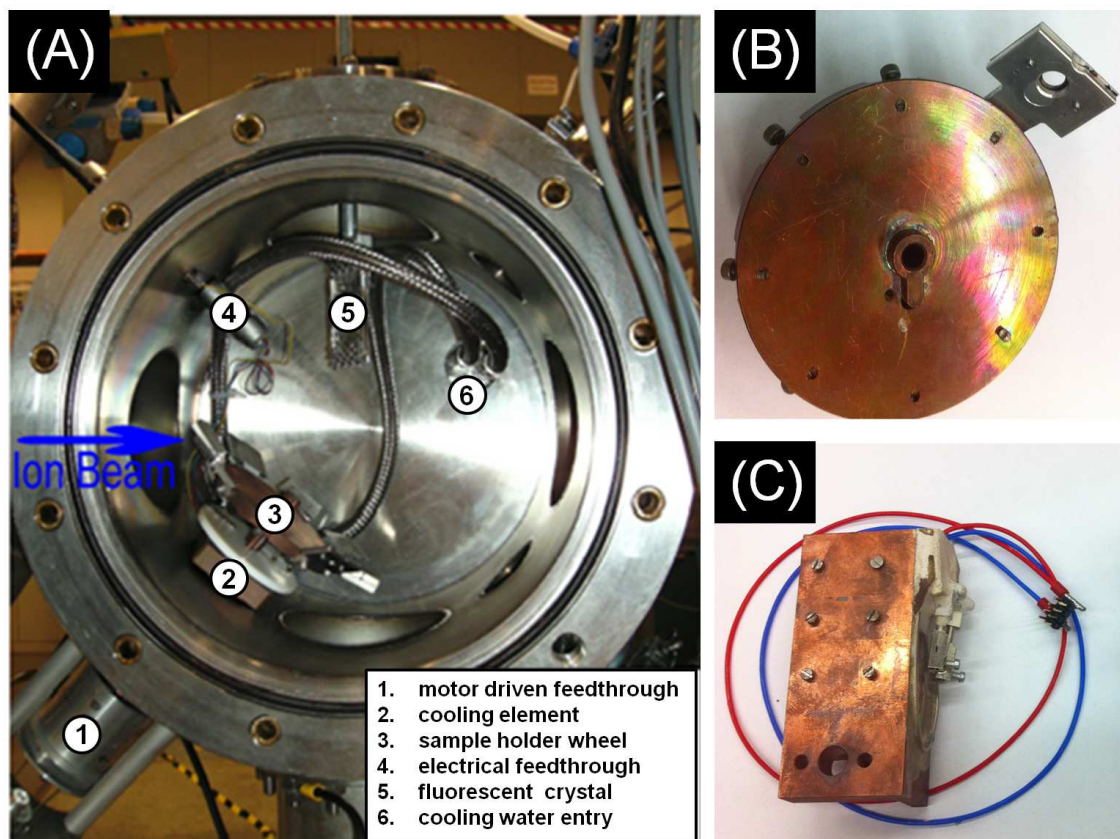
Figure 3.5: (A) the irradiation chamber consists of a motor-driven sample holder (including a feedthrough, a cooling element, and a sample holder wheel), an external heating via an electric feedthrough, a fluorescent crystal for calibrating the beam position, and a cooling system with a water entry [68]. There are two types of sample holder applied in the present work: (B) the wheel one and (C) the plain one.

Institut für Plasma Physik, Garching (Germany). Protons with 2.5 MeV or alpha particles with 7 - 8 MeV irradiate perpendicularly (incident angle $\alpha = 0°$) on samples with a beam size of $0.5 \times 0.5 \ mm^2$. The scattering angle θ is 165° and the final accumulated charge was 5 μC. Surface roughness of the sample has been measured by confocal microscopy. It is within an acceptable value, i.e. beyond the RBS resolution, which enables further data analysis of elemental depth profiles. The elemental depth profiles, i.e. atomic concentration of elements (%) versus areal density ($atoms/cm^2$), are processed by software SIMNRA [74]. The depth resolution of RBS using alpha particles has been calculated via program RESOLNRA [75] in Figure 3.9. It shows that samples with a thick UMo film, e.g. 4 μm, the resolution cannot be limited to less than 100 nm even though the applying energy is relatively high (e.g. 7 - 8 MeV).

3.3.3 Scanning electron microscopy (SEM)

SEM is a type of electron microscope that produces images of a sample by scanning with an focused electron beam. The electrons interact with atoms in the sample, producing signals which contain information about surface topography and composition. SEM
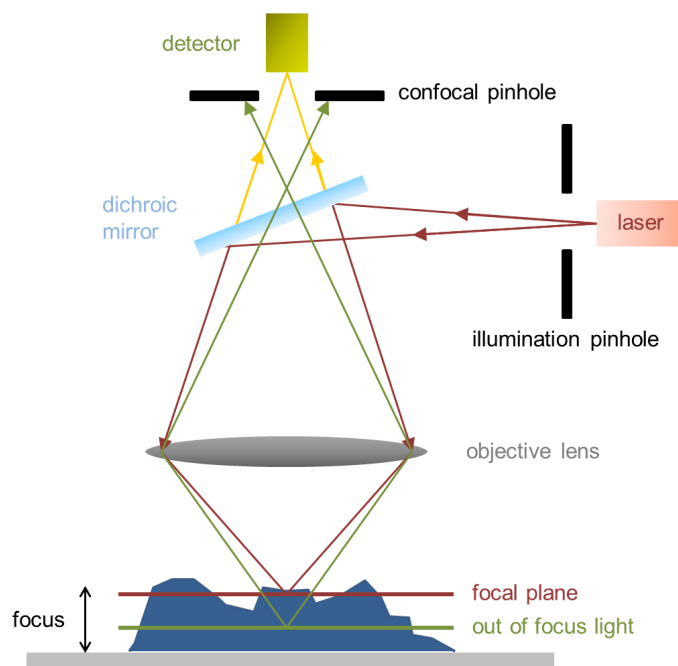
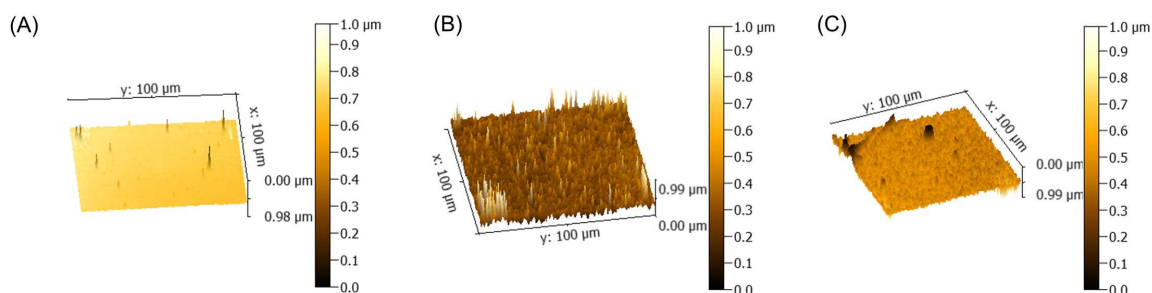**Figure 3.6:** The setup of confocal microscopy

Figure 3.7: Surface roughnesses of (A) the virgin Al substrate, (B) the UMo/Al bilayer, and (C) the UMo/Mo/Al trilayer have been measured by confocal microscopy and the corresponding surface morphology has been processed via program Gwyddion in 3D [72].

measurement has been performed with Zeiss EVO MA 25 equipped with a ultra-dry silicon drift detector by Thermo Fisher for EDX analysis (Sec. 3.3.8).

3.3.4   Focused ion beam milling (FIB)

FIB milling uses a focused beam of ions for imaging (at low beam currents) or for local deposition or milling (at high currents). The principle of FIB milling is that a Ga ion beam hits the specimen surface and sputters a small amount of material (see Figure 3.10). As the primary ion beam scans on the sample surface, the signal from the sputtered ions or secondary electrons are collected to form an image. This technique also allows precise TEM sections to be manufactured. If the region of interest is next to the surface, a protective layer must be deposited to prevent damage from the ion beam. This protective layer is made by introducing a metal-organic gas (e.g.
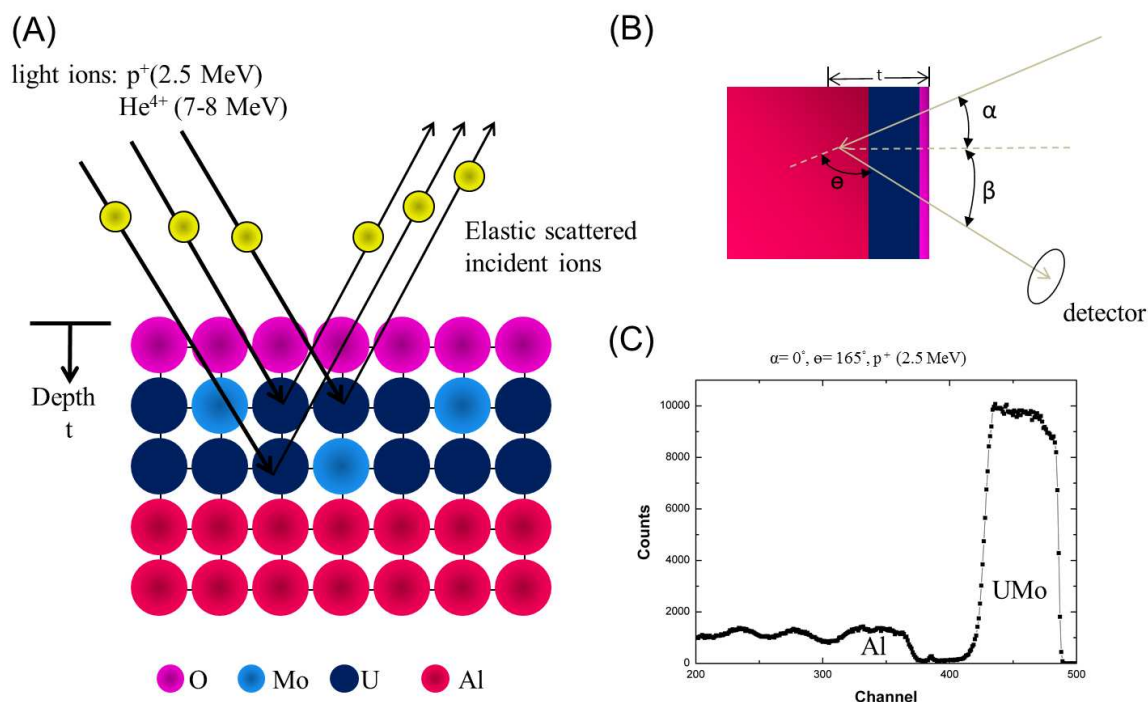
Figure 3.8: RBS measurement is based on the elastic collisions between probing ions, e.g. protons and alpha particles, and the target as shown in (A). After the collisions, the detection of the deflected probing ions (B) gives the corresponding spectrum, e.g. the spectrum of the UMo/Al bilayer (C).

Pt, C) next to the specimen, which decomposes in the ion beam and deposits the corresponding material on the sample surface wherever the ion beam is placed. Thin foils of the sample for X-ray diffraction (Sec. 3.3.5) and scanning transmission electron microscopy (Sec. 3.3.7) have been prepared by focused ion beam milling (FIB) on a Zeiss Crossbeam NVision40 with an accelerating voltage of 30 kV. The basic setup is sketched in Figure3.11A, which includes the sample stage, SEM and FIB columns, the gas injection for layer deposition (e.g. the carbon layer), and the micromanipulator which controls the contacting needle.

A thin foil (denoted as lamella) can be produced by fine trenching from the surface into the interface. The lamella preparation follows 6 steps [76]:

1. a carbon layer with a dimension of $20 \times 2 \times 0.5$ μm^3 is deposited on the region of interest at the sample stage of 54° (as 1 in Figure 3.11B);

2. ion beam mills two trapezoids (in a dimension of $20 \times 10 \times 10$ μm^3) with a slope[6] of 20° above and below the carbon layer (as 2 in Figure 3.11B);

3. a rectangle is milled on the right side of the carbon layer and a shape of lamella forms (as 3 in Figure 3.11B);

4. ion beam mills the bottom of the lamella at the sample stage of 0° (as 1 in Figure 3.11C);

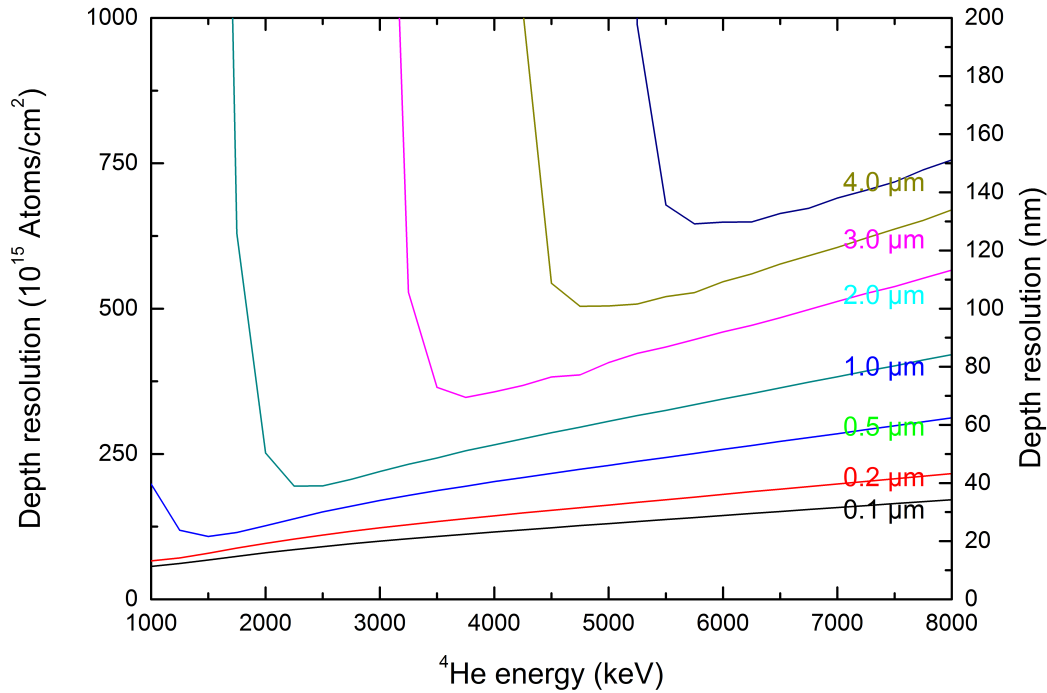[6]The slope is defined as the angle between the horizontal surface and the milled area

Figure 3.9: The depth resolution of UMo/X sample in RBS measurement using alpha particles has been calculated by program RESOLNRA [75]. This resolution has taken into account of electronic energy loss straggling, geometrical straggling, multiple scattering on the incident path and on the outgoing path, and the contribution from the detector resolution. The rise on the lower energy side mainly comes from the multiple scattering. The depth resolution scaled in nm is transformed from the depth resolution ($atoms/cm^2$) divided by the bulk density ($atoms/cm^3$).

5. a contacting needle driven by a manipulator system is moved to the lamella surface (i.e. the carbon layer) and afterwards the contacting needle is attached to the lamella surface by carbon deposition (as 4 in Figure 3.11B);

6. ion beam mills the left side of the lamella and then the lamella can be lifted up by the micromanipulator (as 2 and 3 in Figure 3.11C);

7. the so-produced lamella with a dimension of $10 \times 5 \times 2 \ \mu m^3$ is then attached to a copper grid by carbon deposition.

This lamella with a dimension of $10 \times 5 \times 2 \ \mu m^3$ is then characterized by micro X-ray diffraction (Sec. 3.3.5). For scanning transmission electron microscopy (Sec. 3.3.7), the lamella thickness has been further thinned by FIB milling down to 100 nm by the following steps [76]:

1. the lamella is well-aligned to the longitudinal axis in SEM at the stage of 55° (see Figure 3.12A);
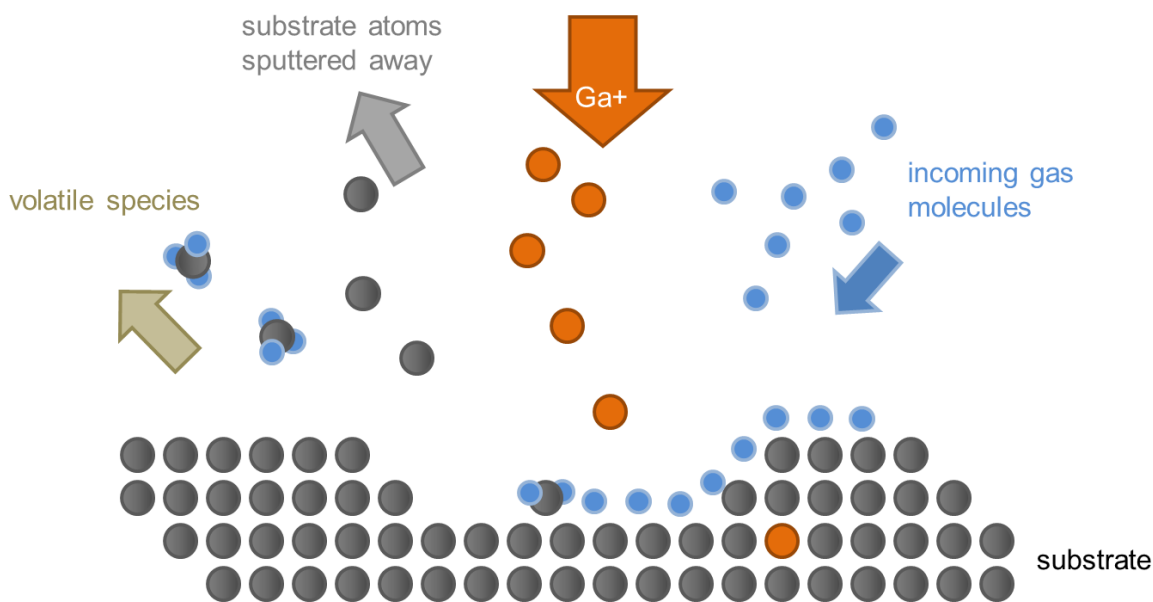
Figure 3.10: The principle of FIB milling is sketched: Ga ions interact with the incoming gas molecules to sputter the target or to deposit an extra layer above.
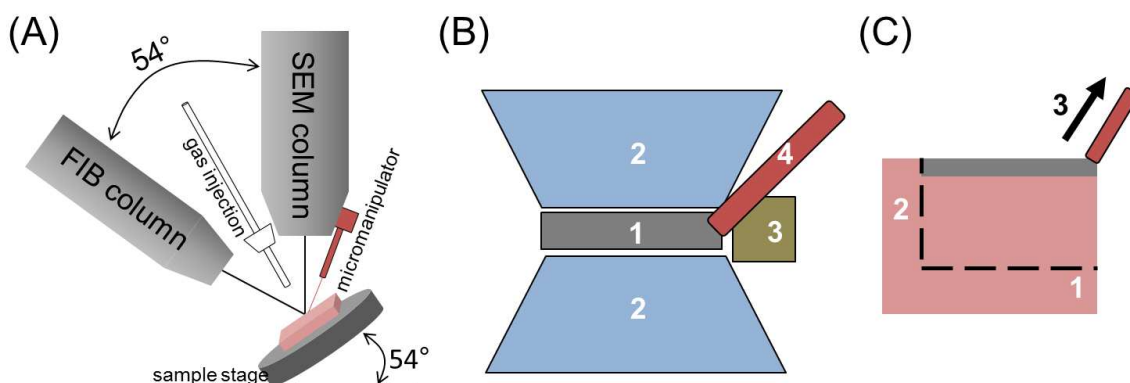

Figure 3.11: (A) the setup of FIB-SEM crossbeam; the thin film product is shown in (B) and (C) where the sample stage is at 54° and 0°, respectively.

2. a rectangular milling-object 1, shown as the rectangle in Figure 3.12A, is set at the bottom and the milling depth is set to 50% of the lamella height;

3. the milling-object 1 (the rectangle in Figure 3.12B) is then milled at the upper part of the lamella at the stage of 53° ;

4. a rectangular milling-object 2 with a 35% height and a 80% length of the milling-object 1 is set at the bottom at 55° (Figure 3.12C);

5. the stage rotates 180° and the milling-object 2 is milled from the top till the bottom (Figure 3.12D) until the lamella appears transparent in secondary electron mode (SE) in SEM;

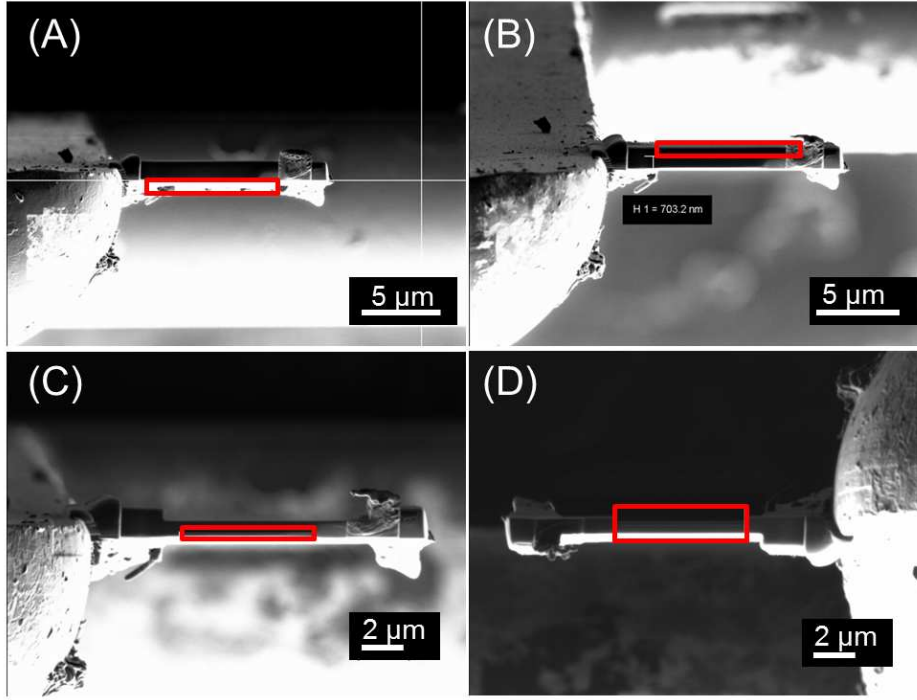6. a final polishing process at low kV must be performed to eliminate the damages created during FIB milling.

Figure 3.12: The procedure of FIB thinning

In addition to thin film preparation, FIB milling has been used to prepare cross sections which are afterwards characterized by SEM in secondary electron mode (SE).

3.3.5   X-ray diffraction (XRD)

To study the interfacial information of samples, e.g. phase identification, X-ray diffraction from synchrotron sources, a well-collimated X-ray beam with a size of sub-micron meter, has been applied. When choosing proper energies of X-ray at synchrotron sources, one should consider both the penetration depth of X-ray and the phase resolution[7]. The penetration depth τ of X-ray can be calculated by the linear absorption coefficient μ. Depending on the crystallinity of samples, penetration depth τ has a range of $\frac{1}{\mu} \leq \tau \leq \frac{2}{\mu}$. The value of μ is proportional to the material density ρ, which means the quantity of $\frac{\mu}{\rho}$, mass absorption coefficient, is a constant of a material and independent of its physical status (solid, liquid, or gas). The mass attenuation $\frac{\mu}{\rho}$ of different elements depends on the energy of X-ray. For a sample containing more than one element, the mass absorption coefficient is weighted by the average of the mass absorption coefficients of its constituent elements. If w_A, w_B, etc., are the weight fractions of elements A, B, etc., in the substance and $(\frac{\mu}{\rho})_A$, $(\frac{\mu}{\rho})_B$, etc., are the mass absorption coefficients , then the mass absorption coefficient $\frac{\mu}{\rho}$ of this substance is given by

$$\frac{\mu}{\rho} = w_A(\frac{\mu}{\rho})_A + w_B(\frac{\mu}{\rho})_B + ... \tag{3.1}$$

---

[7]Phase resolution denotes the peak spacing of phases, e.g. 2θ. With the increasing X-ray energies, peaks in a diffraction pattern tend to overlap with one and another. This will make the phase identification difficult especially in a multiple-phase diffraction pattern.

With the mass absorption coefficient, the linear mass coefficient μ can be calculated by simply multiplying the densities. For example, at 100 keV the penetration depth of X-ray inside U8wt%Mo alloy ranges from 276 μm to 553 μm.

The Bragg's law $n\lambda = 2d\sin\theta$ demonstrates that to acquire information about higher orders of reflection a shorter wavelength (i.e. higher energy) will be preferred where n is the order of reflection, λ is the wavelength, d is the lattice spacing, and θ is the Bragg angle. However, if the applied X-ray energy is too high, the phase resolution will be degenerated as with the increasing energies, the Bragg peaks in X-ray diffraction patterns become broader and begin to overlap with one and another. This peak overlap will lead to difficulties for the consequent analysis. The phase resolution can be simulated using program FindIt [77]. However, the Bragg's law $n\lambda = 2d\sin\theta$ demonstrates that to acquire information about higher order of reflection a shorter wavelength will be preferred where n is the order of reflection, λ is the wavelength, d is the lattice spacing, and θ is the Bragg angle. Therefore, an adequate X-ray energy is essential for X-ray diffraction measurement.

Nano-XRD Nano-XRD measurements have been performed at the ID22Ni beamline of the ESRF (European Synchrotron Radiation Facility in Grenoble, France [78]). The data are collected in transmission mode using a monochromatic X-ray beam with 29.6 keV selected by a cryogenically cooled Si (111). The X-ray beam focusing is performed with a pair of Kirkpatrick–Baez multilayer mirrors, providing a focal spot size of 0.1 $\times$ 0.15 μm^2 (hor. $\times$ ver.). For X-ray diffraction, a double-crystal Si (111) monochromator is generally used, lowering the flux to 10^{10} photons/s. Powder diffraction patterns are measured with a fast and low-noise two-dimensional CCD camera (FReLoN) [79] coupled to a fibre-optic taper. XRD linescans were performed with a counting time of 20 seconds for each obtained pattern. A linescan across the UMo/Al interface has been recorded at a 0.1 μm step width.

μ-XRD μ-XRD has been carried out at the beamline P06 of the synchrotron source PETRA III (Deutsches Elektronen-Synchrotron in Hamburg, Germany [80]). A primary energy of 21 keV was selected by means of a cryogenically cooled Si (111) double crystal monochromator. The beam was focused to 0.4 $\times$ 0.35 μm^2 (hor. $\times$ ver.) employing a Kirkpatrick-Baez mirror optic. The flux in the focused beam was $\sim10^{10}$ photons/s. A Keyence optical microscope was used for positioning of the thin foil UMo/X/Al cross-sections. XRD signals were recorded in transmission geometry with a 2k $\times$ 2k MAR sx165 CCD detector with 80 $\times$ 80 μm^2 effective pixel size and 165 mm scintillator screen diameter. X-ray fluorescence (XRF) signals were detected by means of a VORTEX EX Si-drift detector (SII Nano Technology) with 50 mm^2 active area and were applied to align the samples. Series of one-dimensional scans with 0.3 μm step size were carried out across the interfaces of the UMo/X/Al trilayer. An exposure time of 20 seconds per scan point was chosen in order to accommodate for the differences in atomic scattering factors.

For both XRD measurement, the collected two-dimensional diffraction patterns were first corrected for the dark and the flat field[8], and then converted into a 1D diagram via

---

[8]The dark and the flat field in X-ray diffraction denote the 2D patterns which are taken under the

the Fit2D software package [81]. For Rietveld analysis, the FullProf software package has been applied [82]. The sample geometry used in XRD characterization is illustrated in Figure 3.13.
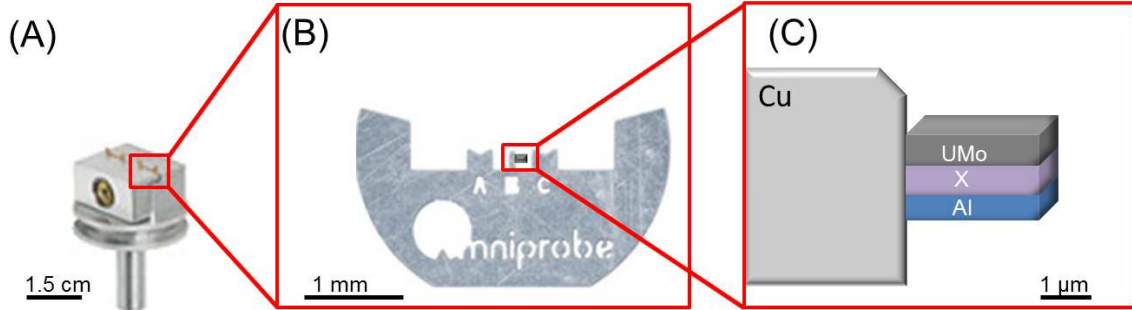
Figure 3.13: The sample geometry applied in XRD characterization is illustrated: a sample holder made of stainless steel (A) carries two copper grids (B). Upon the grid, a lamella produced by FIB milling is attached (C).

Intensities of X-ray diffraction peaks are proportional to the atomic scattering factor f, which describing the efficiency of X-ray scattering by electrons in an atom in a given direction $\frac{\sin\theta}{\lambda}$ (θ: the Bragg angle and λ: the wavelength of X-ray) and is proportional to the atomic number Z. For this reason, in X-ray diffraction the light elements of each trilayer are much less sensitive than the heavy elements such as U. As compared in Figure 3.14, f of U is about 9 and 4 times larger than those of Al and of Ti, respectively [83]. This was in particular disadvantageous with our sample ($\sim 2\ \mu m$ in thickness) exposed to a relative high X-ray energies.

3.3.6 X-ray fluorescence (XRF)

XRF is the emission of characteristic fluorescent X-rays from a material that has been excited by bombarding with high-energy X-ray or gamma ray. When the materials are excited by the bombardment of X-rays or gamma rays, the component atoms can be ionized and then generate characteristic fluorescence. XRF measurement was performed simultaneously with μ-XRD measurement at the beamline P06 of the synchrotron source PETRA III (Deutsches Elektronen-Synchrotron in Hamburg, Germany [80]) and the signals were detected by means of a VORTEX EX Si-drift detector (from SII Nano Technology) with 50 mm^2 active area. Series of one-dimensional scans with 0.3 μm step size were carried. XRF analysis has been processed by the software PyMca [85] to obtain the elemental concentration profile qualitatively.

3.3.7 Scanning transmission electron microscopy (STEM)

STEM combines the advantages of transmission electron microscopy (TEM) and SEM in the single technique. The basic setup of STEM is sketched in Figure 3.15A where BF denotes bright field detector, ADF denotes annular dark field detector ($\theta = 0.5° - 3°$),

---

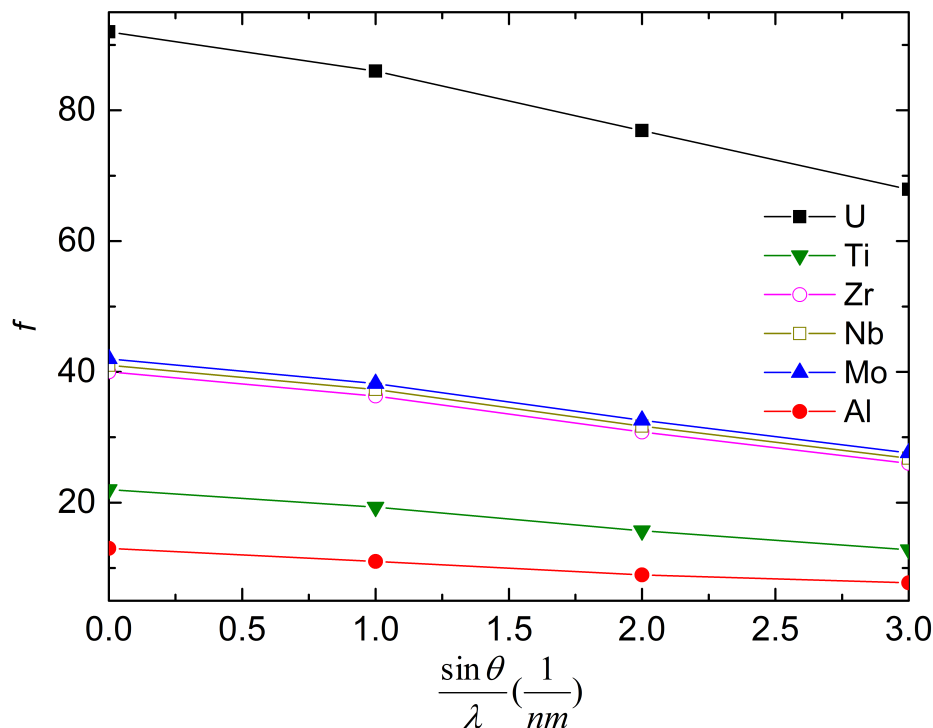circumstance of no X-ray intensity and full X-ray intensity, respectively.

Figure 3.14: The calculated values of f for various elements, i.e. U, Ti, Zr, Nb, Mo and Al of $\sin\theta/\lambda$ are illustrated [83]. It shows that f of U is around 9 and 4 times larger than that of Al and that of Ti, respectively.

and HAADF denotes high-angle annular dark field detector ($\theta > 3°$). The incident electron beam has been converged and then penetrates a specimen with a probe diameter less than 0.2 nm. Afterwards, the incident beam is scattered and then collected by HAADF detector at the relatively large scattering angles. HAADF detector collects both elastic and inelastic scattering which originate from Rutherford and electron-phonon interaction, respectively. The principle of atomic resolution STEM-HAADF imaging is sketched in Figure 3.15B. Since the inelastic scattering power of an atom is proportional to the square of its atomic number, i.e. $I \sim Z^2$, atoms with higher Z appear brighter in the STEM-HAADF images [84]. This Z-contrast imaging is a useful way of getting compositional information from complex structures. STEM using a FEI Titan operating at 300 kV has been applied on the thin films prepared by FIB milling with a final thickness of 100 nm. The local structural information has been characterized by electron diffraction in TEM mode.

3.3.8 Energy-dispersive X-ray spectroscopy (EDX)

EDX is an analytical technique used for the elemental analysis or chemical characterization of samples. It is based on X-ray emission of an excited electron inside the sample and allows to measure the elemental composition of the specimen. Note that EDX quantification can be challenging. Usually EDX quantification is processed using
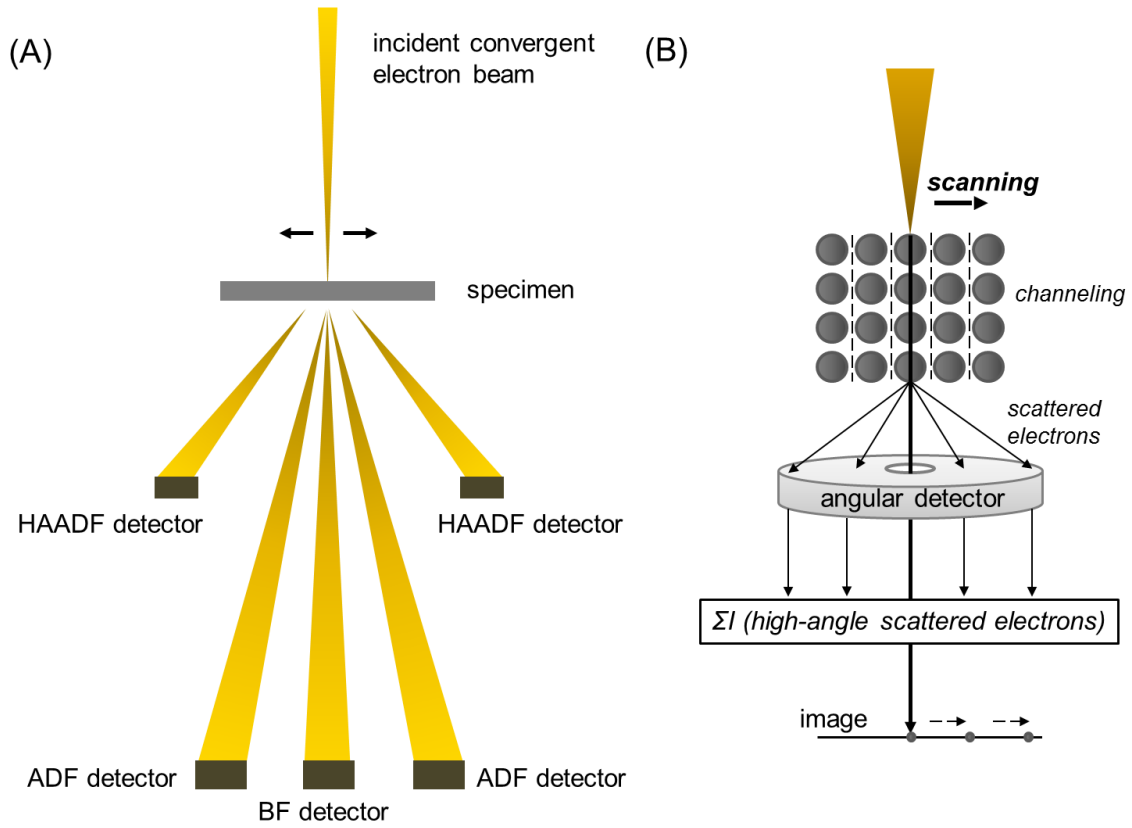
Figure 3.15: The schematic STEM (A) and the principle of STEM-HAADF imaging (B)

the corresponding software. However, the concentration coefficient K, which correlates the intensity of X-rays and the atomic ratio, applied in the software is generally not completely precise. To obtain the exact EDX quantification, an elaborated experiments will be needed to measure the concentration coefficient K. For example, in an A-B binary system K can be measured by using a A-B compound with a known stoichiometry and correlate the EDX intensity with the composition by the equation[9]

$$\frac{I_A}{I_B} = K_{AB}\frac{N_A}{N_B} \tag{3.2}$$

where I is the intensity measured in EDX and N is the number of atoms in a unit volume. Eq. 3.2 can be expressed in details as

$$\frac{I_A}{I_B} = \frac{(Q\omega a)_A}{(Q\omega a)_B} \cdot \frac{\varepsilon_A}{\varepsilon_B} \cdot \frac{N_A}{N_B} \tag{3.3}$$

where I_i is the peak intensity of i element, Q is the ionization cross-section, ω is the fluorescence yield, a is the intensity coefficient (i.e. $a = \frac{I_{K\alpha}}{I_{K\alpha}+I_{K\beta}}$), ε_i is the detector efficiency of element i and N_i refers as number of element i in volume. In the present work, the EDX quantification have been processed using the TIA software package

---

[9]This equation is a thin-film approximation, omitting the influence of absorption and fluorescence of X-ray.

so one should keep in mind that the elemental concentration can be biased. EDX measurement has been performed together with STEM using a FEI Titan operating at 300 kV.

3.4 Simulations

Computer simulations have been widely applied to describe the slowing down and the scattering of energetic ions in solids. The Monte Carlo simulation based on binary collision approximation (BCA)[10] has been exploited for studying the swift heavy ion irradiation. The input thicknesses Δh of sputtered layers are given by $\Delta h = \frac{\Delta m}{\rho}$ where Δm is the mass difference after sputtering and ρ is the density of the sputtered material, e.g. $\rho_{U8wt\%Mo} = 17.7 \ g/cm^3$.

3.4.1 The stopping and range of ions in matter (TRIM)

TRIM [86] has been developed to determine ion range and damage distributions as well as angular and energy distributions of backscattered and transmitted ions. This program provides high computer efficiency while still maintaining accuracy. TRIM also gives the amount of nuclear energy deposited in the primary collisions and recoil events. When a single ion goes into the target, the ion is assumed to change the direction as a result of binary nuclear collisions and move in straight free-flight-paths between collisions. Its energy is reduced as a result of nuclear and electronic energy losses and the subcascades are generated by recoiling lattice atoms along the ion trajectories. Displaced target atoms will remain displaced when the collisional energy is sufficient to move the target atom far enough away from its lattice site to prevent spontaneous athermal recombination with its vacancy. Recombination of point defects can also occur during subsequent irradiation when damage region overlap. However, this recombination is not considered in TRIM: the total number of target displacement shown in TRIM only indicates the number of lattice atoms experienced displacement without considering their final location. Therefore, the actual number of displaced atom remaining in the lattice will be smaller than the calculated value. Besides, TRIM always consider the collision is made on a fresh target, i.e. no collision history recorded from the previous collisions. Note that in TRIM calculations, the target is considered amorphous with atoms at random locations, and thus the directional properties of the crystal lattice are ignored[11].

TRIM calculations have been used in the present study to predict the mean penetration depths of ^{127}I ions at 80 MeV and the stopping powers along the ion trajectory. The calculations apply the *Detailed calculation with full damage cascades* mode using 10000 ions. In UMo, TRIM calculations show that the average penetration depth is 5 μm as shown in Figure 3.16A. Due to the extremely high incident energy of ^{127}I ions, most of the incoming energy has been dissipated via electronic stopping power and the maximum nuclear stopping power occurs at the depth of 4.9 μm (Figure 3.16B).

---

[10]There are three major BCA codes TRIM, TRIDYN, and MARLOWE.

[11]Among the three BCA codes, only MARLOWE is able to take the crystal structure into consideration.

For samples with a UMo film less than 2 μm, incident energy lost by the nuclear collisions is almost negligible. As for Al (Figure 3.17), due to the smaller density, the average ^{127}I ions penetrate further in Al than in UMo and the ion range is 12.8 μm given by TRIM calculations. The maximum nuclear stopping power occurs at 12.5 μm. In the case of Al, the ion range of ^{127}I is 18.5 μm and the maximum nuclear stopping power appears at 18.2 μm as shown in Figure 3.18. The information about ion range and stopping power distribution given by TRIM calculations are essential and after swift heavy ion irradiation experiment: to ensure the interfacial interactions during irradiation and understand the physics of material modifications induced by swift heavy ion irradiation.
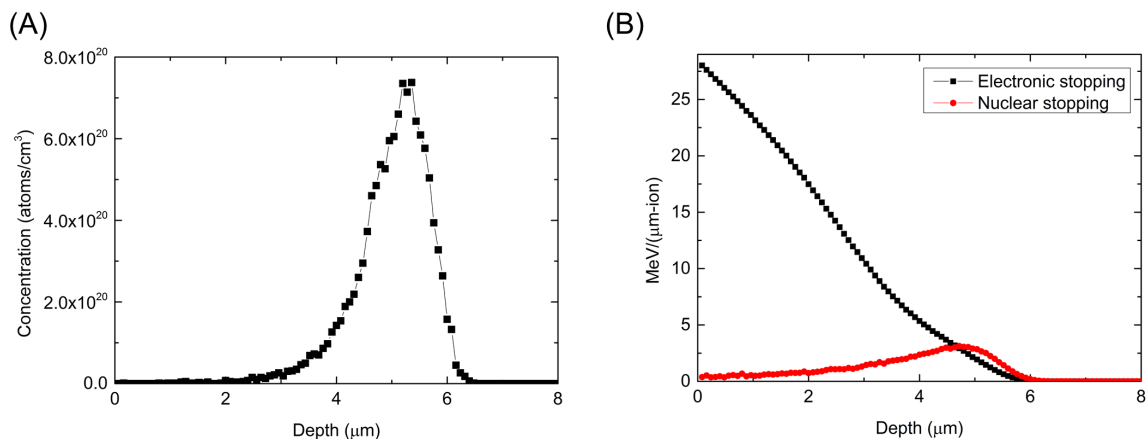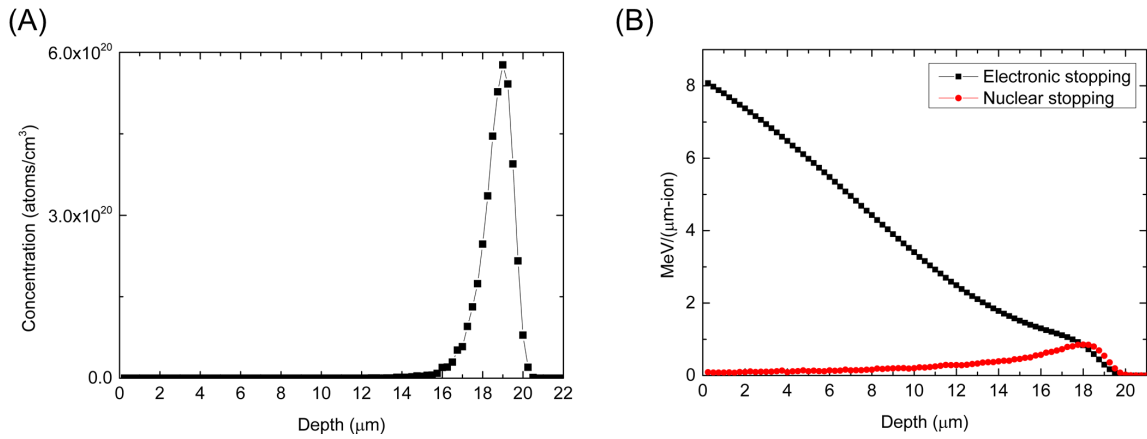

Figure 3.16: Calculated ^{127}I distribution (A) and ^{127}I energy loss (B) inside the UMo: SRIM calculations shows that ^{127}I ions at 80 MeV have an averaged penetration depth of 5.0 μm and the maximum nuclear stopping power reaches 4.9 μm.
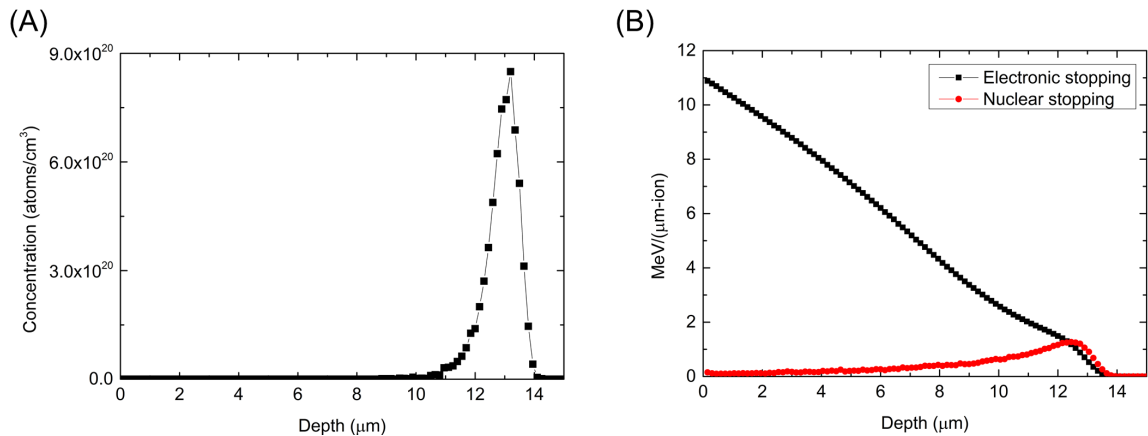
Figure 3.17: Calculated ^{127}I distribution (A) and ^{127}I energy loss (B) inside the Al: SRIM calculations shows that ^{127}I ions at 80 MeV have a penetration depth of 12.8 μm and the maximum nuclear stopping power reaches 12.5 μm.

Figure 3.18: Calculated ^{127}I distribution (A) and ^{127}I energy loss (B) inside the UMo: SRIM calculations shows that ^{127}I ions at 80 MeV have an averaged penetration depth of 18.5 μm and the maximum nuclear stopping power reaches 18.2 μm.

3.4.2 A dynamic binary collision computer simulation code (TRI-DYN)

TRIDYN [87] simulates dynamic changes of thickness and composition of multicomponent targets during high-dose ion irradiation. It is based on TRIM, using the binary collision approximation (BCA) model for ballistic transport (Sec. 2.3.2). Crystal structures of the target and the grown layers are not taken into consideration so they are assumed to be amorphous. Each simulated projectile represents a physical increment of incident fluence (incident particles per unit area). TRIDYN allows to calculate the depth profiles of different atomic species in the target as function of the incident fluence. Originally, TRIDYN is less suitable for energies in the MeV range or above since it does not contain a collision frequency reduction such as in TRIM for higher energies. However, the TRIDYN applied in this study has been modified by including cross-sections at higher energy, i.e. above MeV. The surface energies of U and Mo apply the sublimation energies to calculate the surface erosion and the corresponding values are 5.5 and 6.8 eV, respectively. For those material deep below the surface, surface erosion can be neglected. TRIDYN calculations give a information about the contribution of ballistic effects to the total atomic mixing at interfaces and further enable the clarification of mechanisms of ion beam mixing.

Chapter 4

Swift Heavy Ion Irradiation Simulating In-Pile Irradiation

4.1 Introduction

One major goal of the UMo/Al fuel development is to limit or even suppress the IDL growth under in-pile irradiation. To optimize fuel plate composition, numerous in-pile tests are necessary. Since in-pile irradiation experiments are extremely time-consuming and expensive, alternatives, which are fast and economic, to reproduce in-pile tests are urgently needed. These alternatives are so-called out-of-pile methods. They have been developed in order to accurately simulate radiation damages inside UMo/Al fuel causing by energy losses of fission products.

Thermal annealing is one of the out-of-pile methods and it has been widely applied. However, this method leads to significantly different results compared with in-pile experiments. Particularly, thermal annealing often results in the destabilization of γ-UMo[1] and crystalline phases of IDL[2], e.g. UAl_x and UMo_yAl_z [88, 89]. These two features are not found in in-pile irradiated UMo/Al at temperatures below 200°C [21]. Another out-of-pile method is swift heavy ion irradiation which has been demonstrated its ability to reproduce IDL in the UMo/Al fuel plate [30, 90, 91]. The heavy-ion-irradiated UMo/Al fuel plate exhibits no γ-UMo destabilization and the elementary composition of IDL is the same as that in in-pile irradiated fuel plates. However, instead of being amorphous as under in-pile irradiation, IDL induced by swift ion irradiation has been found mainly consisting of crystalline phases (i.e. UAl_3) [91]. Therefore, improvements of the irradiation conditions have been studied in order to reproduce an amorphous IDL as under in-pile irradiation.

In addition, the geometry of UMo/Al samples used in swift heavy ion irradiation has been simplified into the monolithic system (denoted as UMo/Al bilayer) to enable a direct interpretation [32, 92]. In the past, dispersed samples[3] were exclusively used

---

[1]U usually crystallizes in orthorhombic structure, known asα-U, while UMo in cubic structure (γ-UMo) forms in a metastable state by Mo addition. Therefore, γ-UMo destabilization often refers to the phenomenon that γ-UMo becomes α-U and U_2Mo.

[2]Most of IDLs found in in-pile tests are in amorphous structure.

[3]UMo powders dispersed in an Al matrix.

in swift heavy ion irradiation [30, 90, 91]. Three types of the UMo/Al interface with respect to the irradiation direction can occur in the dispersed samples: UMo/Al and Al/UMo interfaces situated perpendicular to the irradiation direction or parallel to the irradiation direction. These geometries are illustrated in Figure 4.1, a SEM picture taken on a cross-section of a swift-heavy-ion-irradiated fuel plate. However, among these types of interface only the red UMo/Al interface perpendicular to the irradiation direction is relevant to in-pile irradiation that fission products are created in UMo grains and then ejected towards the Al matrix [93]. Therefore, applying the monolithic system for studying the UMo-Al interdiffusion can enable a direct interpretation.

This chapter presents two UMo/Al bilayers irradiated by ^{127}I at 80 MeV and afterwards characterized by RBS and STEM which have a deep sub-micrometer spatial resolution. The interest to accurately characterize the irradiated areas will be presented. In addition, nano-XRD also has been performed in the irradiated UMo/Al bilayer (T = 140°C) Finally, IDL formation under swift heavy ion irradiation as well as comparisons of the characteristics of IDL obtained under swift heavy ion irradiation and under in-pile irradiation will be discussed. The U-Mo-Al interaction will discussed in detail as well, the influence of the irradiation temperature and an estimation of irradiation-induced diffusion coefficient.

4.2 Sampling

The UMo/Al bilayers involved in this investigation are composed of a UMo layer (4.9 μm and 2 μm) upon an Al substrate, preparing by DC-magnetron sputtering. Afterwards, the UMo/Al bilayer were irradiated by ^{127}I ions at 80 MeV, reaching a final fluence of 10^{17} $ions/cm^2$ at a temperature of 140 ± 2°C and 200 ± 2°C, respectively. For SEM characterization, a cross-section of the UMo/Al bilayer has been prepared. For STEM and nano-XRD measurements, the thin-film preparation of the UMo/Al bilayers were carried out by FIB milling to the final thickness of 100 nm.

4.3 TRIM calculations: ion-solid interactions

In order to simulate damages created by ^{235}U fission during in-pile irradiation, ^{127}I ions at 80 MeV have been applied in swift heavy ion irradiation. In the case of perpendicular incidence, TRIM calculations (Monte Carlo calculations of the stopping range of ions in matter [86]) predict a mean penetration depth of ^{127}I and the depth profile of stopping powers, i.e. electronic stopping power and nuclear stopping power. For the UMo/Al bilayer irradiated at 140°C, the mean penetration depth is 5.4 μm (Figure 4.2A). The calculated nuclear stopping reaches a maximum at a penetration depth of 4.9 μm, right at the UMo/Al interface and most of the incident energy is lost via electronic collisions (Figure 4.2B). As for the UMo/Al bilayer irradiated at 200°C, TRIM calculations predict a mean penetration depth of ^{127}I of 9.1 μm in the UMo/Al bilayer as shown in Figure 4.3A and nuclear stopping reaches a maximum at a penetration depth of 7.4 μm and at the interface nuclear stopping power is around 1.2 MeV/(μm-ion) (see Figure 4.3B).
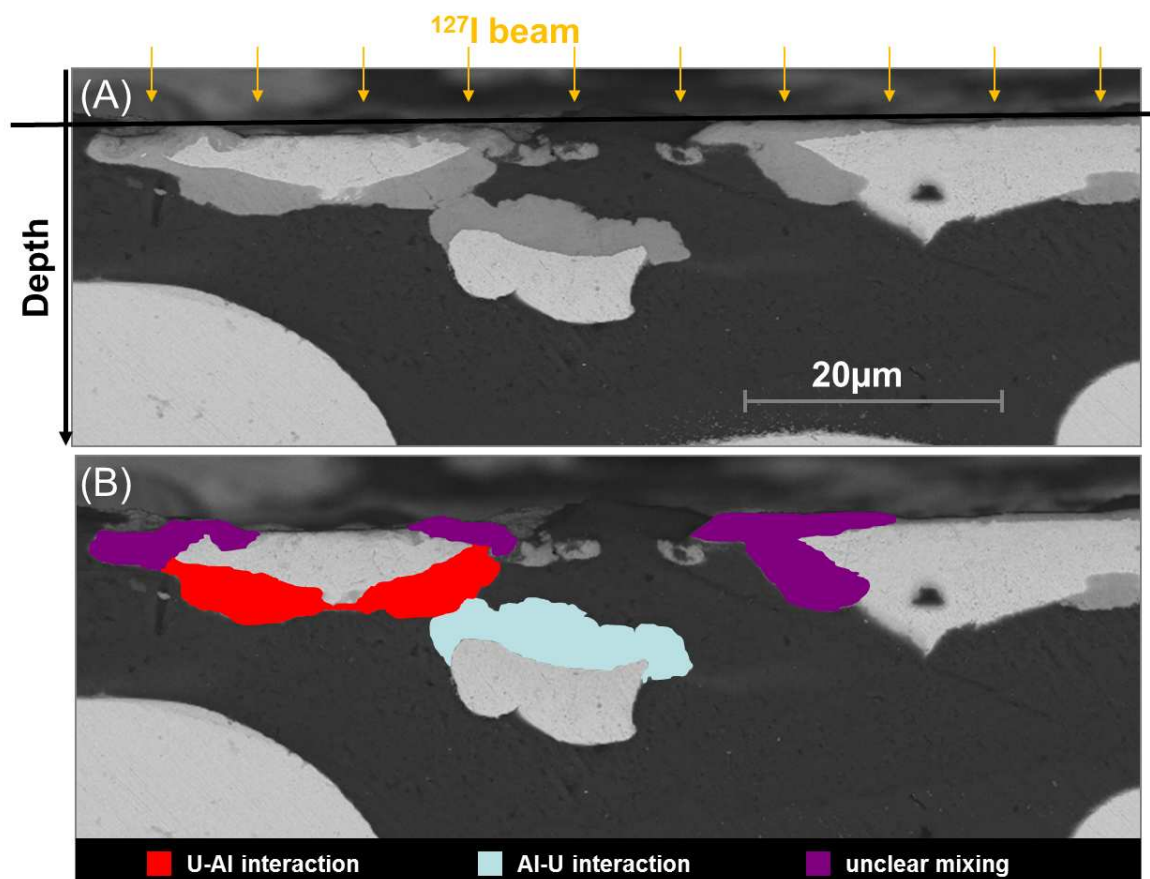
Figure 4.1: Three types of IDL obtained in a UMo/Al dispersed fuel plate by 80 MeV ^{127}I ions irradiation. (A) SEM characterization of a fuel plate transversal cross-section in backscattered electron mode (BSE): UMo particles appear in white, IDL in gray, and Al in black; (B) image shown in (A) after colorization of the IDL with red, cyan, and purple. These three colors highlight three IDL types: IDL at UMo/Al interfaces (^{127}I ions collide with UMo first), IDL at Al/UMo interfaces (^{127}I ions first hit Al), and IDLs coming from an unclear ion mixing (either located at the sample surface or at the matrix/UMo particles interfaces oriented parallel to the irradiation direction).

4.4   Ion irradiation induced IDL: overview

The non-irradiated and the irradiated areas of the UMo/Al bilayer irradiated at 140°C have been characterized in SEM using backscattered electron mode (BSE). The associated images are shown in Figure 4.4. It indicates that no IDL is present in the non-irradiated area whereas an IDL has grown at the UMo/Al interface irradiated with swift heavy ions. This clearly evidences that the IDL growth at the UMo/Al interface is only driven by swift heavy ion irradiation. In other words, the presence of the IDL can neither be attributed to the sputtering manufacturing process, nor to a pure temperature effect (T=140°C during swift heavy ion irradiation).
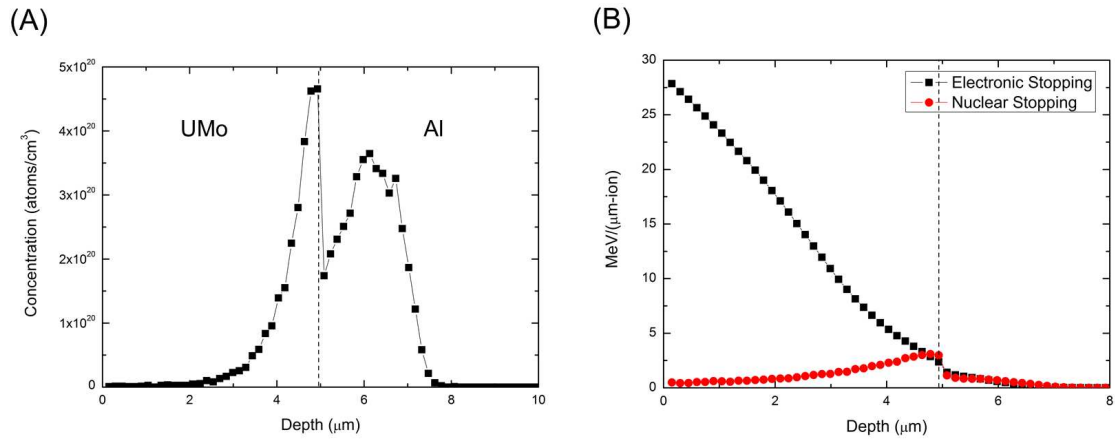
Figure 4.2: Calculated ^{127}I distribution (A) and ^{127}I energy loss (B) inside the UMo/Al bilayer. TRIM calculations shows that ^{127}I ions at 80 MeV have a penetration depth of 5.4 μm and the maximum nuclear stopping power reaches at the interface. The geometry of the bilayer is marked with the dashed line.
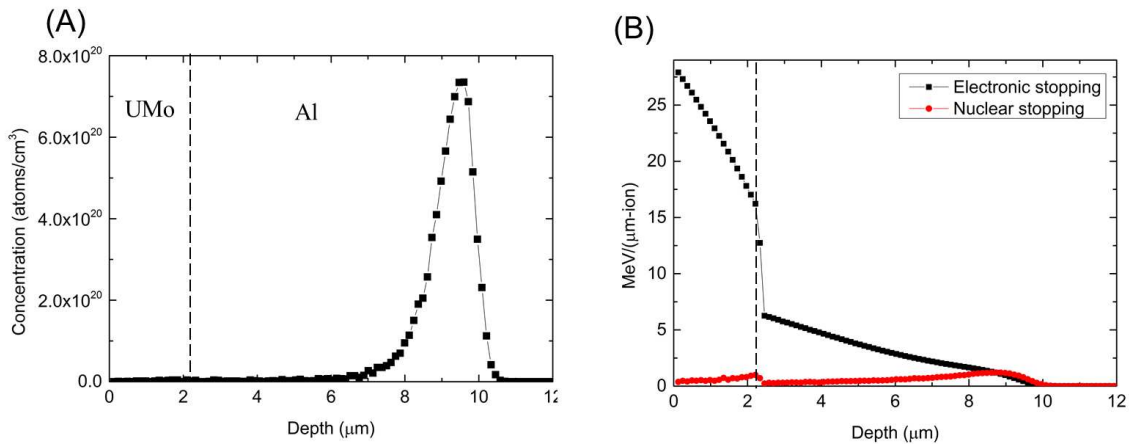

Figure 4.3: TRIM calculations: ^{127}I distribution (A) and the stopping power distribution (B) inside the UMo/Al bilayer

4.5 Microstructural modifications

Microstructural evolution induced by swift heavy ion irradiation were characterized by STEM for both UMo/Al bilayers. For the UMo/Al bilayer irradiated at 140°C, nano-XRD has also been applied.

An overview of the irradiated UMo/Al bilayer (T=140°C) has been recorded by a STEM–HAADF detector (Figure 4.13A). The lateral structure consists of the Al substrate, the IDL ($\sim$ 1 μm), and the UMo layer. In addition, a porous layer with a thickness of 80 nm has been found at the Al/IDL interface. This layer results from the sample preparation by DC-magnetron sputtering[4].

---

[4]The porous layer has been found at both the non-irradiated and the irradiated areas of FIB-milling-prepared cross-sections.
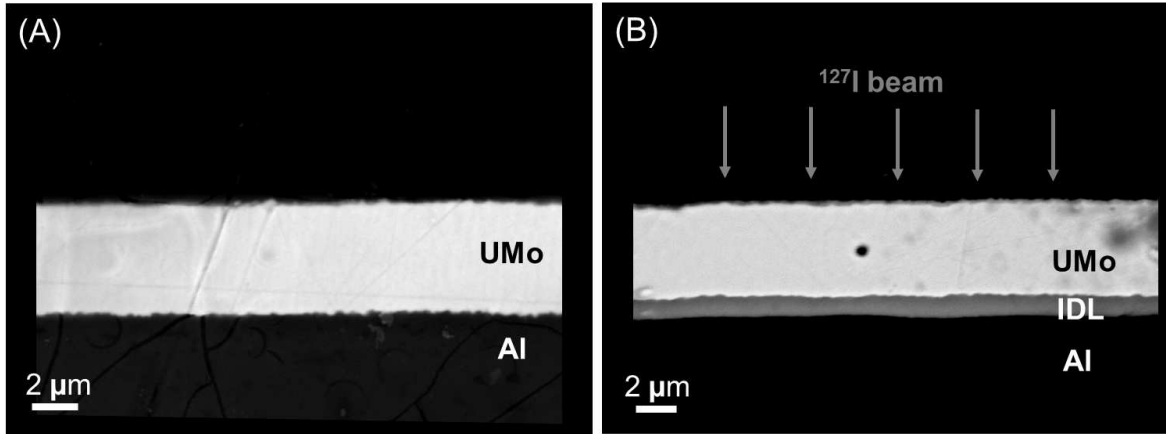
Figure 4.4: A comparison between the non-irradiated (A) and the swift-heavy-ion-irradiated UMo/Al interfaces (B) in the same UMo/Al bilayer has been made by SEM in backscattered electron detection mode (BSE).

The bright field images and the selected area diffraction patterns (SADP) of the irradiated area are shown in Figure 4.5, where the applied aperture size of electron diffraction is 200 nm. In Figure 4.5A, the diffraction pattern measured in the Al substrate reveals polycrystalline Al with sub-micrometer grain size. Note that before swift heavy ion irradiation the grain size of the UMo/Al bilayer was 400 μm in diameter measured by confocal microscopy as shown in Figure 4.6. Based on the electron diffraction pattern of Al, it has been derived that the Al substrate experienced grain sub-division, so-called recrystallization, under swift heavy ion irradiation.

Recrystallization is a process that deformed grains are replaced by the new strain-free grains and usually occurs during or after deformation by cold work, irradiation, etc., where the lattice of material has been strained. The cold work in the UMo/Al mainly came from ion irradiation but also a great amount of strain energy has been introduced during DC-magnetron sputtering[5] (Figure 3.2B). The recrystallized grain size can be estimated using the Scherrer equation [94, 95]

$$\Delta(2\theta) = \frac{G\lambda}{Lcos\left(\theta_g\right)} \tag{4.1}$$

where G is the shape factor (G = 0.89 for spheres, G = 0.94 for cubes [96]), L is the nanoparticle size, θ_g is the Bragg angle and $\Delta\left(2\theta\right)$ is the broadening of the diffraction ring at FWHM (in radian). The Scherrer equation is applicable for defect and strain free nanoparticles smaller than 100 nm. To apply the Scherrer equation software Digital micrograph (DM) [97], DM package DiffTools [98], and software Fityk 0.9.8 [99] have been utilized. After a calibration in DM, using DiffTools by Locate SADP function to obtain 1D pattern (intensity/2θ) out of the electron diffraction pattern. Afterwards, the 1D pattern can be fitted by Fityk 0.9.8 and then one can receive the values of $\Delta\left(2\theta\right)$ and θ_g. The calculated grain size of Al via Scherrer equation is about 10 nm in diameter.

---

[5]In a heat treatment experiment of UMo/Al bilayer, strains produced by DC-magnetron sputtering were released and then the the UMo/Al bilayer was completely deformed.

At the IDL, an amorphous phase has been observed by the diffraction pattern (Figure 4.5B), with a nearest neighbor distance of 0.250 (20) nm. This value coincides with the results from in-pile tests well. A comparison between IDLs produced by swift heavy ion irradiation and in-pile irradiation will be discussed in detail in Sec. 4.7.1. According to Sec. 2.4.1, the amorphization can take place when the ionicity difference is minor as described by N-K ionicity rule [56]:

$$ionicity = 1\!-\!exp\left[-0.25\left(X_A - X_B\right)^2\right] \leq 0.1$$

where X_A and X_B are the electronegativities of atoms A and B, respectively, in the A-B binary system. Considering the main composition of IDL, A and B denote as U and Al, respectively. The electronegativity of U is 1.38 and of Al is 1.61. The ionicity of the U-Al binary system is $0.013 \leq 0.1$ which meets the rule of Naguib and Kelly derived empirically based on the bond type. On the other hand, when considering A and B as Mo and Al, respectively. The electronegativity of Mo is 2.16. The ionicity of the Mo-Al binary system is $0.07 \leq 0.1$ which also meets the N-K ionicity rule.

Figure 4.5C shows a representative of SADP in the UMo region. In this region, nanocrystalline UO_2 (Fm-3m) and micrometer-size UMo grains (Im-3m) have been observed. Using the Scherrer equation, the grain size of UO_2 is estimated to be about 6 nm. The nanocrystalline UO_2 might come from the oxidation of UMo[6]. Note that the diffraction pattern has been measured near UMo <100> zone axis. As shown in Figure 4.7, the pattern measured on UMo does not strictly correspond to the one simulated on the basis of cubic γ-UMo structure. The d_{hkl} values have been determined to 0.244 nm for direction A and 0.128 nm for direction B. For A direction the value of 0.244 nm is very close to the calculated one for UMo {110}, i.e. 0.242 nm which is obtained using 0.342 nm as the γ-U8wt%Mo lattice parameter [101]. For B direction, the measured value is definitely lower than expected if we assume a $(0\bar{2}2)$ reflection: calculated distance would be 0.121 nm. Besides, the angle between the different lattice directions (i.e. A and B) does not exhibit 90° as for BCC structures, but around 80°. It can be deduced that under swift heavy ion irradiation with a high fluence, UMo alloy in the BCC structure has been transformed into body-centered tetragonal (BCT) structure[7].

Nano-XRD patterns have been acquired in the UMo and in the IDL regions of the same irradiated UMo/Al bilayer (T=140°C); they are both shown in Figure 4.8. However, no diffraction pattern for the Al region is presented here since diffraction patterns of this region provided minor Al peaks to disable a meaningful analysis. This is attributed to due to the limited atomic scattering factor f (see Sec. 3.3.5), the overall thickness of the thin foil (just 2 μm), and the relatively high energy of the X-ray beam (29.6 keV). XRD analysis is processed with Rietveld refinement [82, 103]. In the obtained XRD patterns in the UMo region shown in Figure 4.8A, two phases have been identified: γ-UMo[8] (with 0.342 nm as the lattice parameter) and Cu (from the Cu grid). One

---

[6]Several studies reported that swift heavy ion irradiation will induce recrystallization in materials such as cold-drawn steels [100].

[7]Studies reveal that (swift) heavy ion irradiation tend to transform the lattice structure of the irradiated materials at relatively high does such as BCC/FCC [102].

[8]The structure of UMo has been set as BCC (i.e. γ-UMo) instead of BCT as indicating by STEM. Based on the small distortion of the BCC lattice and unknown structural parameters of BCT-UMo, the input of γ-UMo (BCC) is reasonable.

peak near 8.5° is not assigned. Note that similar results have been reported on γ-UMo atomized powders [89, 104] and UMo ingots [105]. In the diffraction pattern from the IDL (see Figure 4.8), the presence of an amorphous phase can be clearly seen. In this amorphous compound the nearest neighbor distance has been determined as 0.247(20) nm. Besides, UO_2 and Cu have been detected as well. Rietveld refinement gives lattice parameter of UO_2 as 0.545 nm which is a relatively low value. This suggests an over-oxidation of this phase (towards U_4O_9 or U_3O_7) [106]. Preferred orientation corrections have been used to improve the refinement quality of the Bragg lines associated with γ-UMo and Cu phases in both patterns of Figure 6. This correction is required because of the low sampling statistics with respect to powder diffraction of the nano-XRD measurements for these phases.

STEM and nano-XRD examinations reveal a strong oxidation which come from the exposure of the analyzed thin foil in the ambient atmosphere. Characterizations of STEM and nano-XRD show the amorphous state of the IDL with a first neighbor distance of 0.247 - 0.250 nm indicating a broad dispersion of first neighbor distance in this compound.

Figure 4.9 consists of an overview of the irradiated UMo/Al thin foil (T=200°C) and the corresponding SADPs. The inhomogeneous shape of the foil results from the pref-erential thinning of materials during FIB milling. The SADP at the UMo region shows a single crystalline UMo and polycrystalline UO_2. This observation implies that some UMo grains are bigger than the aperture size of SADP (i.e. 200 nm in diameter) and the other UMo grains might experience grain sub-division during swift heavy ion ir-radiation which have been consequently oxidized into nanocrystalline UO_2. The size of the nanocrystalline UO_2 is about 10 nm based on Eq. 4.1. These two diffraction patterns (or grain sizes) might result from i) the early stage of recrystallization that only a part of UMo grains undergo grain sub-division and ii) the final stage of recrys-tallization that some grains have been re-grown to a size bigger than the aperture size of SADP. The overview exhibits that after irradiation an IDL appears at the UMo/Al interface with a thickness of 310 nm. The trapezoidal hollows located at the IDL/Al interface comes from the sample subtrate, i.e. observed in the non-irradiated area. The SADP at the IDL region shows a completely amorphization where the nearest neigh-bor distance is 0.229 - 0.255 nm. At the Al region, instead of Debye-Scherrer rings as observed in the UMo/Al bilayer irradiated at 140°C (Figure 4.5C) the SADP indicates single crystalline Al.

A series of high resolution bright field images have been taken to investigate this band as shown in Figure 4.10. Based on the mass-thickness contrast of the TEM bright field images, one can interpret that this band imhomogeneously consists of voids with a diameter of 5 nm. The formation of voids is usually as a result of the vacancy current that accompanies the unequal flow in a diffusion couple. When one species moves faster than the other one, there will be a net flux of vacancies into the faster species. The Kirkendall experiment [112] demonstrates that the rate at which the two types of atoms (e.g. U and Al) in a binary solution diffuse is not the same. Based on the observation, one can hypothesize that this porous band in the IDL offers the very-first accommodation sites for fission gases. During the fission, energetic fission fragments (e.g. 70 - 80 MeV) are produced and travel through UMo, where they originated, toward Al matrix. After a certain dose, the IDL forms at the UMo/Al interface as well
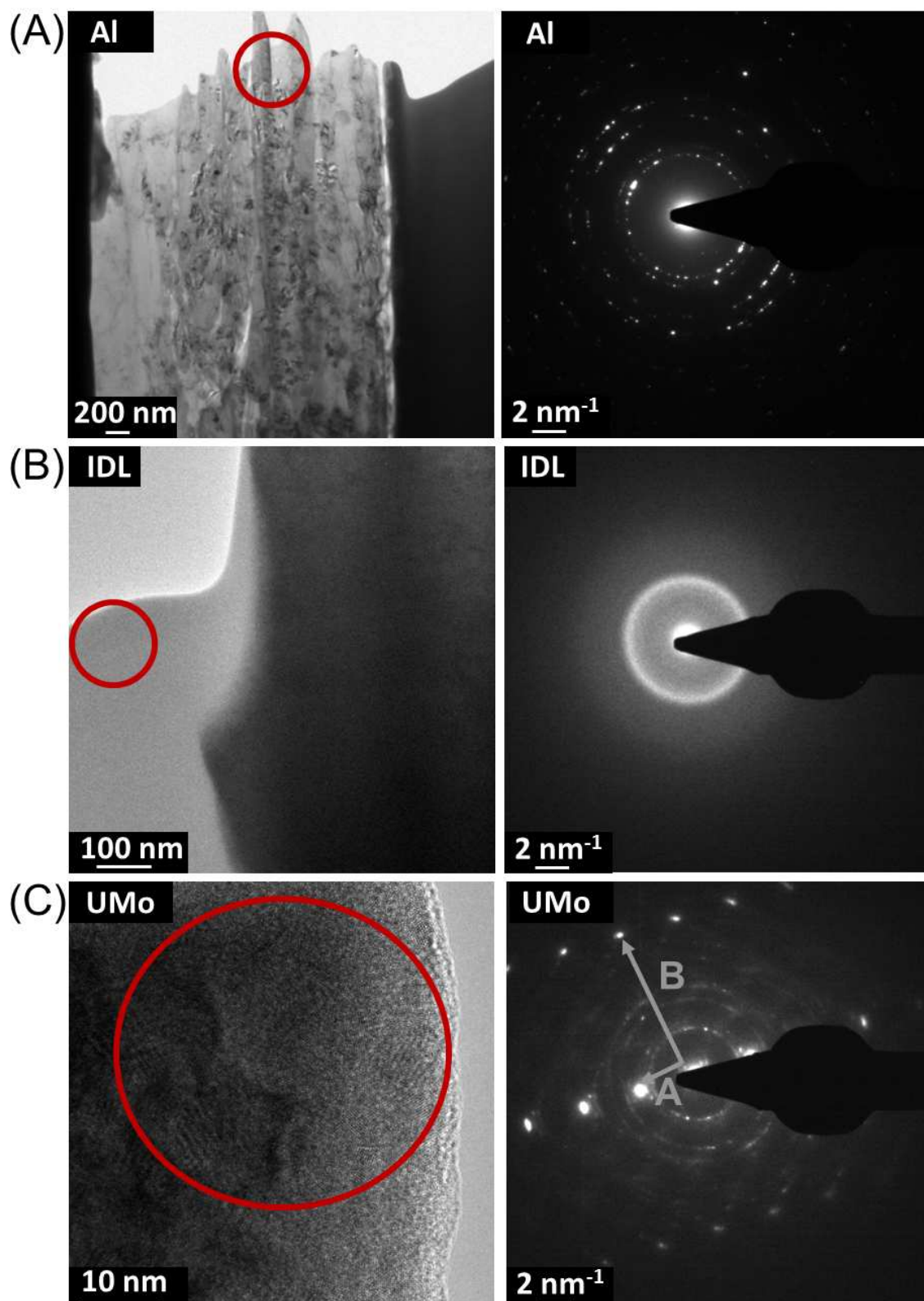
Figure 4.5: TEM bright field images and the associated SADPs for (A) Al, (B) IDL and (C) UMo which have been collected in the thin foil in zones a, b and c respectively. The marked areas in bright field images are the locations where SADP have been taken.
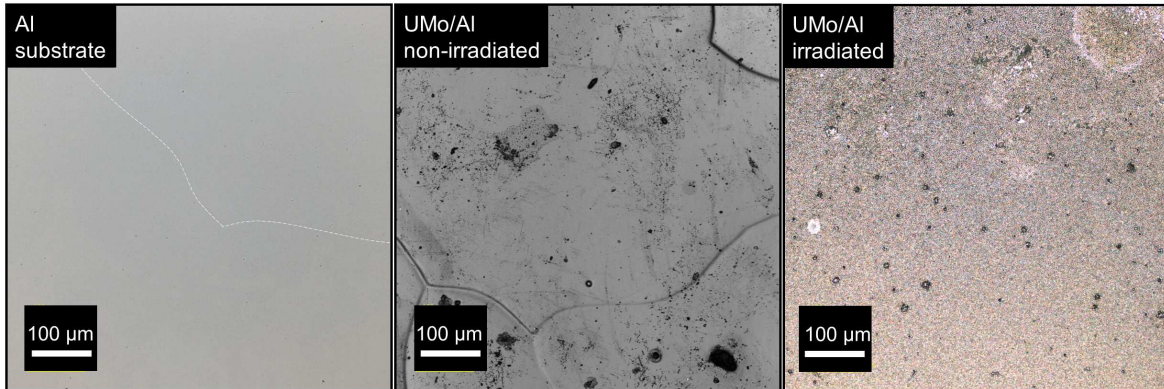
Figure 4.6: The surface morphology of a virgin Al substrate and the UMo/Al bilayer have been characterized by confocal microscopy. In the Al substrate, the grain boundaries have been marked with dashed lines and the grain size is around 400 μm in diameter. At the non-irradiated area of the UMo/Al bilayer, the grain size of the UMo layer is the same as that of Al substrate. However, at the irradiated area the surface morphology of the bilayer has been modified and no grain boundary is visible.
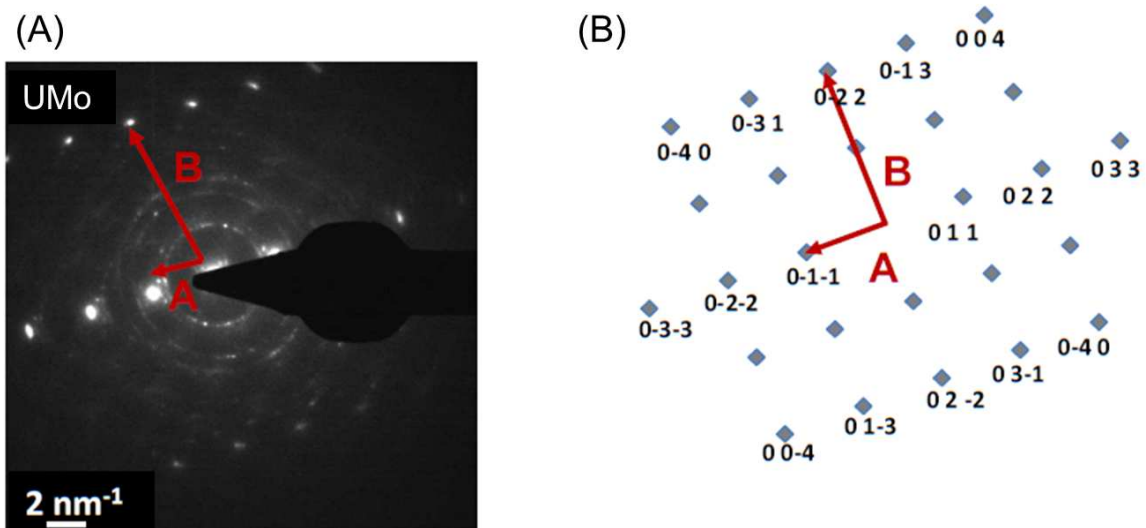
Figure 4.7: A comparison between the measured (A) and the calculated (B) electron diffraction patterns for UMo alloy has been made. Calculations have been performed assuming γ-UMo crystallographic structure and near $< 110 >$ zone axis, i.e. the angle between directions A and B is 90°. This angle equals to 80° in the measured image (A) and this indicates the γ-UMo structure (BCC) has been transformed into BCT structure under swift heavy ion irradiation.

as the porous band inside the IDL. When fission gases pass by the IDL they can easily fit in this porous band. Indeed, once the amount of fission gases increases reaching the maximum capacity of the pores, a pore expansion or migration toward to the IDL/Al interface could take place which lead to the results of in-pile irradiation: fission gases accumulating at the IDL/AL interface.

A comparison between the UMo/Al bilayer irradiated at 140°C and at 200°C has been made and tabulated in Table 4.1.

irradiation temperature (°C)		140	200
UMo thickness	(μm)	4.5	2
IDL	thickness (μm)	1.2	0.3
	crystal structure	amorphous	amorphous
	nearest neighbor distance (nm)	0.230 - 0.270	0.229 - 0.255
recrystallized	region	UMo and Al	UMo

Table 4.1: A comparison between characteristics of swift-heavy-ion-irradiated IDL at the irradiation temperature 140°C and 200°C has been made.

4.6 Chemical analysis

Chemical analysis utilizes RBS and EDX, which is equipped in STEM, . These two methods offer both macroscopic and microscopic aspects of chemical composition evolution after irradiation based on the characterized areas: several hundreds of μm for RBS and few nm for EDX.

After swift heavy ion irradiation, the UMo/Al bilayer irradiated at 140°C has been characterized by RBS at both the non-irradiated and the irradiated areas by protons with 2.5 MeV and alpha particles with 8 MeV. The corresponding spectra are shown in Figure 4.11. Spectra probed by protons (Figure 4.11A) exhibit modifications by swift heavy ion irradiation at the channel ~ 490 and at the channel $\sim 350 - 325$. At the channel ~ 490, RBS spectrum taken at the irradiated area appears less counts compared to that at the non-irradiated area. This difference comes from the strong surface oxidation at the beam spot during swift heavy ion irradiation. Around the channel of 325 - 250, the slope of the UMo decreases after irradiation and this implies a significant atomic mixing at the interface. These modifications in RBS spectra can also be observed in the alpha-particle-probed spectra (Figure 4.11B) where the slope decreases more obviously at the UMo/Al interface. A quantitative analysis of RBS can be processed by software SIMNRA [74] which gives elemental depth profiles. The elemental depth profiles corresponding to the proton-probed RBS spectra are shown in Figure 4.12A where the solid lines represent the non-irradiated area and the dashed lines denote the irradiated area. When comparing the elemental depth profiles of the non-irradiated and the irradiated areas, it shows a strong atomic mixing among U, Mo, and Al at the interface. Based on the elemental depth profiles, a $\frac{C_U}{C_{Al}}$ ratio (C denotes concentration) at the intermixed region is given as $\sim \frac{1}{2}$ both by protons (around the distance of 26250×10^{15} $atoms/cm^2$) and alpha particles (at the distance of 26400×10^{15} $atoms/cm^2$). The main composition at the UMo/Al interface (i.e. IDL) has been reported to be UAl_3 [91] so the ratio of $\frac{C_U}{C_{Al}}$ was expected to be $\frac{1}{3}$. This discrepancy might result from the limited resolution of RBS: the UMo layer has a high density (17.7 g/cm3) and this layer is relatively thick compared to most RBS studies, i.e. of the order of 100 nm.

On the other hand, an EDX linescan has been recorded across the interfaces from the Al substrate to the UMo layer at a step of 88 nm as shown in Figure 4.13A.

Qualitative contents in Al, U, and Mo at each point are plotted in Fig. 4.13B. This EDX measurement gives the ratio of $\frac{C_U}{C_{Al}}$ as $\frac{2}{3}$ and this deviated ratio might result from the K factor of EDX measurement (see Sec. 3.3.8) and too many stray X-rays from the Cu grid.

RBS spectra of the UMo/Al bilayer irradiated at 200°C at the non-irradiated and the irradiated areas have been probed by 2.5 MeV protons and 7 MeV alpha particles (see Figure 4.15). At the UMo/Al interface, the slope of the UMo decreases ($\sim$ channel number 415 - 435 in the proton-probed spectra; at channel number $\sim$ 630 - 650 in the alpha-particle-probed spectra). The simulated elemental depth profiles given by software SIMNRA [74] are shown in Figure 4.16. According to the elemental depth profiles, a $\frac{C_U}{C_{Al}}$ ratio (C denotes concentration) at the intermixed region is given as $\frac{2}{7}$ and $\frac{1}{4}$ by proton-probed (near the distance of $12000 \times 10^{15} \ atoms/cm^2$) and alpha-particle-probed (around the distance of $11500 \times 10^{15} \ atoms/cm^2$) RBS spectra, respectively. Based on the result of STEM, the intermixed region is majorly composed of IDL (i.e. UAl_3 [91]) yet the $\frac{C_U}{C_{Al}}$ ratios given by RBS measurements are not $\frac{1}{3}$ as expected.

A STEM-HAADF image and the corresponding EDX linescan have been taken after the UMo/Al foil was rotated 90° (Figure 4.14). The EDX linescan across interfaces shows that U migrated into Al side through the trapezoidal hollows. The composition ratio between U and Mo is around 1 : 2.6 over the IDL and the interdiffusion region is around 500 nm. In addition, a band with a thickness of 100 nm has been found at the IDL near the IDL/Al interface in HAADF image (Figure 4.14A).

4.7 Discussion

4.7.1 Comparison with in-pile irradiation

Several TEM investigations have been performed on in-pile irradiated U7wt%Mo powder dispersed in an Al-based matrix: van den Berghe examined UMo powder in a pure Al matrix [21], Gan and Keiser studied UMo powder in an Al matrix with 2 wt% of Si addition for minimizing the IDL formation (Al-Si matrix) [109, 110]. The irradiation temperatures ranges from 90°C to 130°C and the final fission density is in the regime of $10^{21} \ fissions/cm^3$) [109, 111]. An overview of these in-pile tests is given in Table 4.2. These studies report that the IDL are in form of an amorphous structure with a nearest neighbor distance from 0.239 nm to 0.251 nm. From Table 4.2 one can conclude that the distribution of first neighbor distance in the IDL is much broader in swift-heavy-ion irradiated samples than in in-pile irradiated ones. However, this difference could be also a result of different methods used for calculating uncertainties.

4.7.2 IDL formation

The IDL of the UMo/Al bilayer formed during swift heavy ion irradiation is mainly composed of the U-Al compounds, i.e. UAl_3 [91]. An in-situ annealing-XRD experiment of UMo powder dispersion in an Al matrix shows that the formation of UAl_3 begins slowly at 425°C [107]. As the system temperature rises to 450°C or 475°C, the

fission composition	final fission density ($10^{21} fissions/cm^3$)	irradiation temperature (°C)	IDL	characteristics
			structure	nearest neighbor distance (nm)
U7wt%Mo in Al matrix [21, 111]	1.41	<130	amorphous	0.239(4)
U7wt%Mo in Al matrix +2wt% Si [110]	3.32 (low flux)	90 (low flux)	amorphous	not measured
	6.3 (high flux)	120 (high flux)		
U7wt%Mo in Al matrix +2wt% Si [109]	4.5	109	amorphous	0.251
U8wt%Mo/Al under heavy ion irradiation (this work)	<0.4	140	amorphous	0.248(20)

Table 4.2: A comparison between characteristics of interdiffusion layers (IDL) obtained by in-pile irradiation and by swift heavy ion irradiation has been made. In each case irradiation conditions are indicated (e.g. final fission density, irradiation temperature).

growth rate of UAl_3 significantly increases as shown in Figure 4.17. However, the system temperature during swift heavy ion irradiation is only 140°C. Indeed, swift heavy ion irradiation is in non-equilibrium state while the thermal annealing is an equilibrium system. The discrepancy in temperatures implies that during irradiation, the local temperatures or the atomic mobilities are comparable to those at T > 425°C in an equilibrium system. An investigation of altering irradiation temperature has been made at the same irradiation conditions of the present work (^{127}I at 80 MeV with a final fluence of 10^{17} $ions/cm^2$)[92]. The result shows that the IDL formation (i.e. thickness) is proportional to the irradiation temperature when T ≥120°C while at T ≤ -35°C the growth of IDL is completely suppressed. This indicates that the IDL formation is highly related to the irradiation temperature and one can derive that the diffusion during swift heavy ion irradiation is thermal diffusion enhanced by irradiation. There are two mechanisms which have been widely exploited to describe diffusion behaviors under ion irradiation: radiation enhanced diffusion (Sec. 2.3.3) and thermal spikes effects (Sec. 2.3.4). Radiation enhanced diffusion describes the overall diffusion coefficient will be enhanced by the increasing defects during irradiation, e.g. vacancies, interstitials, divacancies. In thermal spikes effects, it is assumed that molten zones form along the cascades due to the heat dissipation of incoming ions. Both mechanisms can explain the UAl_3 formation at relatively low system temperatures, e.g. 140°C and 200°C, during swift heavy ion irradiation.

In addition, the UMo-Al interaction under heavy ion irradiation has been studied by Birtcher and Baldo using 3 MeV Kr ions at 150°C [108]. The result shows that the interdiffusion observed in the Al concentration profile is related to the ion dose, i.e. displacement per atom (dpa). When the ion dose is above 60 dpa, UAl_3 forms at the

UMo/Al interface as shown in Figure 4.18. They conclude that during irradiation at 150°C, Al diffusion into UMo is rapid and the amount of Al diffusion linearly depends on damages caused by heavy ion irradiation. Besides, the concentration profile of Al dose not change as a result of annealing at 150°C for several hours and therefore the irradiation temperature 150°C is considered in athermal region. Birtcher and Baldo's work implies that nuclear stopping power, i.e. knock-on collision, dominates the formation of IDL (UAl_3) while electronic stopping power has relatively small influences. However, the correlation between nuclear stopping power and the formation of IDL cannot be completely adapted to our case due to different irradiation conditions. In ^{127}I ions irradiation at 80 MeV, most of the incident energy is lost via electronic stopping power ($\sim 96\%$) which means a great amount of heat has been dissipated during irradiation. On the other hand, irradiation using 3 MeV Kr ions, the incident energy is almost equally lost by two stopping powers (i.e. electronic and nuclear stopping powers) and that in this case knock-on collisions are more prominent.

4.7.3 Diffusion coefficient calculation

An irradiation-induced diffusion coefficient can be calculated from the elemental depth profiles measured in RBS. The elemental depth profiles in Figure 4.16 are scaled in % versus areal density ($atoms/cm^2$). Assuming the atomic density in the UMo/Al bilayer is the same as that in the bulk, the elemental depth profiles scaled in % versus distance (cm) can be obtained by dividing the areal densities ($atoms/cm^2$) with the atomic densities ($atoms/cm^3$). In addition, instead of the U-Mo-Al ternary system, the UMo-Al binary system has been considered by assuming the system has a constant ratio of $\frac{C_{Mo}}{C_U}$ in the UMo layer during the diffusion process (i.e. swift heavy ion irradiation). Consequently, the elemental depth profiles are plotted in Figure 4.19. The depth profiles are composed of a set of binned data after processed in SIMNRA and the number data points for fitting has been therefore limited to 5 (UMo: the star sign and Al: the circle with a cross) at the UMo/Al interface.

The irradiation-induced diffusion coefficients of UMo and Al are then estimated using Fick's second law since the relation among diffusion coefficient D, concentration C, distance x and diffusing time t can be formulated in error function *erf (x)*:

$$C(x,t) = \frac{C_0}{2}\left[erf(\infty) - erf\left(\frac{x}{2\sqrt{Dt}}\right)\right] \equiv \frac{C_0}{2}erfc\left(\frac{x}{2\sqrt{Dt}}\right) \qquad (4.2)$$

where C_0 is the initial concentration and $erfc(x) = 1 - erf(x)$. For the case of UMo diffusing into Al (i.e. D_{UMo}), Eq. 4.2 can be expressed as

$$C_{UMo}(x,t) = \frac{1}{2}erfc\left(\frac{x}{2\sqrt{D_{UMo}t}}\right) = \frac{1}{2} - \frac{1}{2}erf\left(\frac{x}{2\sqrt{D_{UMo}t}}\right) \qquad (4.3)$$

As for Al diffusing into UMo (i.e. D_{Al}), the equation can be expressed as

$$C_{Al}(x,t) = 1 - C_{UMo}(x,t) = \frac{1}{2} - \frac{1}{2}erf\left(\frac{x}{2\sqrt{D_{Al}t}}\right) \qquad (4.4)$$

Another premise is that most of diffusion reactions take place during irradiation: applying the irradiation duration as the diffusing time t. Afterwards, diffusion coefficients can be estimated by fitting the elemental depth profiles and the results of fitting are shown in Figure 4.20. The estimated diffusion coefficients of D_{UMo} (UMo into Al) and D_{Al} (Al into UMo) are $3.6 \times 10^{-20} cm^2/s$ and $3.5 \times 10^{-16} cm^2/s$, respectively. Unfortunately, a comparison with the results cannot be made since the diffusion coefficient of the UMo-Al system at 200°C or at this temperature region ($\pm 50°C$) is not available. Nevertheless, the values estimated by Fick's second law seems to be lower than expected: the growth constant of the U7wt%Mo/Al at 550°C is $7.2 \times 10^{-9} cm^2/s$ (based on the assumption of parabolic growth rate) [113].

The *effective mixing parameter k* (Sec. 2.3.2) of the UMo-Al system at 150°C has been reported by Birtcher and Baldo [108]. By using the equation

$$C_{Al} = C_0 e^{-(x/k\phi)^2} \qquad (4.5)$$

where C denotes the concentration, k is effective mixing parameter which equals to $\frac{Dt}{\phi}$ and ϕ is the ion dose (i.e. dpa), the concentration profiles of Al obtained under different ion does can be fitted (Figure 4.18). The resulting k is a constant of 30 nm^2/dpa under different ion doses. In our case, by converting the total fluence $10^{17} ions/cm^2$ into the average dpa using SRIM cascade (Sec. 2.2.2), the ϕ will be 117. The k has been calculated as 12.2 nm^2/dpa which is different by a factor of 2 compared to Birtcher and Baldo's work. However, as mentioned in Sec. 4.7.2, the irradiation condition used in their work Kr ions at 3 MeV while we applied I ions at 80 MeV. In our case, the maximum electronic stopping power and nuclear stopping power are around 26 MeV/(μm-ion) and $\sim$ 1.2 MeV/(μm-ion), respectively. On the other hand, in the case of Kr ions at 3 MeV the maximum electronic stopping power and nuclear stopping power are around 2.4 MeV/(μm-ion) and 2.6 MeV/(μm-ion), respectively. Based on the conclusion drawn by Birtcher and Baldo, the difference in k (a factor of 2) might come from the difference in nuclear stopping power of two irradiation conditions. Their conclusion, nuclear collisions dominate the diffusion process, cannot be completely applied on our case due to the significant difference in electronic stopping powers. Nevertheless, the difference in k (only a factor of 2) also indicates the estimation of diffusion coefficient by Fick's second law in our case is reasonable.

One should note that Fick's second law considers that diffusion coefficients are independent of the concentration variation during diffusion process which cannot fully describe the irradiation-induced diffusion in the UMo/Al bilayer. To obtain an interdiffusion coefficient precisely, Boltzmann-Matano method should be utilized. However, to apply Boltzmann-Matano method [114] having more data points at the interface is necessary and this implies the RBS resolution should be as good as a scale of 30 nm. This resolution cannot be achieved with our samples which have the UMo thickness $\geq 1 \ \mu m$. Indeed, a UMo/Al bilayer with a much thinner UMo layer, e.g. 100 nm, can achieve a good resolution in RBS and then enables the application of Boltzmann-Matano method for the interdiffusion coefficient. However, a dilemma appears when irradiating a bilayer with such a thin layer with swift heavy ions: the incident energy will be entirely dissipated via electronic stopping power without any contribution from nuclear collisions as shown in Sec. 3.4.1. This is not desired for simulating in-iple irradiation where both electronic and nuclear stopping powers contribute to the IDL

growth. One solution to this dilemma is to apply heavy ion irradiation at different energies, e.g. high (70 - 90 MeV) and low energies (1-3 MeV). As mentioned in Sec. 2.2.1, energy loss by nuclear collisions or by electronic collisions depends on the velocity of incoming ions. Therefore, in order to obtain an interdiffusion coefficient induce by both collision effects (i.e. electronic collisions and nuclear collisions) a two-stage experiment, i.e. high and low energy ion irradiation will be ideal.

4.8   Summary

After swift heavy ion irradiation the formation of an IDL between the UMo and the Al has been observed in U8wt%Mo/Al bilayer. Former studies suggested that the IDL is at least partially crystalline after swift heavy ion irradiation while it is fully amorphous after in-pile irradiation. This chapter indicates that by maintaining proper irradiation temperature and a geometry of samples with a well-defined UMo/Al interface, a fully amorphous IDL can be obtained under swift heavy ion irradiation. This study enhances the comparability of swift heavy ion irradiation to in-pile irradiation with respect to the formation of the IDL. This also confirms that swift heavy ion irradiation is an appropriate method to quickly study the effects of in-pile-irradiation without the risk of exposure to high levels of radiation. Furthermore, based on the elemental depth profiles measured by RBS, an attempt of deriving the diffusion coefficient has been made using Fick's second law. To obtain the interdiffusion coefficient precisely, Boltzmann-Matano method should be applied.
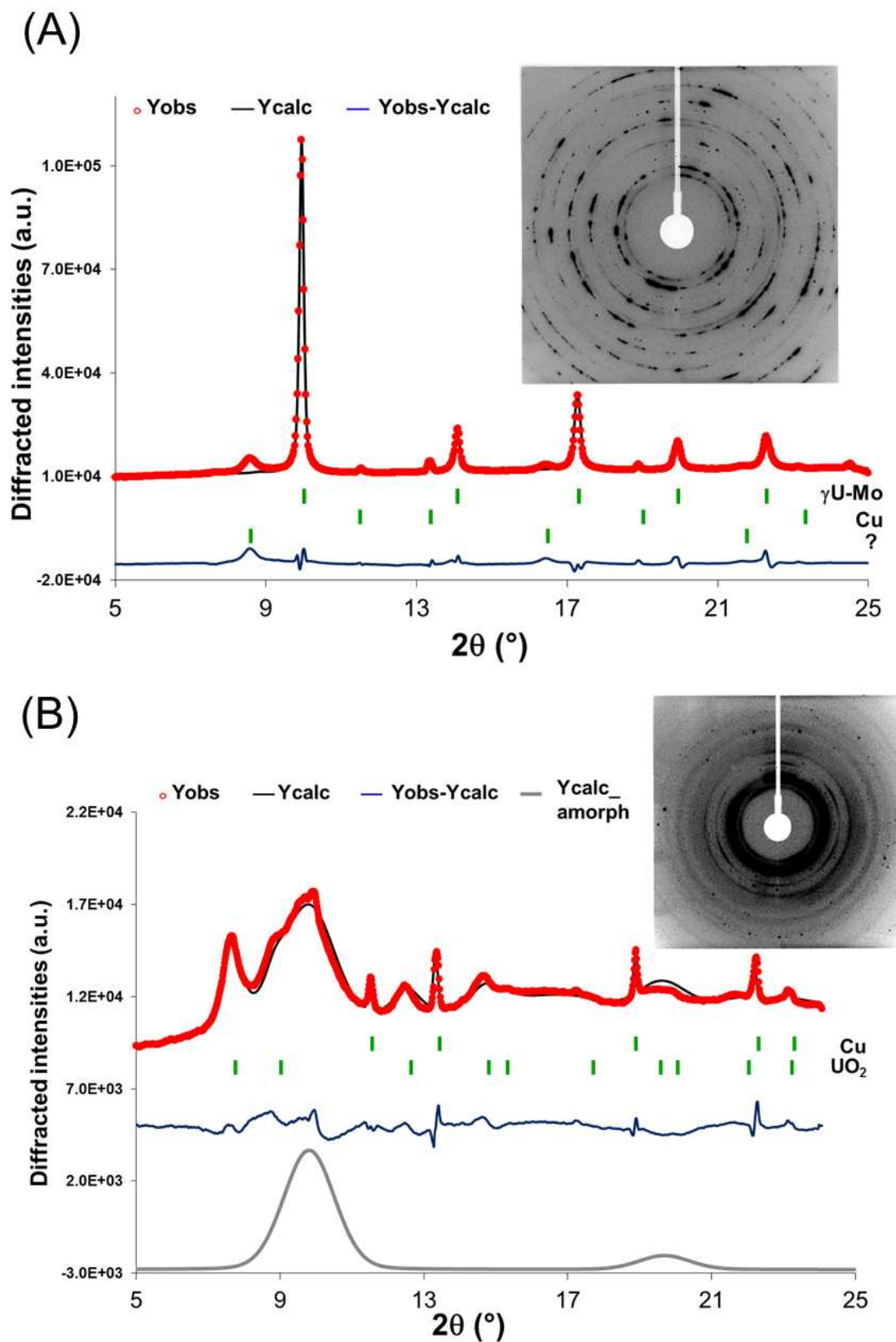
Figure 4.8: Nano-XRD analysis of the UMo (A) and IDL (B) areas in the thin foil (Fig. 4.13). For each case measured and calculated 1D patterns are compared and the measured 2D pattern is added as an inset. In (A) one peak near 8.5° is not assigned. Besides, the refined amorphous contribution is also plotted in the lower part of (B) as the gray line.
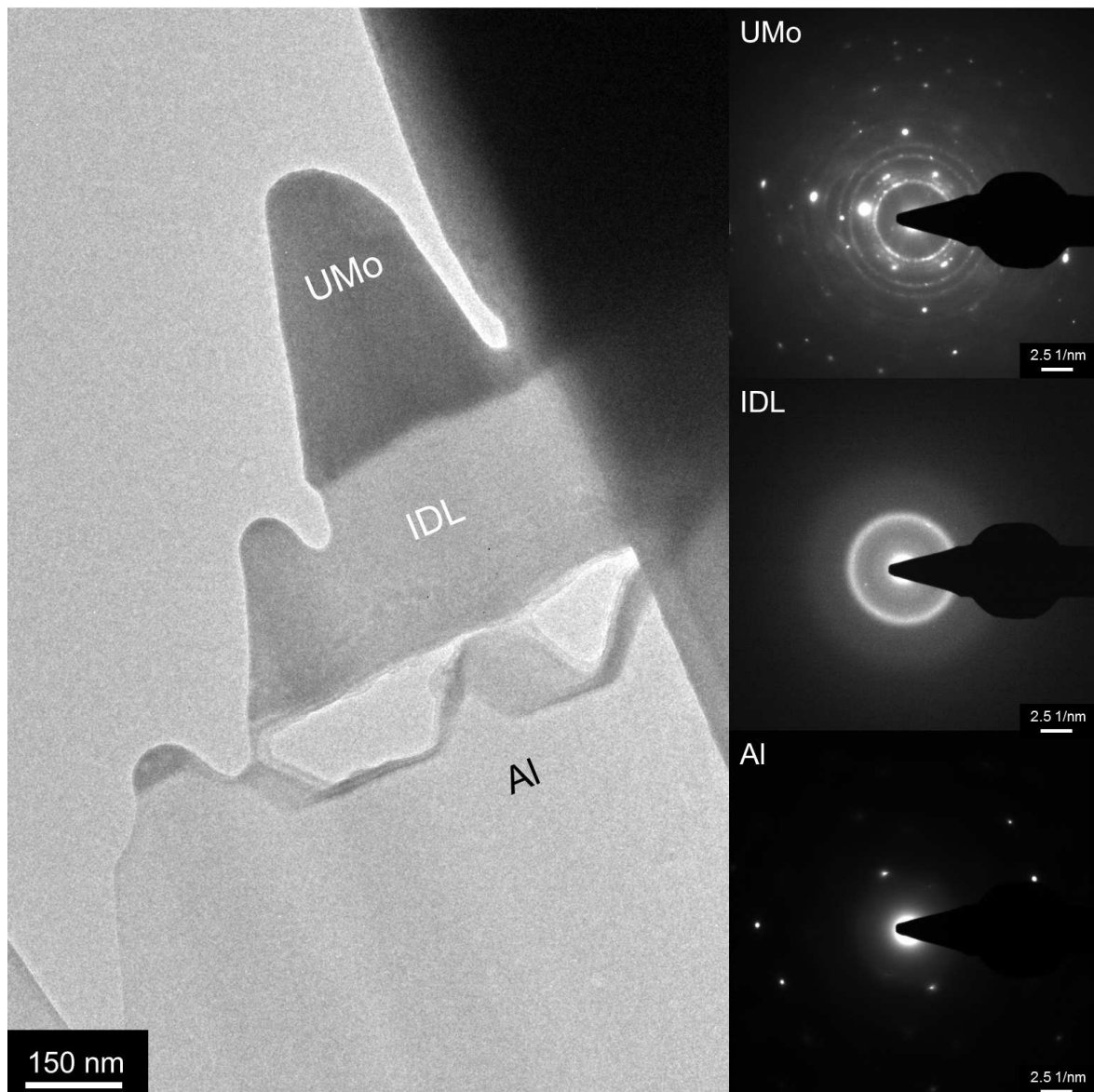
Figure 4.9: An overview of the UMo/Al foil irradiated at 200°C and the corresponding SADP at different locations
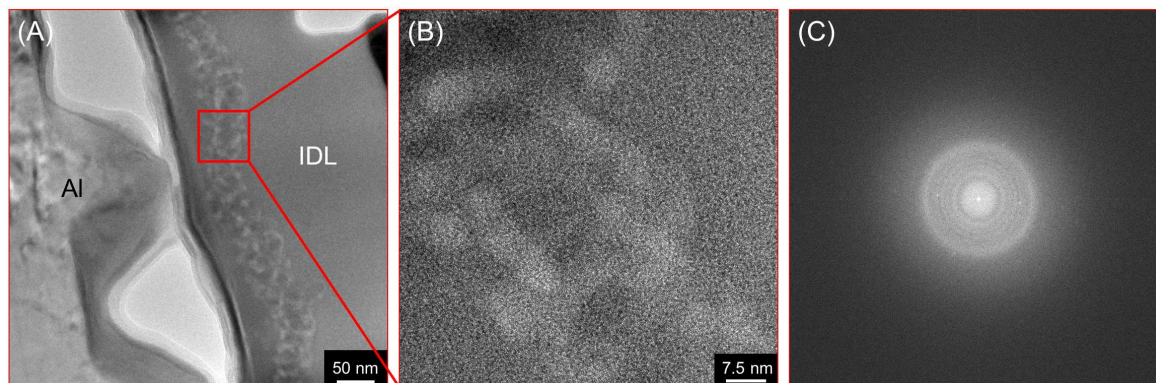
Figure 4.10: High resolution bright field images have been taken at (A) the IDL/Al interface and (B) the band located at the IDL. Based on the mass-thickness contrast of bright field images, it is deduced that the band shown in (B) is composed of voids. Its structure is amorphous indicated by (C) a fast Fourier transformation (FFT) out of (B).
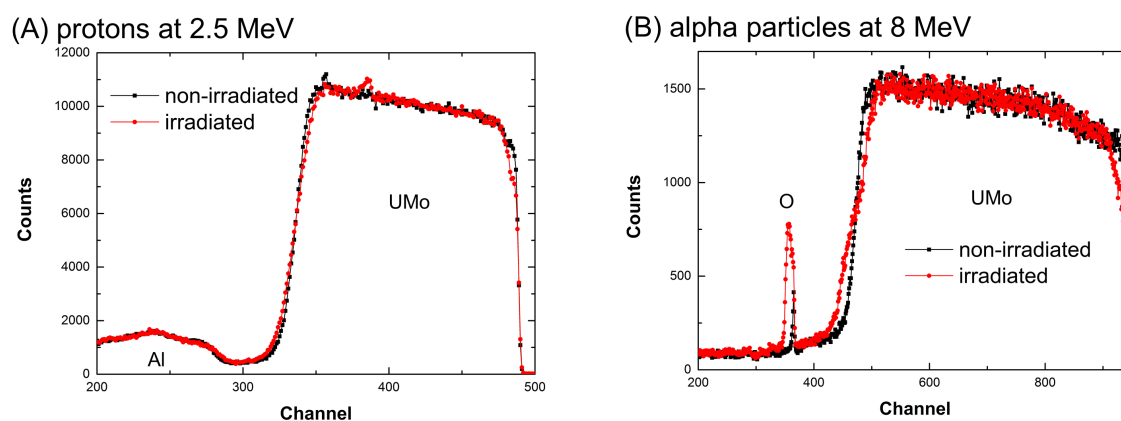
Figure 4.11: RBS spectra characterization by protons (A) and by alpha particles (B) have been performed at both the non-irradiated and irradiated areas of the UMo/Al bilayer where the irradiation temperature was 140°C.
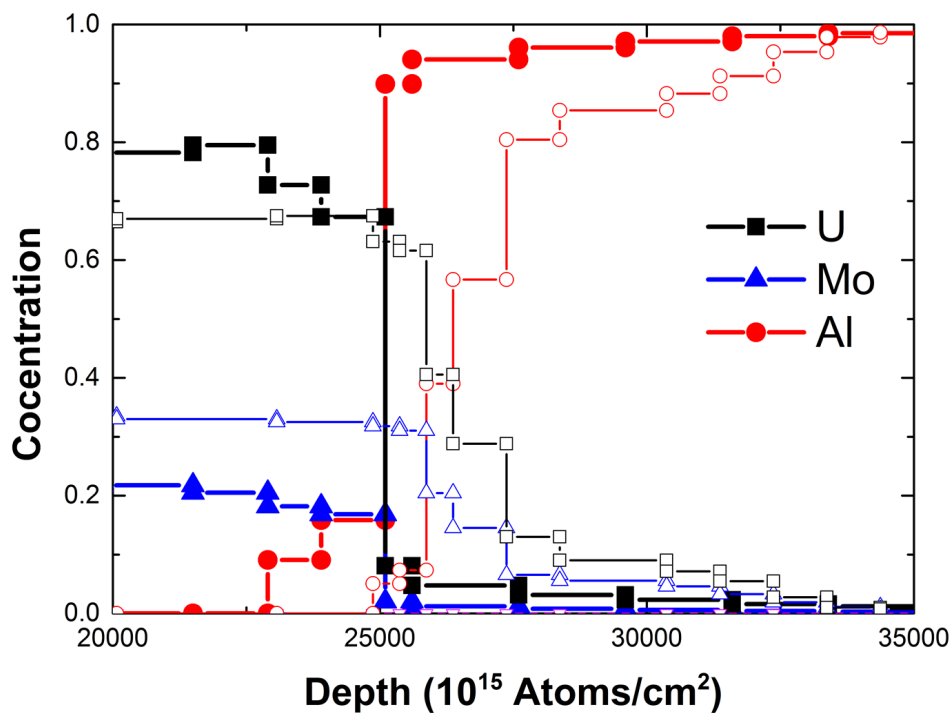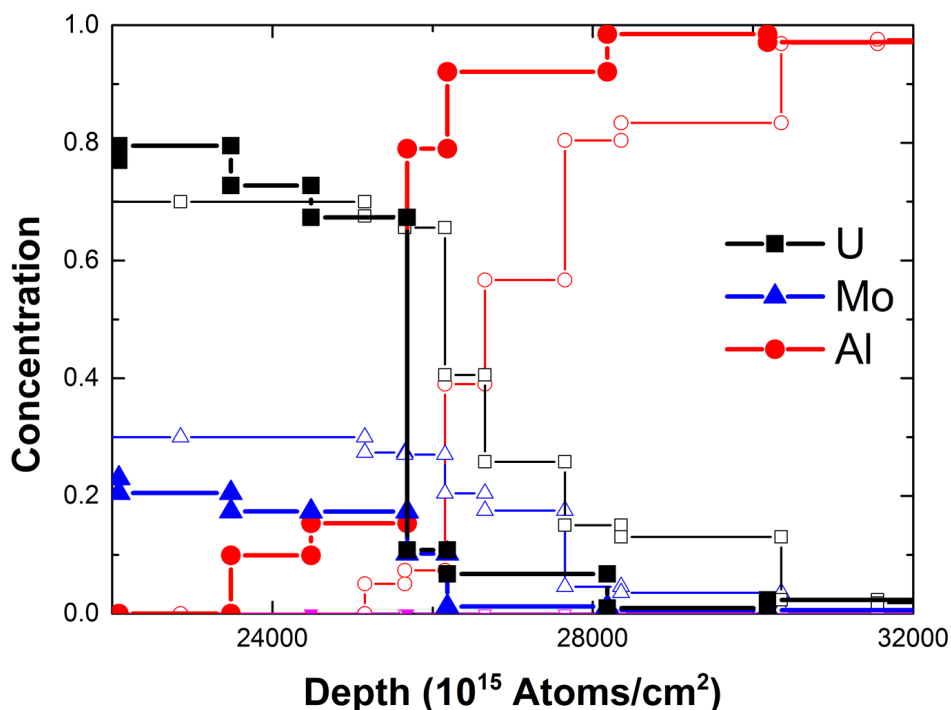
Figure 4.12: RBS spectra probed by protons and alpha particles give information of elemental depth profiles of the UMo/Al bilayer irradiated at 140°C as (A) and (B), respectively. The elemental depth profiles at the non-irradiated area are shown in solid symbols while those at the irradiated area are represented in hollow symbols.
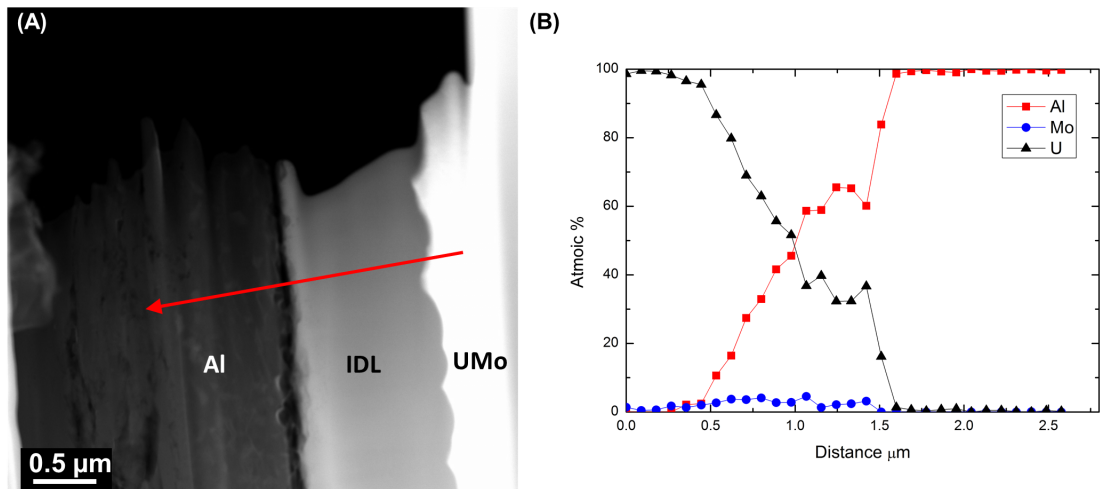
Figure 4.13: STEM-HAADF image of the UMo/Al bilayer (A) and the corresponding EDX quantification (B).
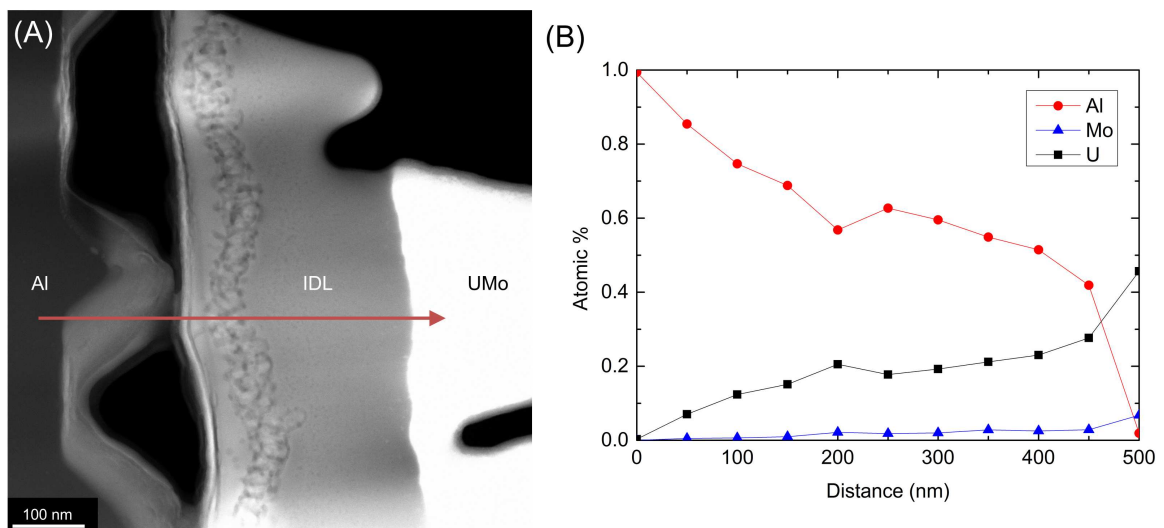
Figure 4.14: STEM-HAADF image of the UMo/Al bilayer (A) and the corresponding EDX quantification (B)
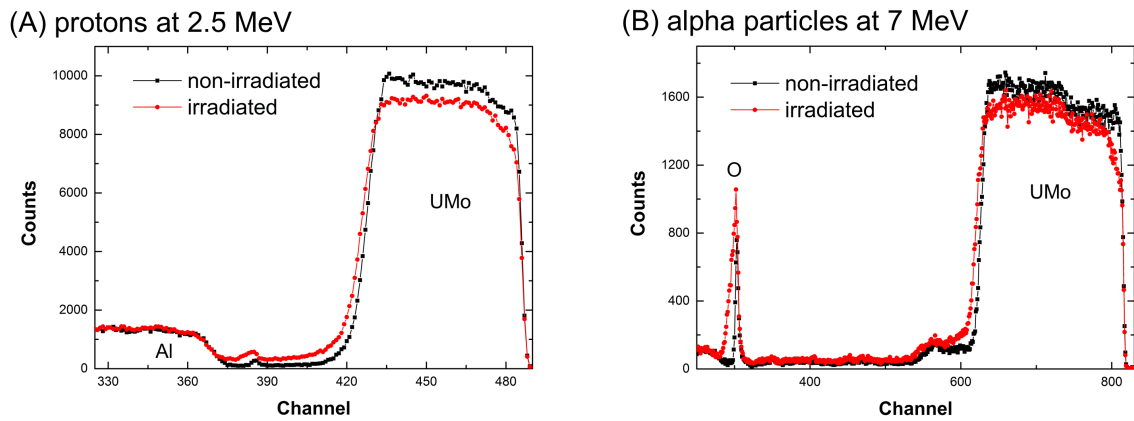
Figure 4.15: RBS spectra of the UMo/Al bilayer irradiated at 200°C characterization by protons (A) and by alpha particles (B) at the non-irradiated and irradiated areas
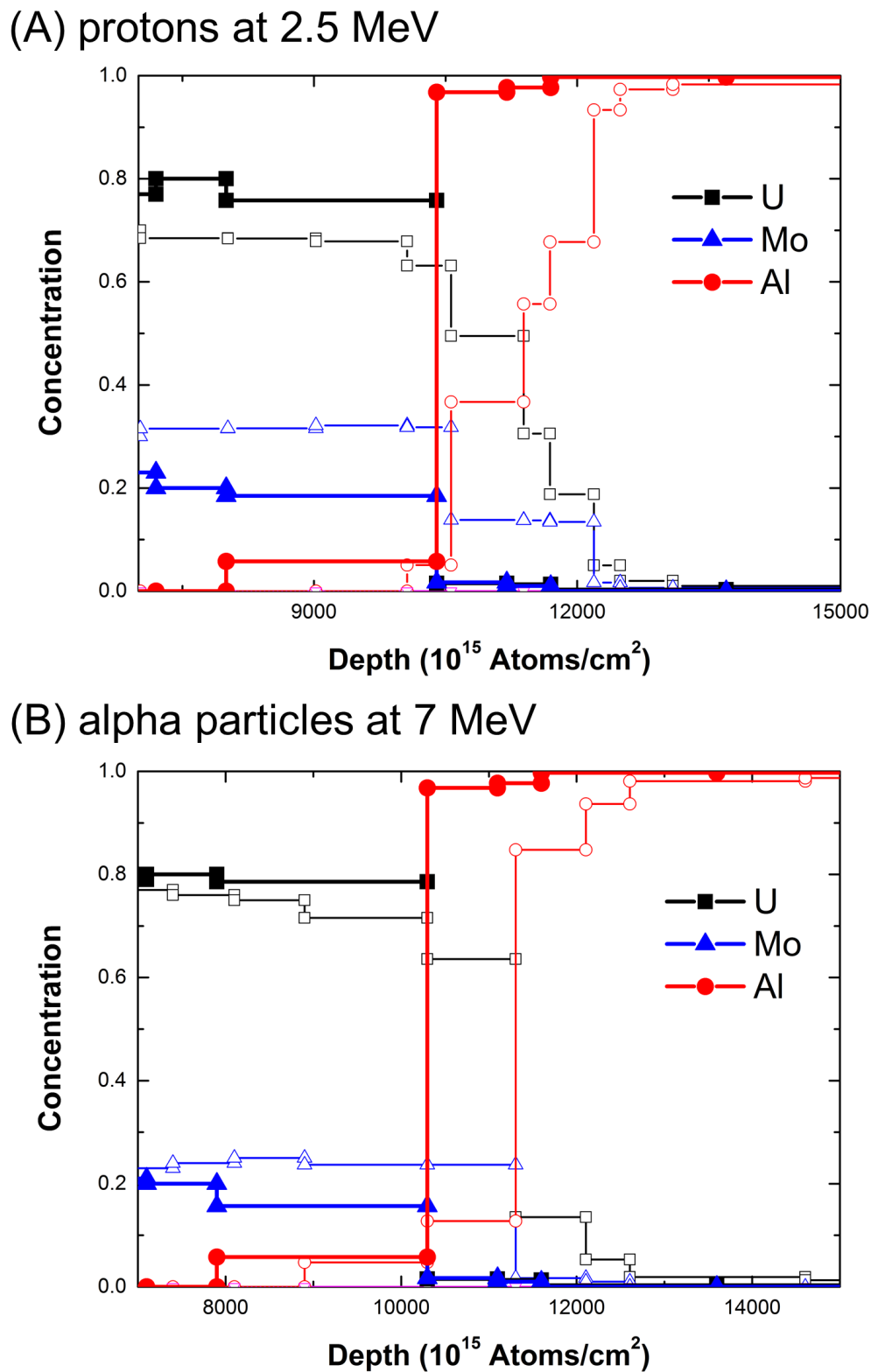
Figure 4.16: Elemental depth profiles of the UMo/Al bilayer (T=200°C) probed by (A) protons and (B) alpha particles: solid symbols denote the non-irradiated area and hollow symbols denote the irradiated area.
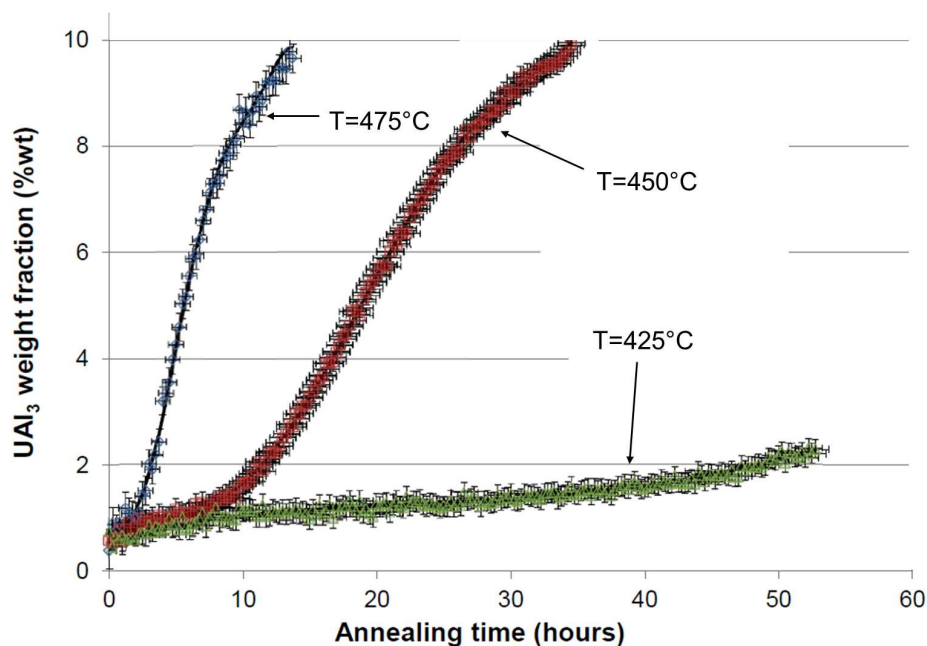
Figure 4.17: In-situ annealing-XRD experiment of UMo powder dispersion in an Al matrix shows that the UAl_3 formation starts slowly at around 425°C [107].
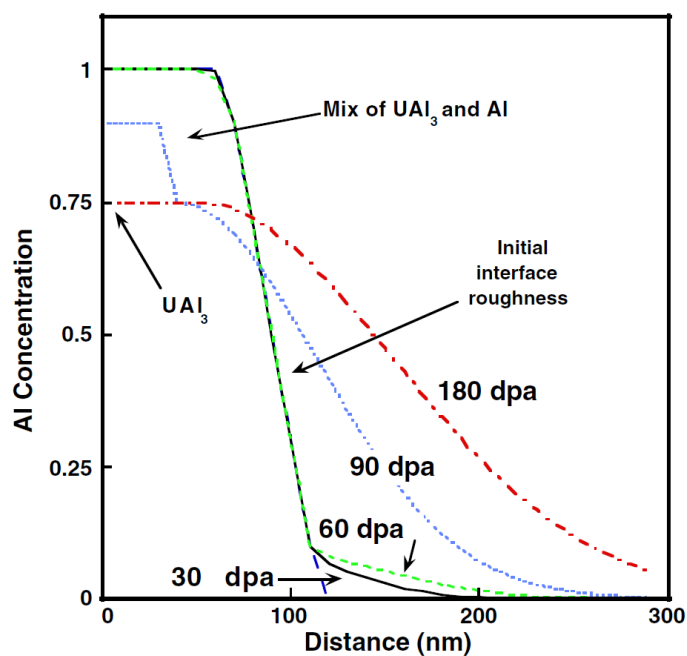
Figure 4.18: The Al concentration profile has been measured by Rutherford backscattering and the resonance nuclear reaction of $^{27}Al(p,c)^{28}Si$ reported by Birtcher and Baldo [108].
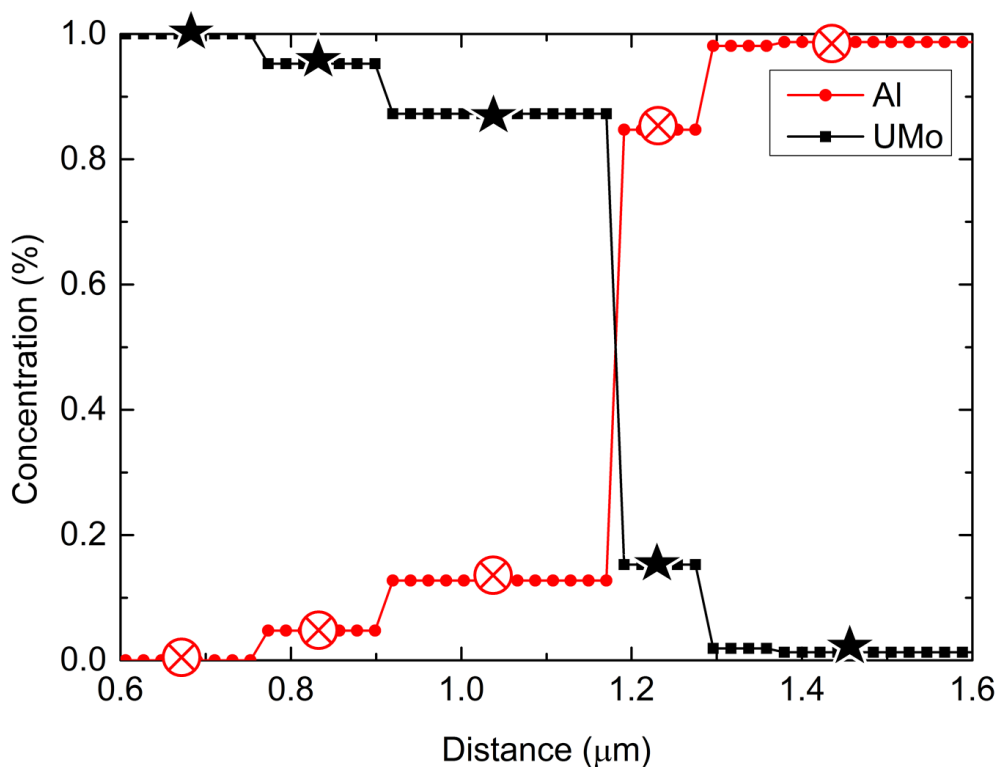
Figure 4.19: The elemental depth profiles of the UMo/Al bilayer after ion irradiation: in order to obtain the diffusion coefficients, the ternary system has then been simplified into a binary one with UMo and Al. Due to the binned data from SIMNRA, there are only 5 points at the interface which are labeled in the star sign and the circle with cross representing UMo and Al, receptively.
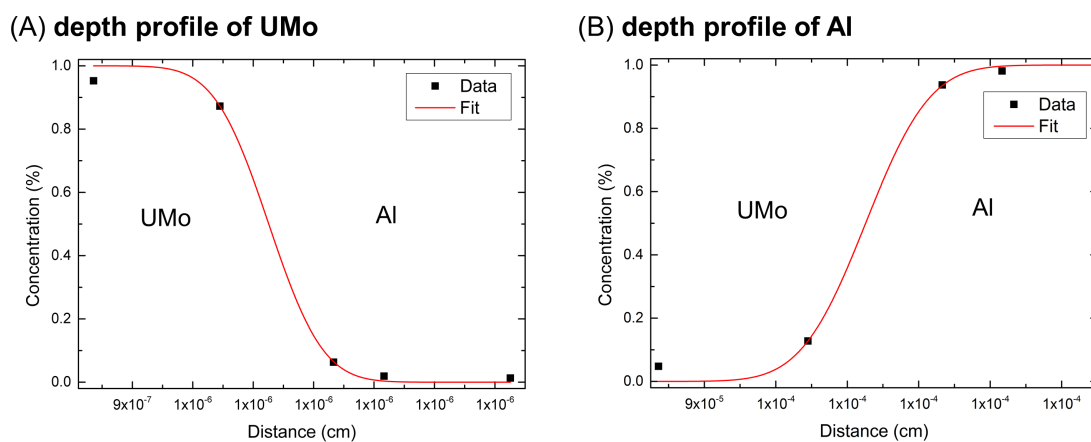
Figure 4.20: By exploiting Fick's 2nd law, Figure 4.19 has been fitted in terms of (A) UMo and (B) Al.

Chapter 5

Mg as The Matrix Material of UMo Fuels

5.1   Introduction

The U-Mo-Al interactions degenerate the irradiation performance of the UxMo/Al fuel causing swelling, a decrease of thermal conductivity, inability of accommodating fission gases, etc. In order to optimize the irradiation performance modifications on the UxMo/Al fuel have been proposed. Mg as the alternative matrix material has been considered because its low thermal neutron cross-section is comparable to that of Al [60]. Mg is thermally immiscible with both U and Mo, so that the interaction induced during the hot fabrication process can be limited. The corresponding binary phase diagrams are shown in Figure 5.1. According to Keiser et al., the interaction between U7wt%Mo particles and Mg matrix is negligible during in-pile irradiation so that the degeneration of irradiation performance can be avoided [116]. In fact, such a fuel consisting of UMo particles dispersion in Mg matrix has already been used in Russian light water reactors (LWRs) in the 1950s [117]. The stability of UMo/Mg bilayer has been tested by swift heavy ion irradiation. The irradiation has carried out at 140°C and 200°C which are the maximum temperatures in the meat of plate-like fuel, i.e. FRM II [69] and pin type fuel, e.g. HANARO [70] of research reactors during operation, respectively.

5.2   Sampling

The UMo/Mg bilayers involved in this investigation are composed of a UMo layer ($1\mu m$) upon a Mg substrate, preparing by DC-magnetron sputtering. Afterwards, the UMo/Mg bilayer were irradiated by ^{127}I ions at 80 MeV, reaching a final fluence of 10^{17} $ions/cm^2$ at a temperature of 140 ± 2°C and 200 ± 2°C, respectively. For μ-XRD and STEM measurements, thin films of the UMo/Al bilayers were carried out by FIB milling to reach the final thickness of 2 μm and 100 nm, respectively.
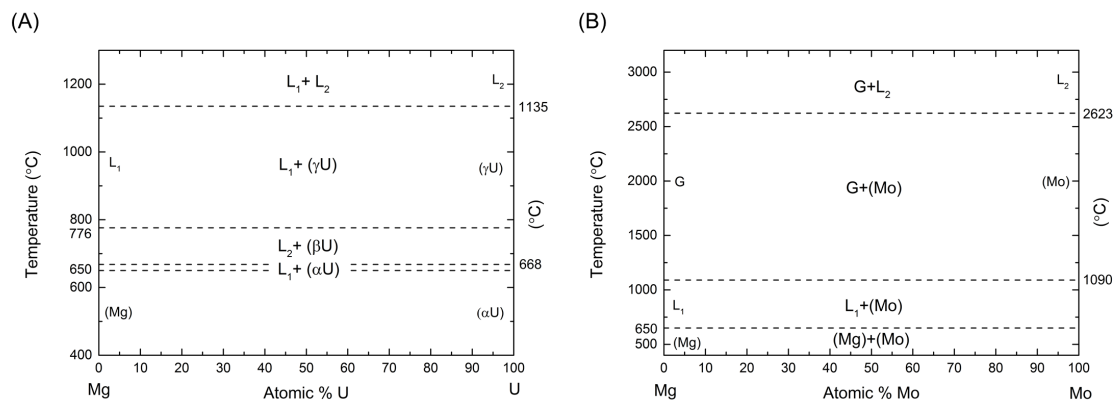
Figure 5.1: Phase diagrams of the Mg-U (A) and the Mg-Mo (B) binary systems indicate the thermal immiscibility of Mg toward both U and Mo [115].

5.3   TRIM calculations: ion-solid interactions

The UMo/Mg bilayers have been irradiated by ^{127}I ions at 80 MeV perpendicularly. Monte Carlo calculations of the stopping range of ions in matter (SRIM calculations [86]) predict a mean penetration depth of ^{127}I of 15.9 μm in the UMo/Mg bilayer (Figure 5.2A). The stopping powers along the trajectory are illustrated in Figure 5.2B. This indicates that most of the incident energy loss results from electronic stopping power.
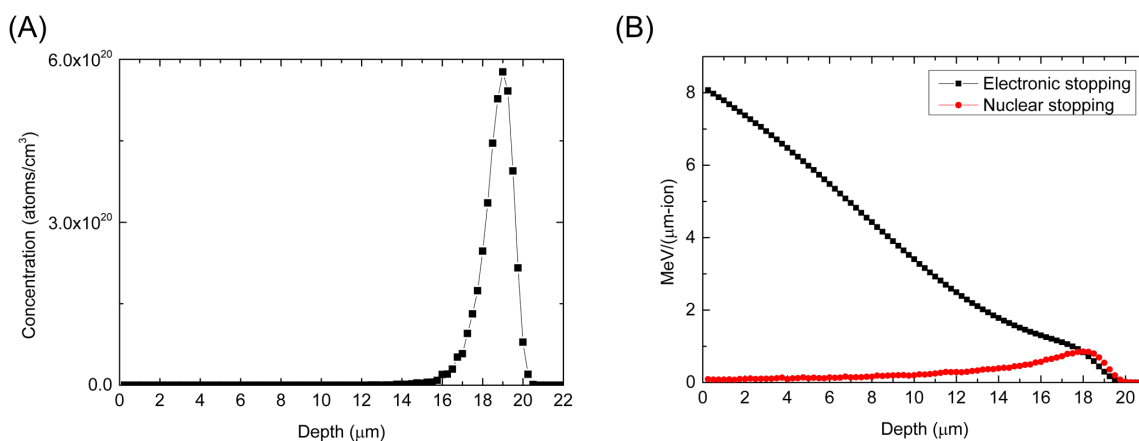
Figure 5.2: Calculated ^{127}I distribution (A) and ^{127}I energy loss (B) inside a thin UMo layer (1 μm) onto a Mg substrate. SRIM simulation of this sample irradiation with a 80 MeV ^{127}I beam up to a fluence of 10^{17} $ions/cm^2$.

5.4   Microstructural modifications

An overview of the UMo/Mg bilayer irradiated at 140°C in bright field is shown in Figure 5.3. It consists of 3 regions: UMo, the interfacial region and Mg. Each region has been characterized by electron diffraction and the diffraction patterns are labeled in corresponding areas. In the UMo region, the SADP with a diameter of 200 nm

shows a single crystalline pattern of UMo (space group symmetry: Im-3m), i.e. 110 reflection of γ-UMo, and Debye-Scherrer rings of UO_2 (Fm-3m). The grain size of this polycrystalline UO_2 is about 6.5 nm as determined by the Scherrer equation (Eq. 4.1). These polycrystalline UO_2 comes from oxidation of recrystallized UMo particles. The interfacial region consists of two layers: the upper one and the lower one. The SADP at the upper interface indicates the existence of UO_2 (Fm-3m), UO_2 (Pbca) and MgO (Fm-3m). High resolution bright field images with a higher magnification have been taken at the UMo/Mg interface as shown in Figure 5.4. The upper interface (Figure 5.4B) exhibits a ploycrystalline structure with a grain size about 4 - 5 nm in diameter (encircled by dashed lines) which is similar to the grain size of UO_2 estimated by Scherrer equation. A fast Fourier transformation (FFT) has been made out of Figure 5.4B as shown in Figure 5.4C confirms the polycrystalline structure. As for the lower interfacial area, due to the limitation of the aperture size a SADP could not be achieved. However, an FFT out of the high resolution TEM image indicates amorphization at this lower interfacial region. SADP of the Mg region reveals polycrystalline MgO (Fm-3m). The strong oxidation is mainly caused by the ambient storage of the thin foil.

μ-XRD patterns have been acquired at the UMo and at the interfacial region of the irradiated UMo/Mg bilayer (T= 140°C). The diffraction pattern of the Mg region is not available because of the low signal statistics. This is due to the difference of atomic scattering factor f and the extremely thin overall thickness of the thin foil ($\sim 2 \ \mu$m) exposed by a relative high X-ray energy of 21 keV. XRD patterns of the UMo/Mg bilayer irradiated 140°C are shown in Figure 5.5. The diffraction pattern taken at the UMo region (Figure 5.5A) indicates three phases: UMo (Im-3m) with the lattice parameter a = 0.3411 (1) nm, UO_2 (Fm-3m), and Cu from the grid. The Scherrer equation indicates that the grain sizes of UMo and UO_2 are 117 nm and 128 nm, respectively. The XRD pattern from the interface (Figure 5.5B) indicates UMo (Im-3m), MgO (Fm-3m), $UO_{2.12}$, Mg ($P6_3/mmc$), and Cu. There is no irradiation induced phase detectable at the UMo/Mg interface. The grain sizes of UMo, MgO, $UO_{2.12}$, and Mg estimated by the Scherrer equation are 47 nm, 93 nm, 57 nm, and 284 nm, respectively. Please note that there is a discrepancy in the grain size obtaining from STEM (Sec. 5.4) and from μ-XRD. This discrepancy results from different beam sizes and different methods of measuring the peak broadening applied in the Scherrer equation. Nevertheless, a comparison of the grain size can be made in the respective characterization.

A bright field image of the UMo/Mg bilayer irradiated at 200°C is shown in Figure 5.6. It consists of 4 regions: UMo, interfacial region 1, interfacial region 2, and Mg. At the UMo region, the SADP shows a single crystalline pattern of UMo (Im-3m) of 110 reflection and a polycrystalline UO_2 (Fm-3m) with an estimated grain size of about 4.5 nm based on the Scherrer equation. At the interfacial region 1, the SADP features Debye-Scherrer rings of both UMo (Im-3m) and UO_2 (Fm-3m). This indicates that UMo at the interface 1 has been completely powdered during the recrystallization process. The SADP of the interfacial region 2 displays polycrystalline UO_2 (Fm-3m) and polycrystalline MgO (Fm-3m), as well. Besides, an diffusing ring is visible, which corresponds to an estimated nearest neighbor distance of 0.265 - 0.295 nm. Due to the overlap of the diffusing ring and some reflection points, it is deduced that the ring comes from both partially amorphization and the particle size of nanocrystalline UO_2. Similar to interface 2, SADP at the Mg indicates polycrystalline pattern of MgO (Fm-3m),
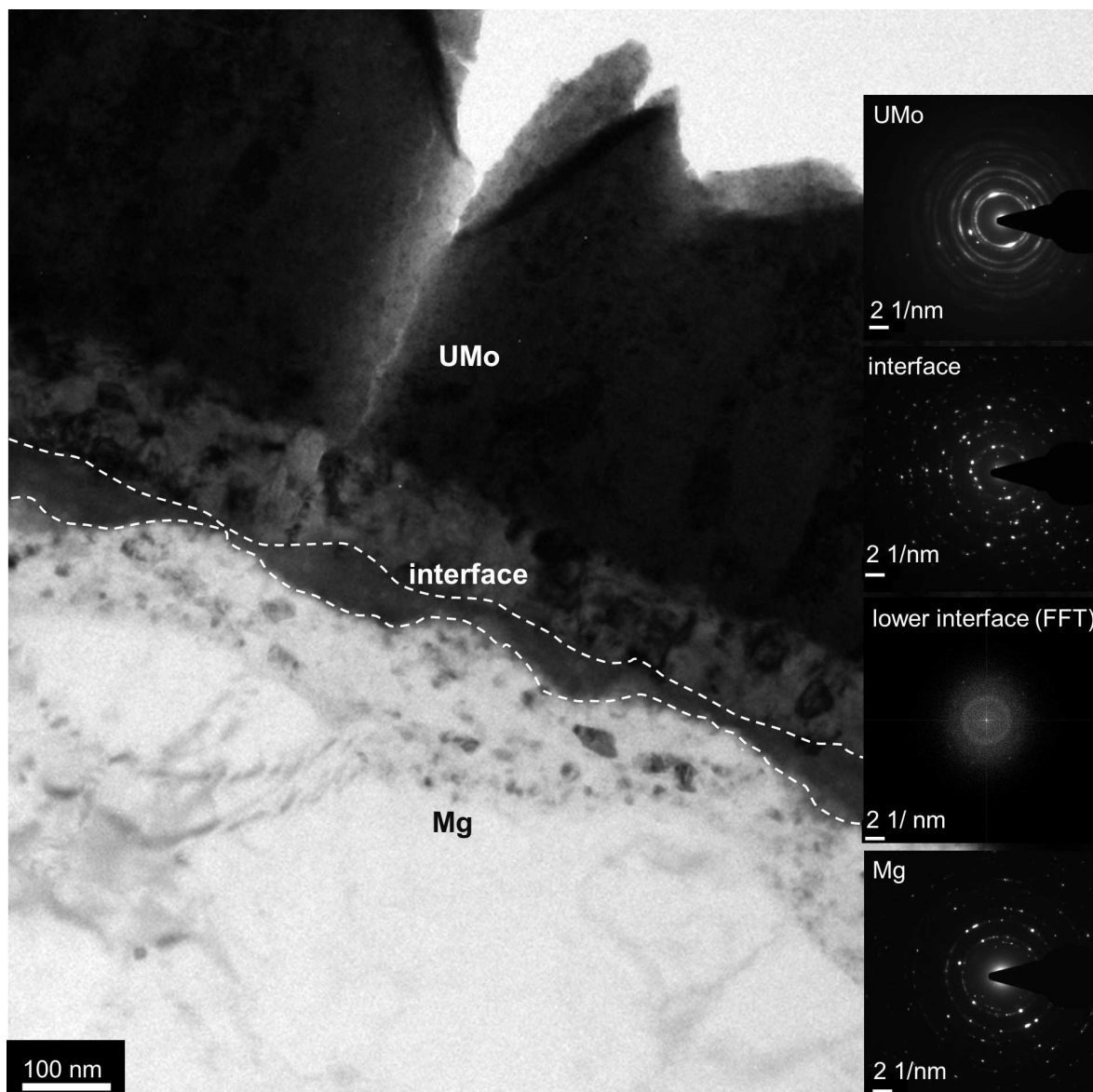
Figure 5.3: The overview of the UMo/Mg bilayer irradiated at 140°C has been taken in bright field and the SADPs have been performed at different regions, i.e. the UMo, the interface, and the Mg substrate. The SADP at the lower interface (marked with dashed lines) cannot be carried out due to the limited aperture size. However, a FFT has been made using a high resolution bright field image and it indicates the lower interface has been amorphized.

UO (Fm-3m) and UO_3 (C2mm) along with an amorphous ring indicating the nearest neighbor distance of 0.280 - 0.329 nm. Further 80 nm into the Mg region, a chessboard-like pattern is observed which is a typical feature of spinodal decomposition (Sec. 2.4.2). This spinodal-decomposed region has been characterized by STEM-HAADF (Figure 5.7A) and based on the Z-contrast it has been found that some precipitates located in the upper spinodal decomposed region. When an alloy is supersaturated, precipitation of the excess composition through the formation of precipitates will markedly decrease the free energy and this can be expected to occur spontaneously. By increasing the magnification a high resolution bright field image (Figure 5.7B) exhibits fringes and
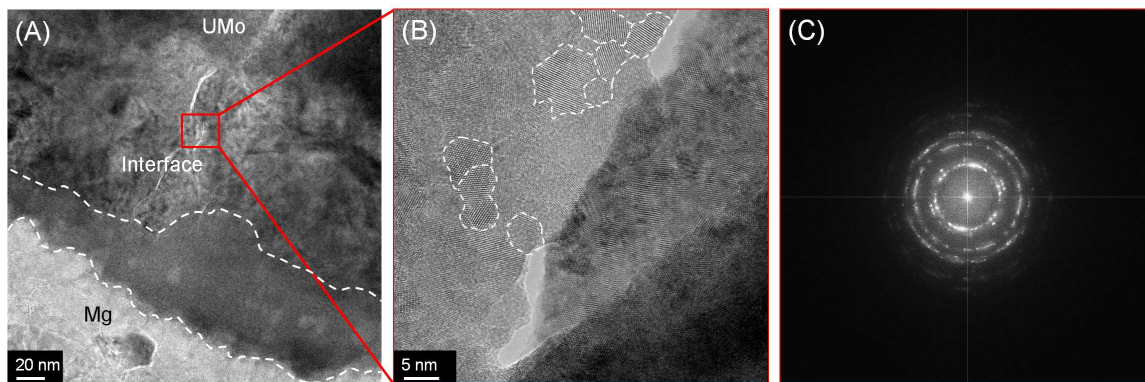
Figure 5.4: High resolution bright field images have been taken at (A) the UMo/Mg interface which consists of the UMo, the interface and the Mg region. The interfacial region has been magnified as shown in (B) which exhibits a ploycrystalline structure with a grain size about 4 - 5 nm in diameter (encircled by dashed lines). A fast Fourier transformation (FFT) made out of (B) as shown in (C) confirms the polycrystalline structure.

dots indicating mass-thickness variations. A FFT based on this high resolution bright field image indicates the amorphous structure with some residual crystallinity as shown in Figure 5.7C.

XRD patterns of the UMo/Mg bilayer irradiated at 200°C are presented in Figure 5.8. The XRD pattern of Figure 5.8A taken at the UMo region shows three phases: UMo (Im-3m) with a = 0.3413(3) nm, UO_2 (Fm-3m), and Cu. Using Scherrer equation, the grain sizes of UMo and UO_2 are estimated to be 84 nm and 304 nm, respectively. As shown in Figure 5.8B, the XRD pattern at the interface of the UMo/Mg bilayer consists of $U_{0.9}Mg_{0.1}$ alloy in BCC structure with a = 0.3313(1) nm and Cu from the grid. The broadening of Debye-Scherrer rings points out the poor crystalline state of $U_{0.9}Mg_{0.1}$ and the grain size is about 16 nm estimated by the Scherrer equation. A further XRD probing into the Mg region reveals four phases: $U_{0.9}Mg_{0.1}$ (Im-3m), $Mg_{1-\bar{a}}U_{\bar{a}}$ ($P6_3/mmc$), Mg ($P6_3/mmc$) and Cu from the grid (Figure 5.9). $Mg_{1-\bar{a}}U_{\bar{a}}$ is an averaged pattern from the spinodally decomposed phases whereas $U_{0.9}Mg_{0.1}$ and Mg originate from the neighboring area and Cu. The grain sizes of $U_{0.9}Mg_{0.1}$, Mg, and $Mg_{1-\bar{a}}U_{\bar{a}}$ estimated by the Scherrer equation are 20 nm, 28 nm, and 39 nm, respectively. One peak at 22.2° cannot be assigned. The identification of $U_{0.9}Mg_{0.1}$ and $Mg_{1-\bar{a}}U_{\bar{a}}$ will be discussed in details in Sec. 5.5.

5.4.1   Chemical analysis

Results from EDX linescan across the interface of the UMo/Mg bilayer irradiated at 140°C and the corresponding STEM-HAADF image are shown in Figure 5.10. This observation demonstrates that amorphization only occurred at the U-Mo-Mg intermixed region. Based on the Z-contrast of STEM-HAADF image, the amorphous region observed in the lower interface corresponds to the first plateau of Mg at the distance of 250 nm in EDX linescan. The amorphous region can be determined by the size of the Mg plateau at the interface in the concentration profile. At 140°C, the amorphous

region is about 50 nm (from the distance of 230 nm – 280 nm).

At the UMo/Mg bilayer irradiated at 200°C, two EDX linescans have been made. The EDX linescan taken across the interfaces and the corresponding STEM-HAADF image are shown in Figure 5.11. The amorphous layer found at the interface 2 corresponds to the first plateau of Mg at the distance of 200 nm and the amorphous region is about 110 nm, i.e. from the distance of 160 – 270 nm, in Figure 5.11B. . The size of the amorphous region increases with increasing irradiation temperature. The second linescan has been made across the chessboard-like pattern at the upper Mg as shown in Figure 5.12. Two phases $Mg_{1-a}U_a$ and $Mg_{1-b}U_b$ are discernible. The stripe-like pattern corresponds to a U-rich phase, i.e. $Mg_{1-a}U_a$ while the rhomb is related to a U-poor phase, i.e. $Mg_{1-b}U_b$. This chessboard-like pattern and its compositional variation are typical for spinodal decomposition.

5.5 Discussion

The modifications of the UMo/Mg bilayer are structurally and chemically driven by swift heavy ion irradiation. SRIM calculations indicate that incident ^{127}I ions deposit the kinetic energy primarily by electronic stopping, i.e. by excitation and ionization of the target atoms along the trajectory. These electronic collisions turn into heat dissipation which enables the formation of local molten zones, i.e. thermal spikes [118]. Direct atomic displacements by nuclear collisions are less prominent even though the damages created by ion irradiation are estimated to be more than 50 displacements per atom (dpa) based on SRIM calculations. At an adequate dose, enough mixing is achieved and the mixture of U, Mo and Mg atoms is most likely in a highly energetic disordered state. Once the ion irradiation is over, this highly energetic state starts to relax towards equilibrium within a short time, e.g. 10^{-10} s. Therefore, a limited number of atoms relax to the equilibrium positions. The mixture might stay in metastable state as an amorphous solid solution or decompose into multiple phases.

5.5.1 Amorphization

^{127}I irradiated UMo/Mg bilayers exhibit an amorphous structure at the intermixed region of U, Mo and Mg. This amorphization can be explained by the limited solubility of U and Mo into Mg. Brinhall et al. have reported that compounds with limited compositional range or solubility tend to become amorphous; in contrary to those compounds with wide solubility remain crystalline [54]. A correlation between the formation of amorphous phase and the compositional range is consistent with the concept of a threshold of defect concentration for amorphization. It is assumed that the structure would transform or relax into the amorphous state spontaneously if the irradiation could produce a critical defect concentration, i.e. whenever the total free energy of defect crystalline state is greater than that of the amorphous state. The increase in free energy is due to the inability of the compound to exist in equilibrium outside the designated composition. In addition, the criterion Eq. 2.8 for amorphization proposed by Naguib and Kelly utilize ionicity holds for the U/Mg case. The electronegativities

of U, Mo and Mg are 1.38, 2.16 and 1.31, respectively. The ionicity of the U/Mg inter-metallics is $1.2 \times 10^{-3} \leq 0.1$ which meets the N-K ionicity rule. However, the Mo/Mg intermetallics does not satisfy this rule with the ionicity of $0.17 \geq 0.1$. One should note that the Mo content in the UMo layer is only $\sim 15\%$.

5.5.2   U-Mg solid solution

As shown in Figure 5.8A and 5.8B, XRD at the interface of the UMo/Mg bilayer irradiated at 200°C indicates an unknown alloy phase (denoted as UX) with the refined lattice parameter a = 0.3131(1) nm. Its isostructural UxMo alloys have larger lattices parameters with a = $0.335 - 0.348$ nm [101, 119] and the lattice parameter of UMo decreases with the increasing Mo content in solid solution. When the lattice constant of UMo is less than 0.335 nm, a segregation of Mo or a formation of U_2Mo occur. However, none of these two phases has been observed in the μ-XRD pattern. Therefore, one can consider this UX phase is a U-Mo-Mg ternary alloy based on the EDX measurement (Figure 5.11) or a U-Mg binary alloy. Mg is thermally immiscible to both U and Mo and therefore the corresponding enthalpies of formation ΔH_f of the Mg-U and the Mg-Mo binary systems, calculated by Miedema's model [61, 62, 64, 65], are positive against any interaction. However, ΔH_f in the U-Mg binary system is smaller than that in the Mo-Mg binary system as shown in Figure 5.13. When considering a large positive enthalpy of formation $\Delta H_f = +50$ kJ/mol required for the formation in the Mo-Mg binary system, solid solution of Mo and Mg can be excluded. Therefore, U and Mg are considered to be the dominant constituents in this alloy. For this reason, we tentatively assigned the UX phase to U_xMg_y occurring as the main phase in Figure 5.8B. Indexing of μ-XRD pattern allowed a body-centered cubic (BCC) structure and the subsequent Rietveld analysis confirmed the stoichiometry $U_{0.9}Mg_{0.1}$.

5.5.3   Spinodal decomposition

The UMo/Mg bilayer experienced swift heavy ion irradiation at higher temperature, i.e. 200°C exhibits a compositional variation with a period of about 50 nm as shown in Figure 5.12A. This is a typical feature of spinodal decomposition. Another feature of spinodal decomposition is satellite reflections around the main diffraction peak [120]. In Figure 5.14, An overview of TEM bright field image has been taken at the spinodally decomposed region. SADPs at different area (marked as a, b, and c) show the satellite diffraction: diffraction spots surrounding the main diffraction peak. The interval between the main diffraction and the satellite one in the SADP decreases as the SADP moves away from the spinodally decomposed region. The satellite reflection comes from composition modulation of Mg. Spinodal decomposition describes a solution decomposing into multiple phases due to the limited solubility, i.e. boundary of absolute instability. The intermediate U-Mg phase induced by irradiation undergoes spinodal decomposition into two phases $Mg_{1-a}U_a$ and $Mg_{1-b}U_b$. Both phases could crystallize in the same space group, i.e. $P6_3/mmc$ to minimize coherency strains. Due to the limited spatial resolution, μ-XRD could only discriminate an averaged patterns

$Mg_{1-\bar{a}}U_{\bar{a}}$ from two spinodally decomposed phases $Mg_{1-a}U_a$ and $Mg_{1-b}U_b$ (Figure 5.9). The U content of the averaged patterns $Mg_{1-\bar{a}}U_{\bar{a}}$ is estimated to be 2 ± 1 at% and 6 ± 2 at% by Rietveld analysis and by EDX, respectively. These arguable values can be improved by further investigation in particular nano-focusing diffraction equipped with an energy-dispersion detector.

Spinodal decomposition in the U-Mg binary system can be explained by thermodynamics. From the thermodynamic point of view, irradiation in an immiscible system with a positive ΔH_f can encourage spinodal decomposition. Having $\Delta H_f = +17$ kJ/mol the U-Mg system could be driven to the consequent phase decomposition. Miedema [61] and related considerations [64, 65, 121] are applied to calculate the free energy change ΔG in the U-Mg binary system for a postulated decomposition into a metastable crystalline and amorphous phase. The free energy change for a metastable crystalline phase, i.e. ΔG_c is expressed as

$$\Delta G_c = \Delta H_c^c + \Delta H_c^e + \Delta H_c^s - T\Delta S \tag{5.1}$$

where ΔH_c is the chemical formation enthalpy, ΔH_e is the elastic mismatch enthalpy, ΔH_s is the structural formation enthalpy, and ΔS is the entropy change. Here we consider two possible crystal structures, i.e. BCC and hexagonal closed pack (HCP) which correspond to the structure of pure Mg and U, respectively. For an amorphous phase, its free energy change is expressed by

$$\Delta G_a = \Delta H^c + \alpha(x_A T_{m,A} + x_B T_{m,B}) - T\Delta S \tag{5.2}$$

where α is an empirical constant with a value of 3.5 $J/mol \cdot K$, and T_m is the melting point of the component metal. Figure 5.15 demonstrates ΔG calculated for the formation of the considered crystalline and amorphous phase for U-Mg solid solution. The free energy of the amorphous U-Mg solid solution is higher than that for the crystalline HCP-type U-Mg solid solution. The difference ΔG can be the driving force for spinodal decomposition from an amorphous structure into two HCP phases, i.e. $Mg_{1-a}U_a$ and $Mg_{1-b}U_b$.

Spinodal decomposed materials usually have a homogeneously distributed microstructure that can enhance mechanical strength of materials. However, a strength enhancement is usually accompanied by scarified ductility [122]. The limited ductility is mostly caused by the formation of grain boundaries. This decrease of ductility might be an issue in developing stable fuel materials which has to adapt to irradiation-induced strains. In addition to the ductility, spinodal decomposition might result in a deformation of the UMo/Mg bilayer as shown in Figure 5.16. Figure 5.16A is the UMo/Mg bilayer which was taken prior to the STEM characterization using SEM whereas two weeks after the STEM characterization the UMo/Mg bilayer exhibits a completely deformation (Figure 5.16B). This result shows that the spinodally-decomposed UMo/Mg bilayer is highly sensitive to the exposure of electron beams in STEM measurements. The instability of spinodally decomposed material should also be taken into consideration when evaluating the potential of UMo/Mg fuels.

5.5.4 Comparison with the UMo/Al bilayer

The amorphous region of the UMo/Mg bilayer increases by rising the irradiation temperature, e.g. ~ 50 nm at 140°C and ~ 110 nm at 200°C. Based on this observation,

one can deduce that during the intermixing process at the interface, atomic transport driven by thermal energy took place. In comparison to the UMo/Al bilayer mentioned in Chap. 4, the amorphous region in the UMo/Mg bilayer is of around $\frac{1}{20}$ and $\frac{1}{3}$ times thick than that in the UMo/Al bilayer under swift heavy ion irradiation at 140°C (Figure 5.17) and 200°C (Figure 5.18), respectively. Indeed, the UMo thicknesses of the UMo/Al and UMo/Mg bilayer are not the same so are the stopping powers. However, the incident energy dissipates majorly via electronic stopping power in most of these bilayers and therefore a reasonable comparison can be made. The thickness difference of the amorphous region arises from the different chemical affinities of the matrix materials towards U. During irradiation, thermal diffusion driven by chemical potentials is considered as the dominant migration process within the molten zones along the ion trajectory. In the U-Al binary system diffusion of U atoms into the Al matrix is favored. In the contrary, due to thermal immiscibility in the U-Mg binary system, diffusion reaction can be suppressed. For this reason the fuel performance can be improved by replacing the matrix material from Al to Mg.

5.6   Summary

The present study shows a suppression diffusion reactions and amorphization in the UMo/Mg bilayers after swift heavy ion irradiation. The amorphous region in the UMo/Mg is minor compared to the case with UMo/Al bilayers. Furthermore, the limited interdiffusion in the UMo/Mg bilayer is expected to oppresses the accumulation of fission gases so that the swelling effect could be minimized. The formation of amorphous phase promotes spinodal decomposition. At higher irradiation temperature, spinodal decomposition occurring at the intermixed region which may cause regression of ductility in fuel composites or a severe deformation. Therefore, we suggest further systematic studies of spinodal decomposition in UMo/Mg for fuels systems operating at higher temperatures. On the whole, this study concludes that the size of amorphous region in UMo alloy fuels can be reduced by replacing Mg for Al as a matrix material.
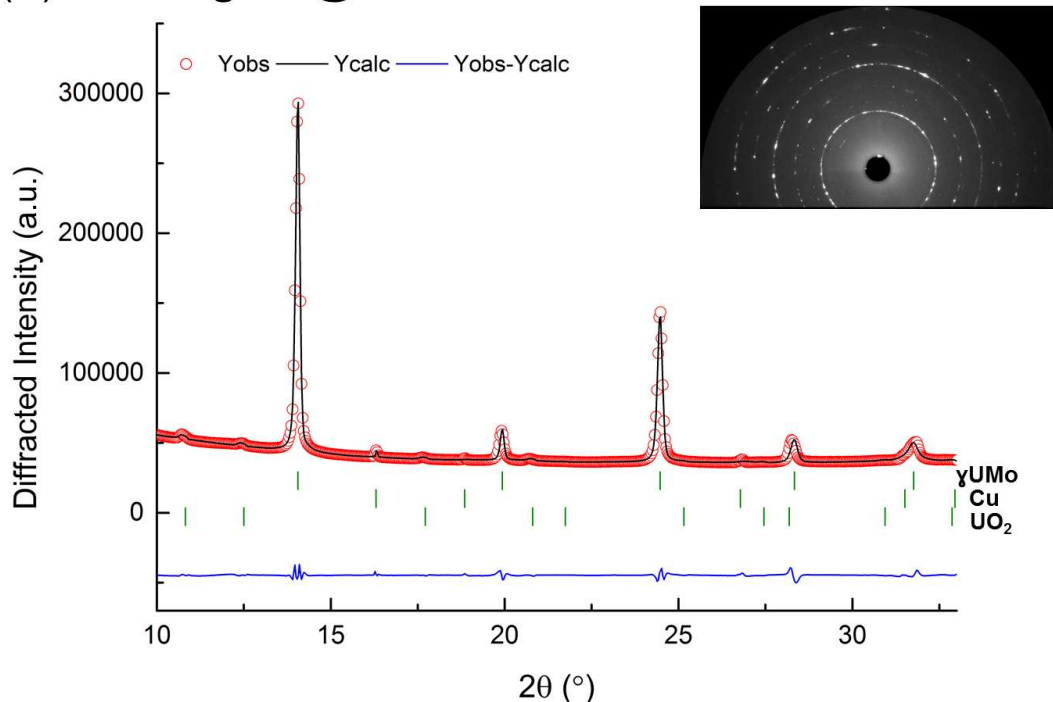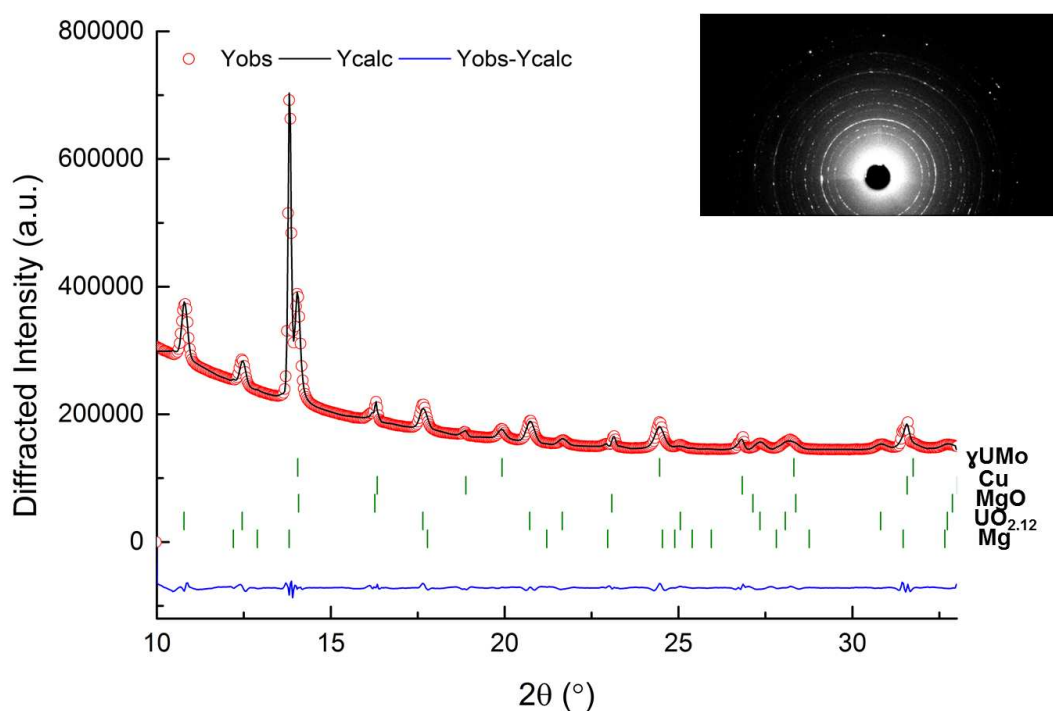
Figure 5.5: Observed (open circles) and calculated (solid line) μ-XRD patterns of (A) the UMo region and (B) the interfacial region of UMo/Mg bilayer irradiated at 140°C. The flat discrepancy profiles given at the bottom in (A) and (B) demonstrate well-performed Rietveld calculations with all identified phases (bars) at the UMo layer (UMo, U-oxide) and at the interface (UMo, MgO, U-oxide, and Mg) along with Cu from the sample grid.
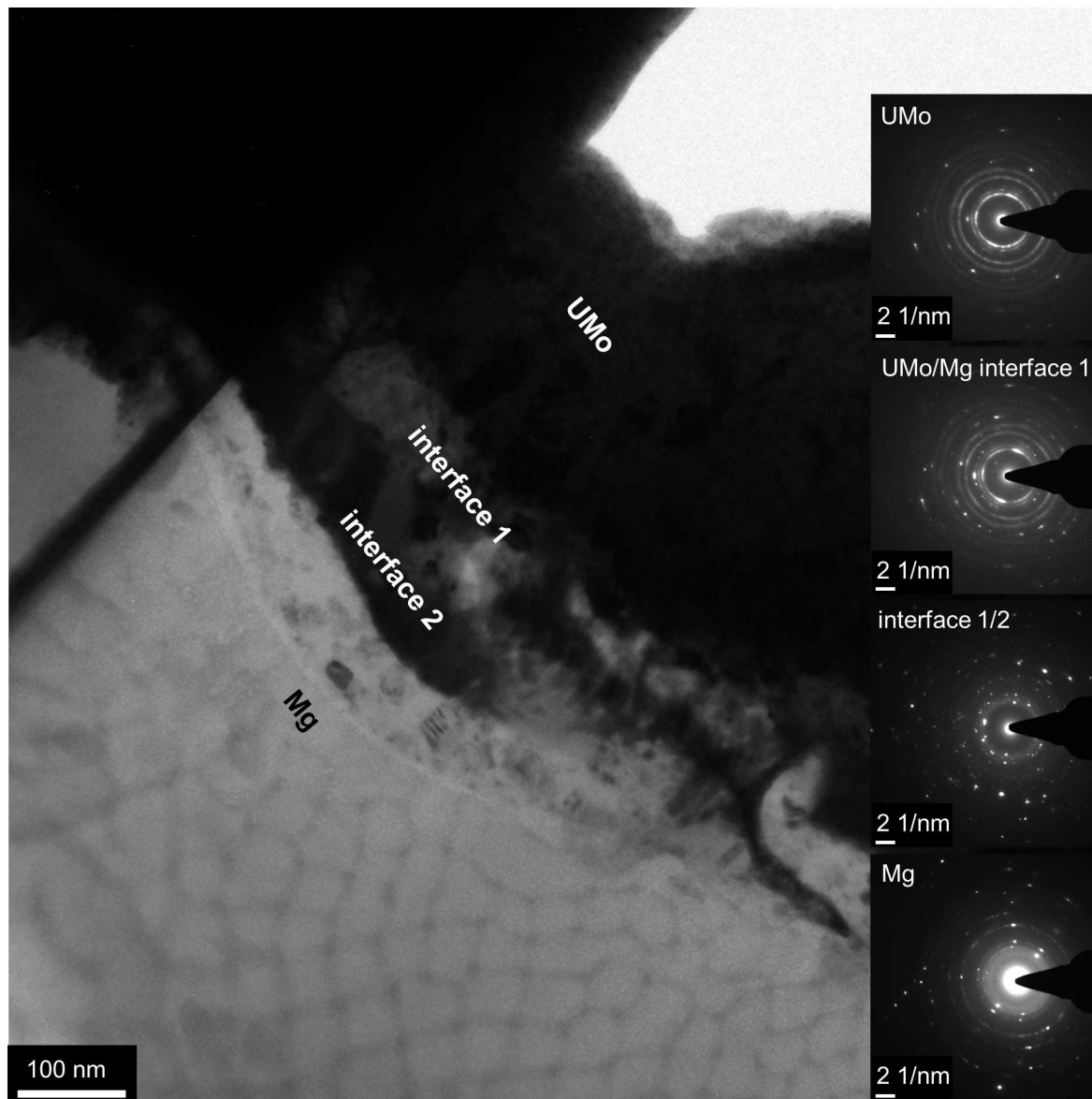
Figure 5.6: The overview of the UMo/Mg bilayer irradiated at 200°C has been taken in bright field and the SADPs have been performed at different regions, e.g. the UMo, the interface 1, the region between the interface 1 and the interface 2, and the Mg substrate. The SADPs performed at the interface 1/2 and the Mg region indicate the partial amorphization. A chessboard-like pattern has been observed at the Mg region and this pattern is identified as a spinodal decomposition pattern.
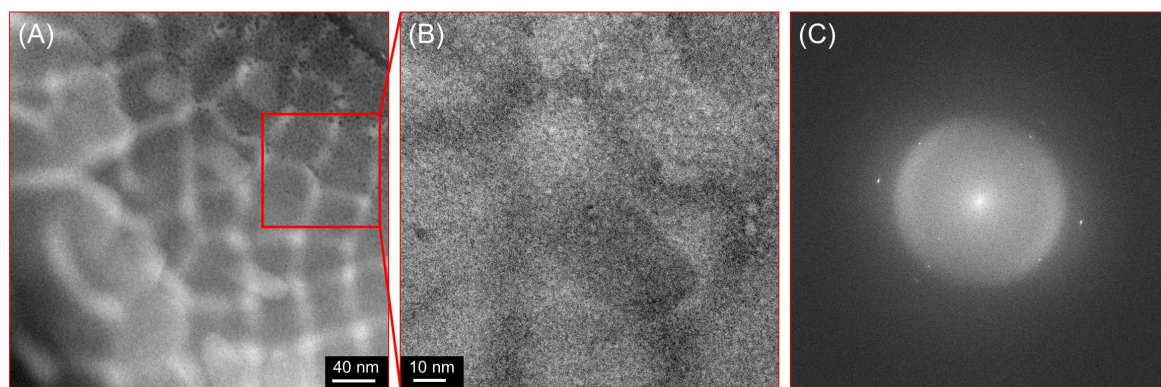
Figure 5.7: The spinodally decomposed region has been characterized by STEM-HAADF (A) and based on the Z-contrast it has been found that some precipitates located in the chessboard-like pattern. By increasing the magnification a high resolution bright field image (B) exhibits fringes and dots. A (C) FFT based on (B) indicates the amorphous structure with some residual crystallinity.
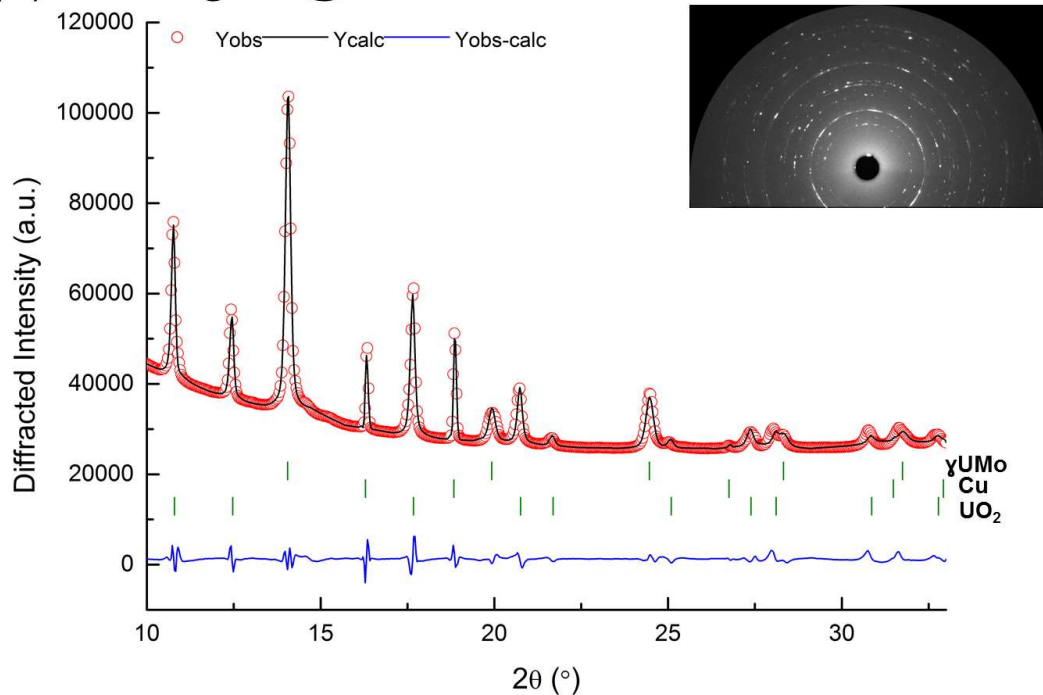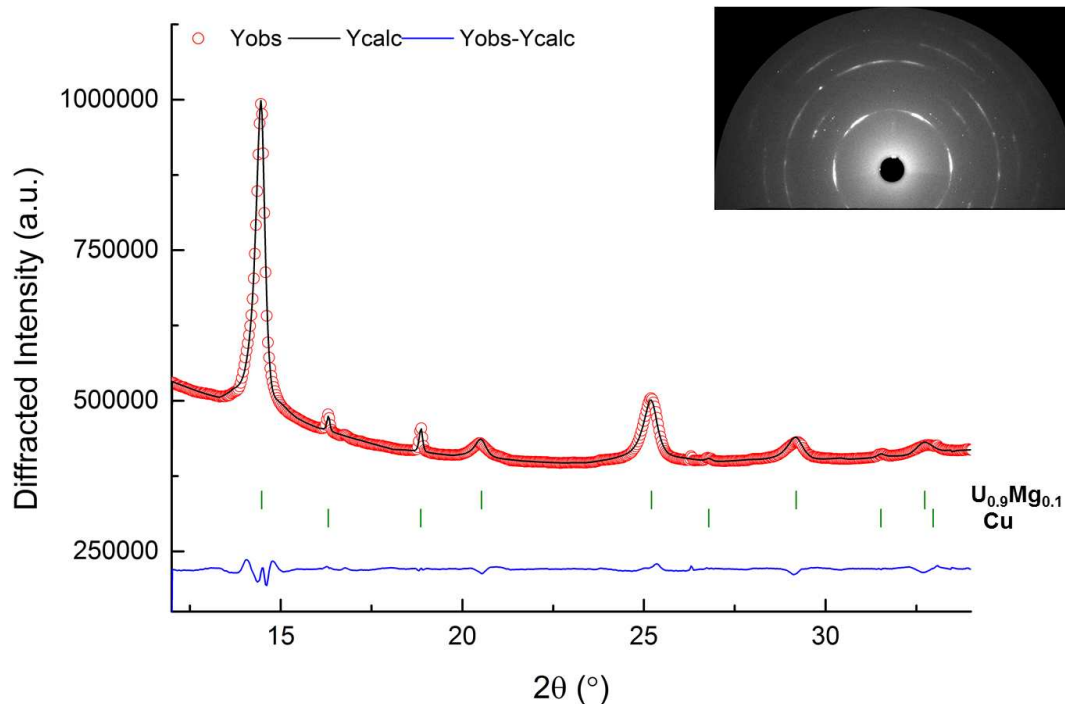
Figure 5.8: Observed (open circles) and calculated (solid line) μ-XRD patterns taken from (A) the UMo and (B) the interfacial region within the sample irradiated under 200°C. Rietveld analysis confirms UMo and U-oxide in the UMo layer and $U_{0.9}Mg_{0.1}$ at the interface.

(C) spinodal-decomposed region @ 200°C
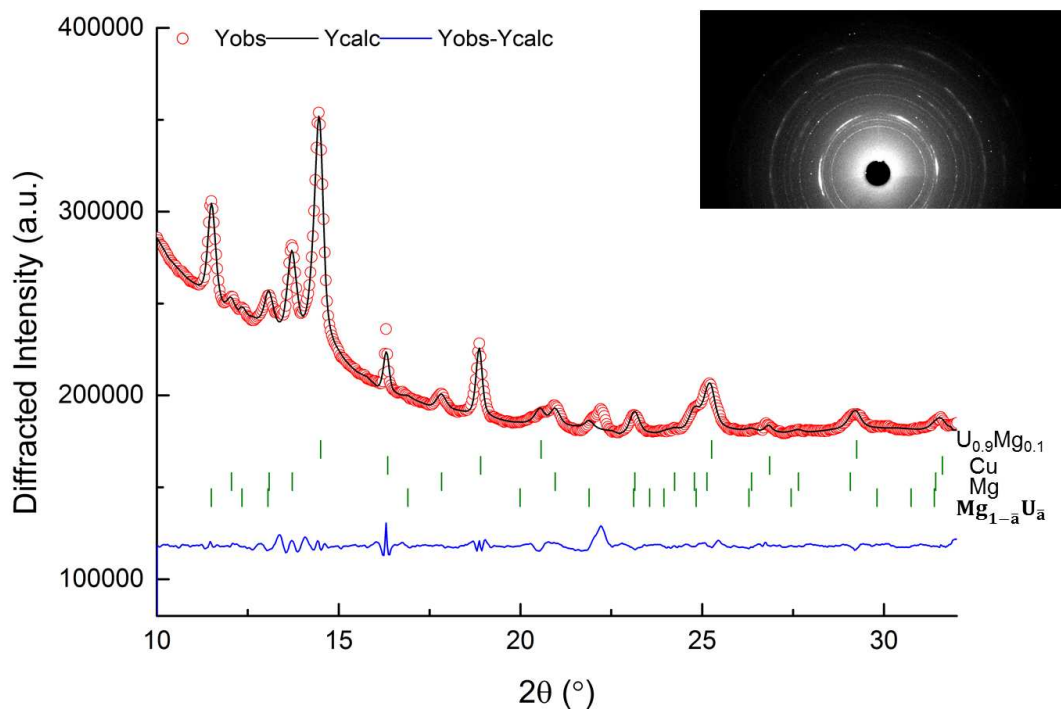
Figure 5.9: Observed (open circles) and calculated (solid line) μ-XRD patterns taken from the spinodal decomposed region within the sample irradiated under 200°C. Rietveld analysis confirms $U_{0.9}Mg_{0.1}$, Mg and $Mg_{1-\bar{a}}U_{\bar{a}}$ in the spinodally decomposed region.
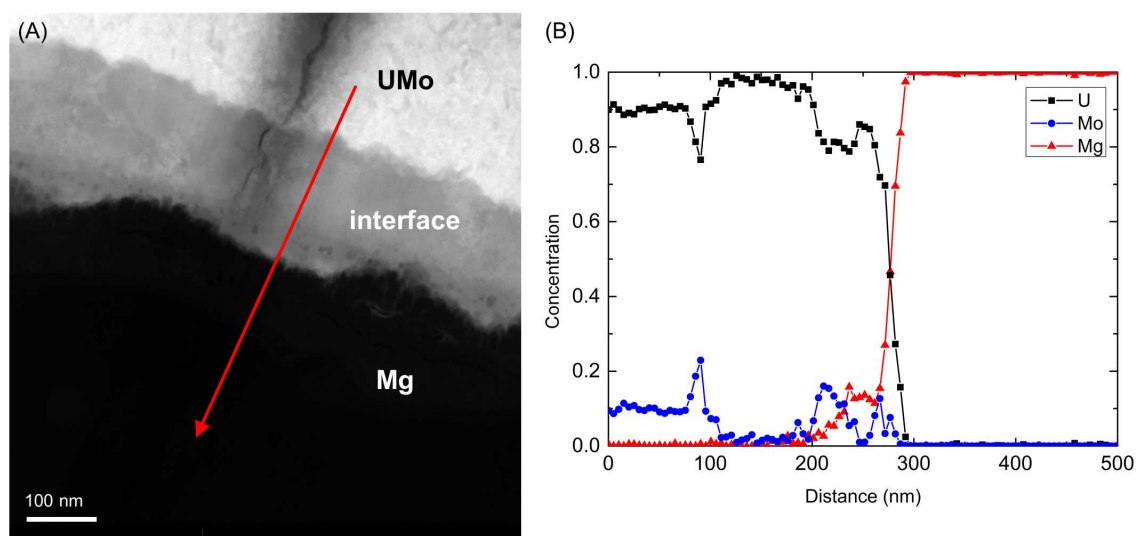
Figure 5.10: (A) a STEM-HAADF images showing an EDX linescan across the interface of the UMo/Mg bilayer irradiated at 140°C; (B) the variation of element concentrations across the EDX linescan.
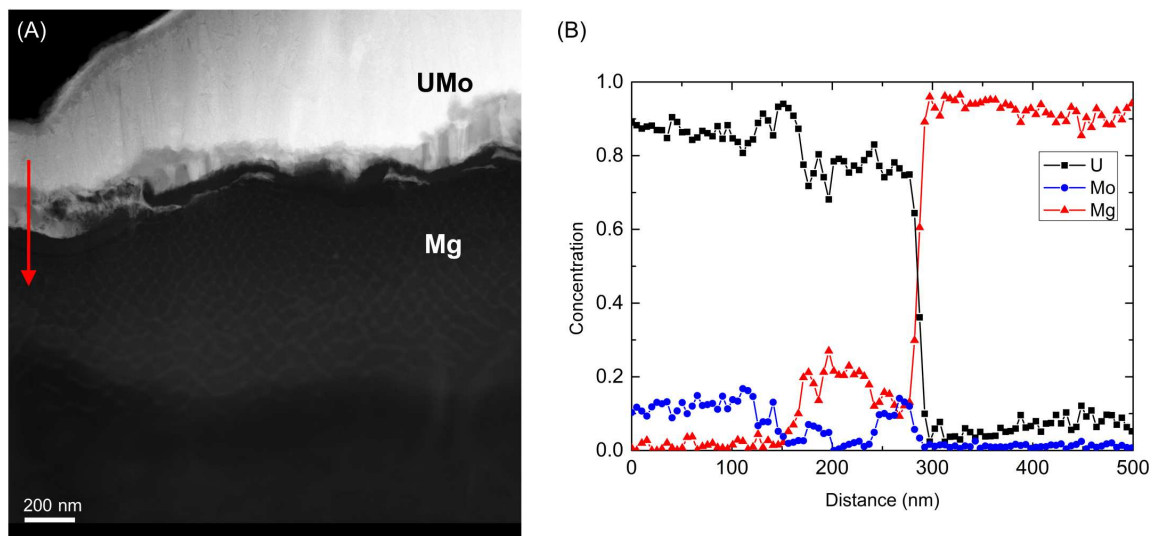
Figure 5.11: (A) a STEM HAADF of the interface of UMo/Mg bilayer irradiated at 200°C; (B) an EDX linescan across the layer indicated by arrow in (A) shows distinct chemical gradients (B).
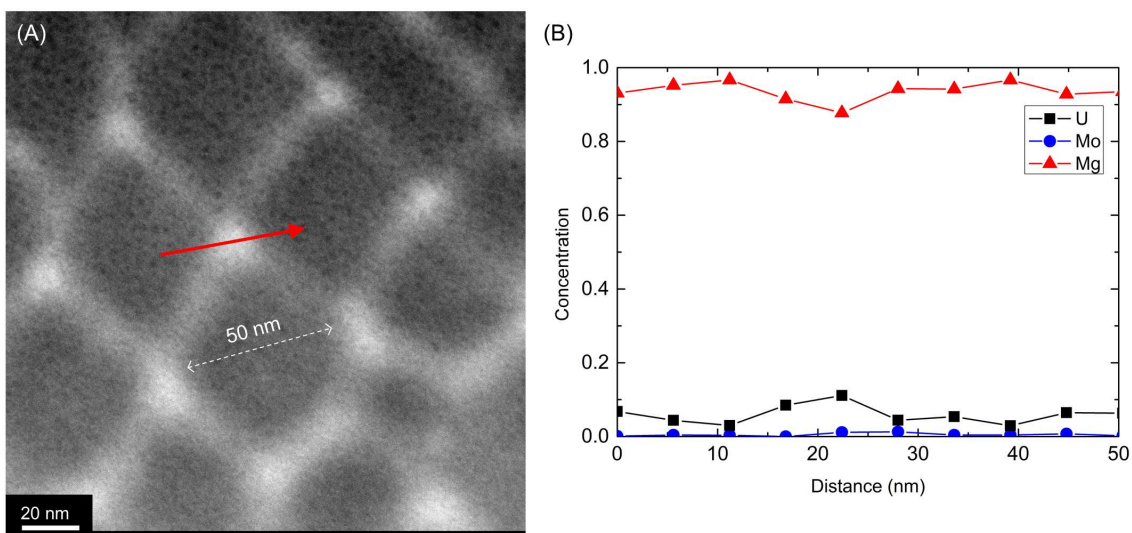
Figure 5.12: (A) a STEM-HAADF image of the spinodal pattern of UMo/Mg bilayer irradiated at 200°C shows a chessboard-like texture with dark rhombs bounded by bright stripes; (B) an EDX linescan across between two rhombs, as marked by the arrow in (A) indicates that bright stripes contain a higher U amount than dark rhombs (B). The period of the chessboard-like pattern is around 50 nm.
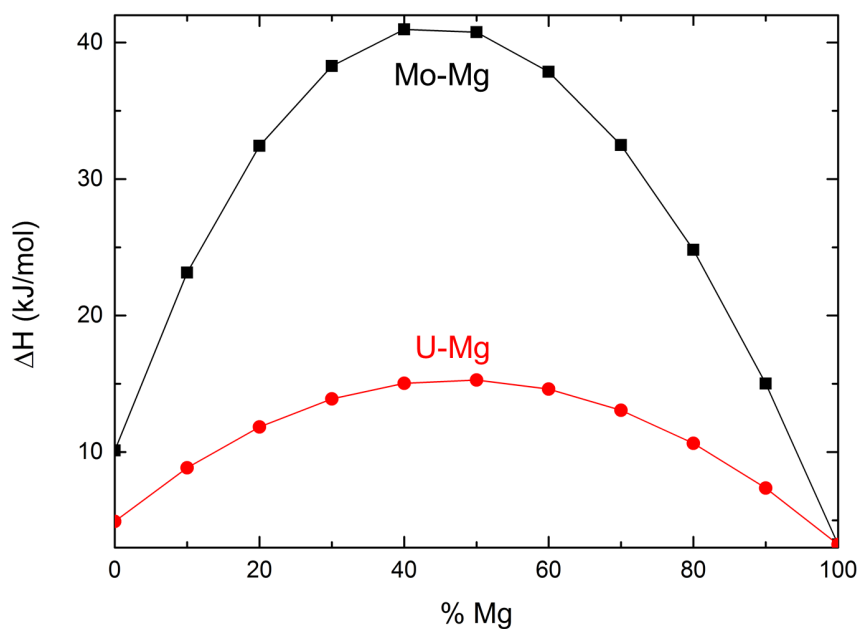
Figure 5.13: The enthalpies of mixing in the U-Mg and the Mo-Mg binary system have been calculated using Miedema model. As illustrated that both U and Mo are immiscible to Mg but the barrier in the Mg-U binary system is smaller than that in the Mg-Mo binary system.
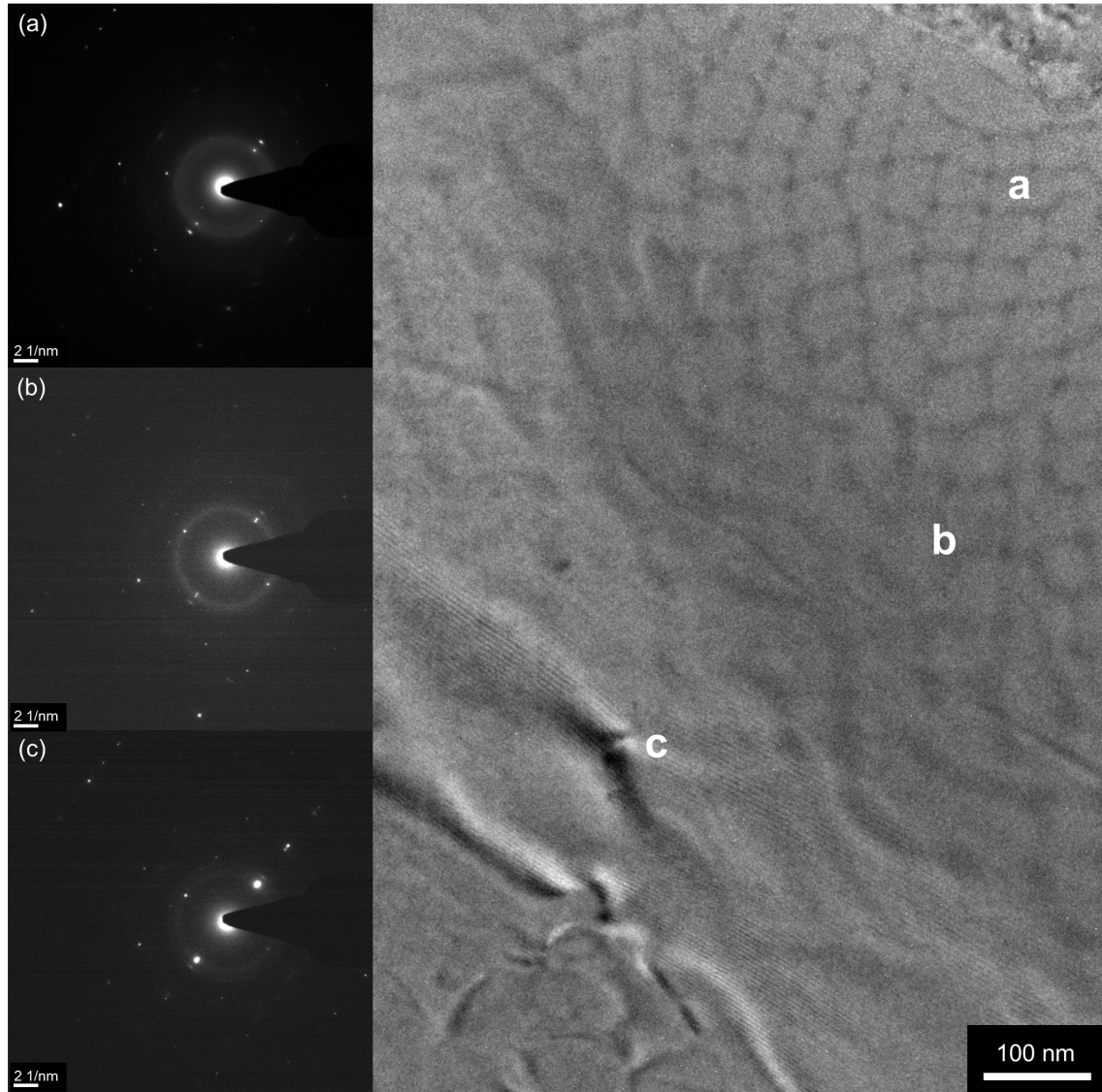
Figure 5.14: An overview of TEM bright field image has been taken at the spinodally decomposed region. The SADPs at different area (marked as a, b, and c) show the satellite diffraction which is one of the typical feature of spinodal decomposition.
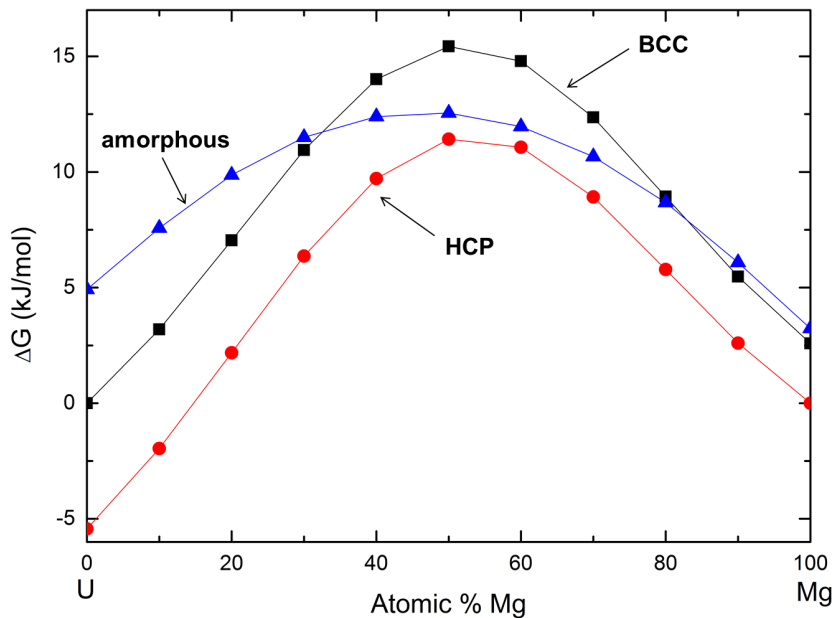
Figure 5.15: Free energy changes of U-Mg solid solution in the crystalline structures and an amorphous structure. BCC and HCP correspond to the crystal structures of pure Mg and U, respectively.
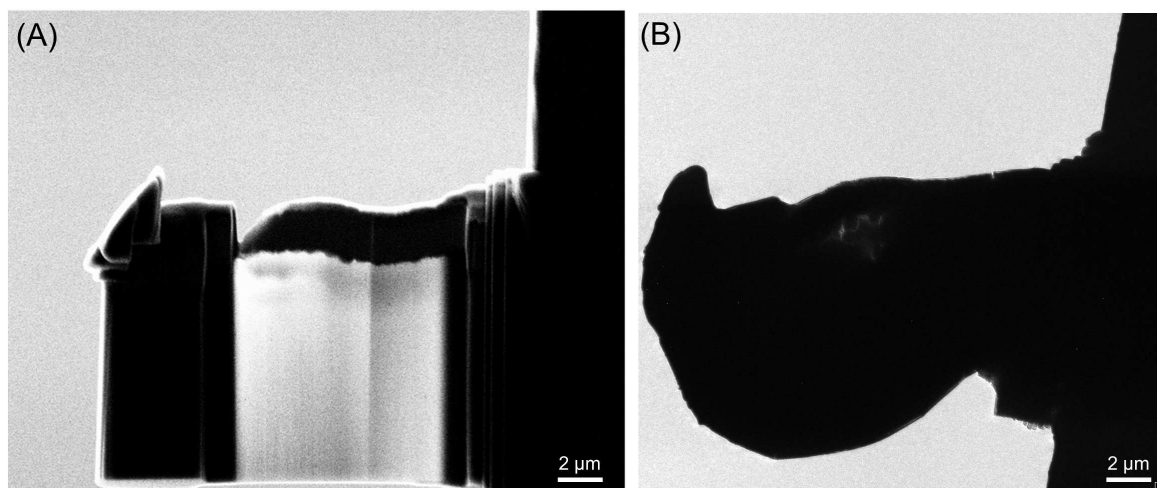
Figure 5.16: An overall image of the UMo/Mg bilayer (A) has been taken during prior to the first STEM characterization while two weeks after the STEM characterization the bilayer shows a completely deformation (B).
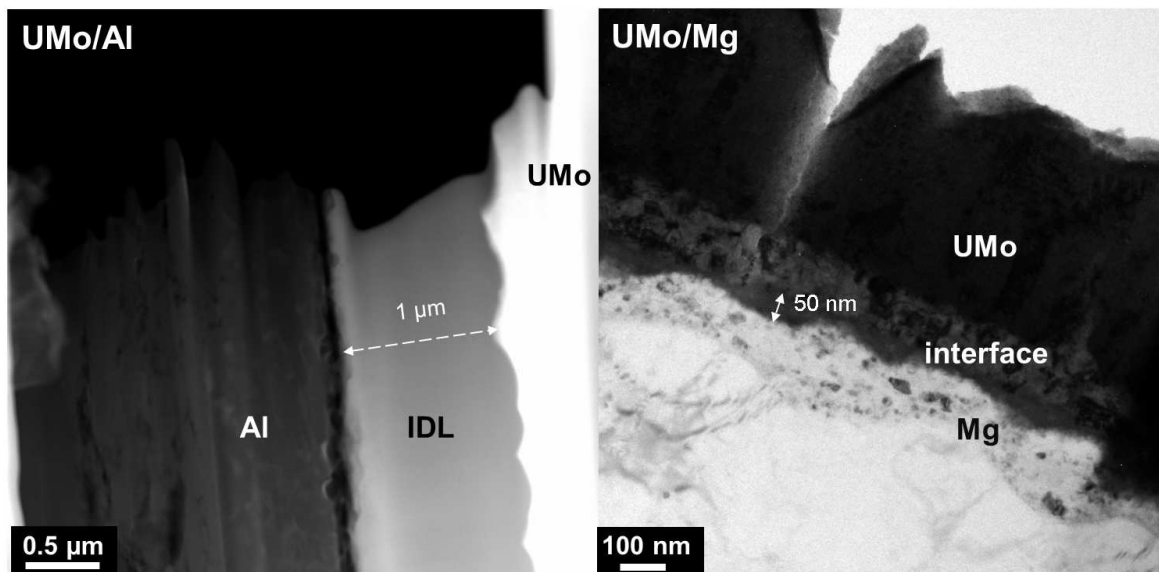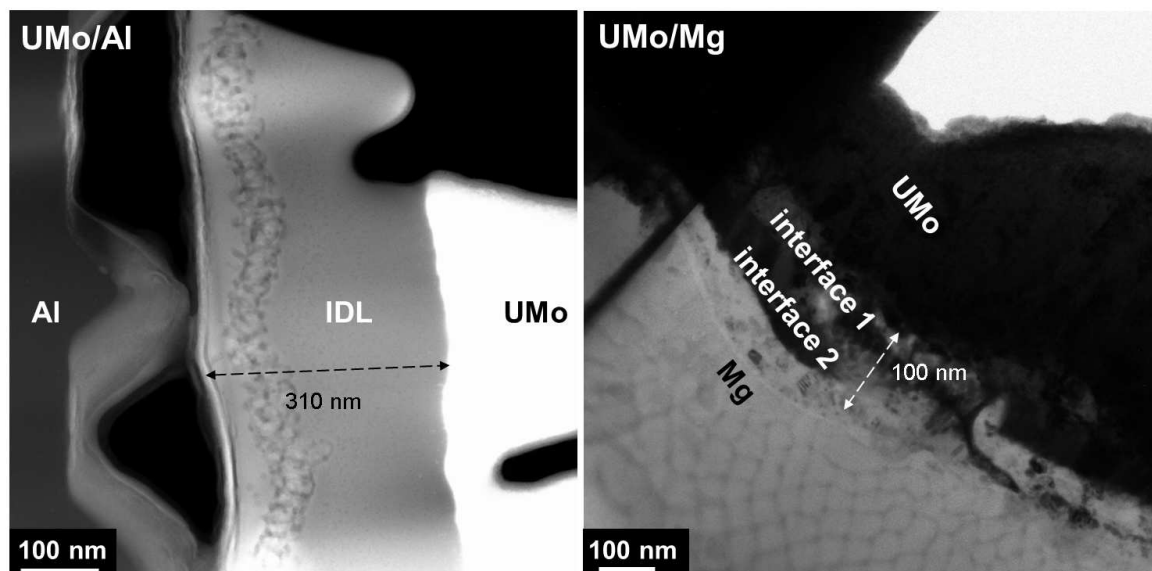
Figure 5.17: Under swift heavy ion irradiation at 140°C, the bright field image of the UMo/Al bilayer indicates the amorphous layer (i.e. IDL) is 1 μm in thickness while in the case of the UMo/Mg, the amorphous region is about 50 nm in thickness.

Figure 5.18: Under swift heavy ion irradiation at 200°C, the bright field image of the UMo/Al bilayer indicates the amorphous layer (i.e. IDL) is 310 nm in thickness while in the case of the UMo/Mg, the amorphous region is about 100 nm in thickness.

Chapter 6

Application of A Diffusion Barrier: Ti, Zr, Nb, and Mo

6.1   Introduction

Modifications on UMo/Al fuels have been proposed to suppress the undesired U-Mo-Al interactions and one of the propositions is to apply a diffusion barrier into UMo/Al fuels. The ideal barrier material should satisfy the following conditions:

1. atomic transport between UMo and Al across the barrier should be detained or even blocked;

2. the barrier should be thermodynamically stable against UMo and Al. If any intermetallics are formed, they should be stable under irradiation;

3. the barrier should have a high thermal conductivity and a high mechanical resistance;

4. the neutron absorption cross section of the barrier should be within an acceptable value to minimize the loss of neutron flux;

5. the barrier material should be compatible with processing procedures for spent fuel.

In order to meet the criteria, transition metals X such as Ti [25], Zr, Nb [123, 124] and Mo[125] have been suggested as barrier materials. In the present work swift heavy ion irradiation has been applied to study the stability of the UMo/X/Al trilayer. The trilayer was irradiated with ^{127}I ions at 80 MeV to simulate irradiation damage caused by fission fragments during in-reactor operation. The applied ion species and energy are the typical conditions of fission fragments. During irradiation, interactions at both the UMo/X and the X/Al interfaces are expected. However, the system of ion irradiation is in a non-equilibrium status, which makes it difficult to predict the irradiation-induced phases. To characterize atomic mixing and phases induced by swift heavy ion irradiation in this complex system, RBS and μ-XRD have been applied. The findings support the discussion of the modified properties (strength, ductility, etc.) and the evaluation of the UMo/X/Al trilayer for advanced UMo/Al fuels.

6.2   TRIM simulations: ion-solid interactions

Monte Carlo calculations using the TRIM code stopping range of ions in matter (SRIM 2008 [86]) predict the mean penetration depths of ^{127}I (at 80 MeV reaching a fluence of 10^{17} $ions/cm^2$) and its stopping power along the ion trajectory (Figure 6.1). TRIM calculations indicate that the ^{127}I ions penetrate both interfaces of the trilayer, i.e. the UMo/X and the X/Al interface, and are stopped in the Al. Most of the energy loss in the UMo/X/Al trilayer happened by electronic stopping power as shown in Figure 6.1B.
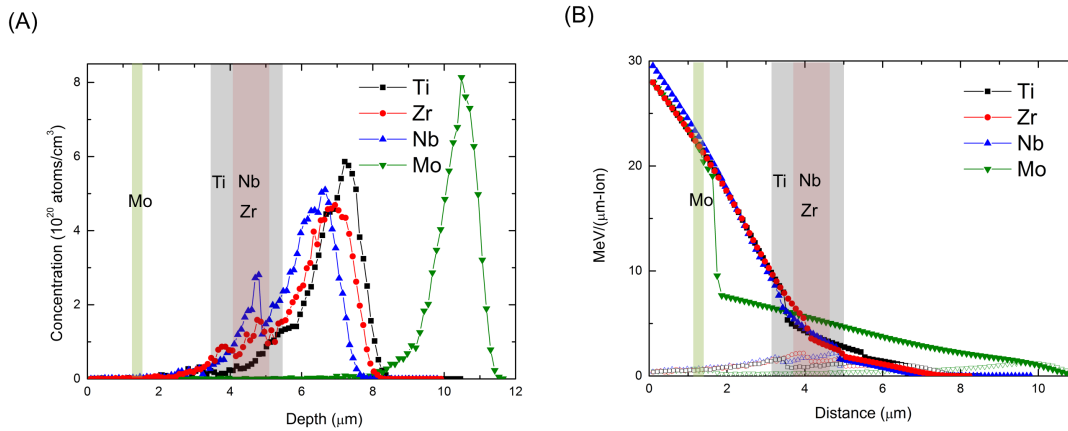
Figure 6.1: Graphic comparisons of the penetration depth of ^{127}I (A) and the depth profiles (B) of stopping powers among the UMo/X/Al trilayers based on SRIM calculations. The diffusion barrier layers have been marked by different colors. The range of ^{127}I indicates that the ions pass both the UMo/X and the X/Al interface. In the depth profiles of stopping powers, electronic stopping power (solid lines) is dominating over nuclear stopping power (hollow lines) over most of the ion range. Nuclear stopping power becomes dominant only at the end of the ion range.

6.3   Sampling

The UMo/X/Al trilayers (X= Ti, Zr, Nb, and Mo) involved in this investigation are composed of a UMo layer and a transition metal layer upon an Al substrate, preparing by DC-magnetron sputtering. The details of the UMo/X/Al trilayer are listed in Table 6.1. Afterwards, the UMo/Al bilayer were irradiated by ^{127}I ions at 80 MeV, reaching a final fluence of 10^{17} $ions/cm^2$ at a temperature of 200 ± 2°C, respectively. For μ-XRD measurements, thin films of the UMo/Al trilayers were prepared by FIB milling until the final thickness of 2 μm.

thickness (μm)	UMo/Ti/Al	UMo/Zr/Al	UMo/Nb/Al	UMo/Mo/Al
h_{UMo}	3.5	4	4	1.3
h_X	2	1	1	0.3

Table 6.1: Thicknesses of U/X/Mo layers for the samples investigated in this study

6.4 Irradiation-induced modifications: an overview by SEM

Cross-sections of the irradiated UMo/X/Al trilayer have been characterized via SEM probing by secondary electrons (SE) in in-lens mode. Unlike using backscattered electrons (BSE), the fraction of secondary electrons produced $\delta = N_{SE}/N_{beam}$ is relatively independent of the atomic number Z of the scattering atoms. However, the difference in the atomic number Z can still be discriminated, e.g. $\delta_{carbon} \simeq 0.5$ and $\delta_{gold} \simeq 2.0$. Besides, secondary electrons have the smallest sampling volume which enables a better spatial resolution than using backscattered electrons. Even though the intensity of the SE signal is sensitive to the atomic number Z yet the Z-contrast of SEM is too low to discriminated the intermetallics formed in UMo/X/Al during swift heavy ion irradiation as shown in Figure 6.2A, -C, and -D. As an exception, a homogeneous layer with a thickness of 350 nm has been detected beneath the Zr layer (Figure 6.2B) in the UMo/Zr/Al trilayer, which has been identified as Al_3Zr by μ-XRD (see Sec. 6.6.3).

6.5 Chemical analysis: elemental depth profiles

Chemical analysis for the UMo/X/Al trilayer (X= Ti, Zr, Nb, and Mo) applies both RBS and μ-XRF. RBS offers macroscopic information with the beam size of 0.5×0.5 mm^2 quantitatively while μ-XRF gives the microscopic insight qualitatively with the characterized size of 0.4×0.35 μm^2.

RBS spectra of the UMo/X/Al trilayer have been acquired at both the non-irradiated and ^{127}I irradiated areas. Atomic mixing induced by swift heavy ion irradiation can be recognized by the smearing of RBS spectra at the high energy edge near the interfaces, or by the flat-top peak broadening of the diffusion barrier at lower energies (Figure 6.3). The atomic mixing at interfaces has been quantitatively calculated using elemental depth profiles, i.e. atomic concentration of elements (%) versus areal density ($atoms/cm^2$), processed by the SIMNRA software [74]. Depth profiles of elements are shown in Figure 6.4. The atomic transport during swift heavy ion irradiation has been evidenced by comparing elemental depth profiles of the non-irradiated and the irradiated areas. The atomic mixing takes place especially at the X/Al interfaces, and this points out that the transition metals interacted strongly with Al. All samples have been oxidized at the surface due to oxygen uptake during irradiation. The intermixed region Δh induced by swift heavy ion irradiation can be calculated as

$$\Delta h = h^{irradiated} - h^{non-irradiated} = \left(\frac{D}{\rho_{mix}}\right)^{irradiated} - \left(\frac{D}{\rho_{mix}}\right)^{non-irradiated} \tag{6.1}$$
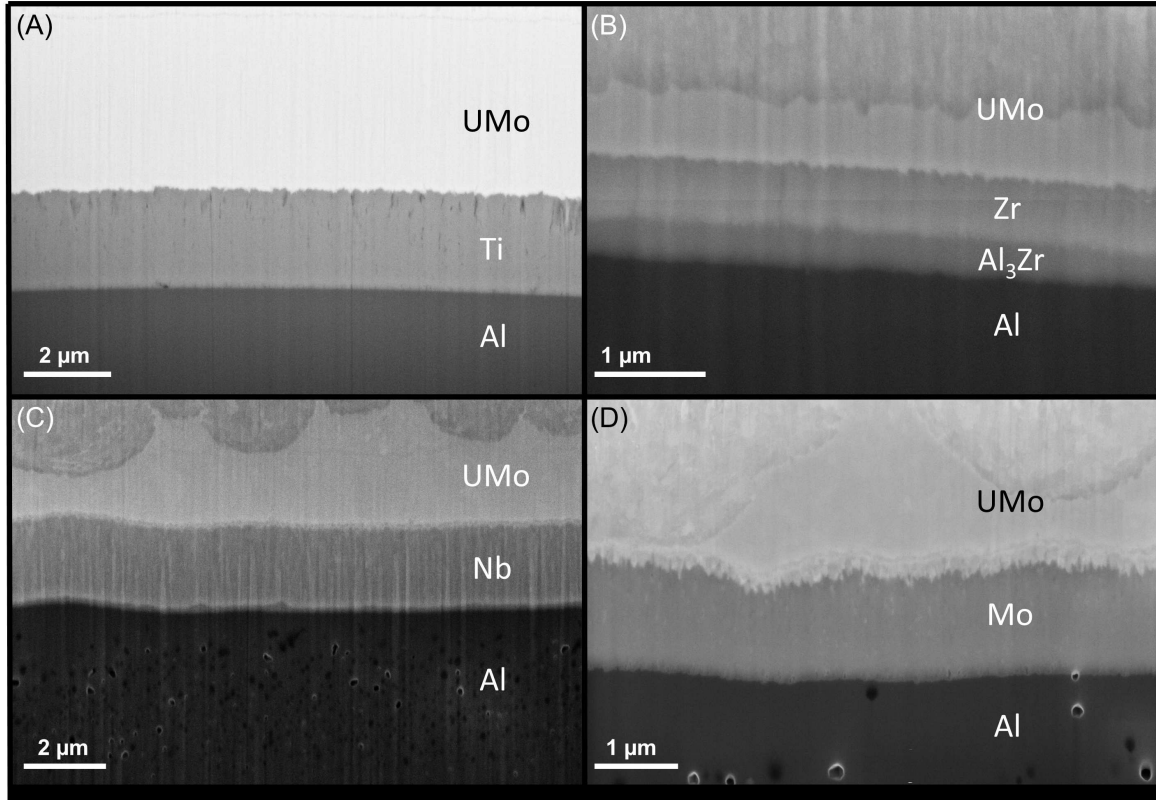
Figure 6.2: Cross-sections of (A) the UMo/Ti/Al, (B) the UMo/Zr/Al, (C) the UMo/Nb/Al, and (D) the UMo/Mo/Al trilayers prepared by FIB milling have been characterized by SEM using secondary electron (SE) in in-lens mode. Most of intermetallics induced by swift heavy ion irradiation are not detectable due to the limited Z-contrast. The intermetallic compound Al_3Zr in the UMo/Zr/Al trilayer is discriminable and is in form of a homogeneous layer (~ 350 nm) beneath the Zr layer as shown in (B).

where h (cm) is the interface region, D ($atoms/cm^2$) is the areal density provided by SIMNRA and ρ_{mix} is the local atomic density ($atoms/cm^3$). ρ_{mix} can be expressed as

$$\frac{1}{\rho_{mix}} = \sum_i \frac{C_i}{\rho_i} \tag{6.2}$$

where C_i and ρ_i is the concentration and the bulk atomic density of element i [126], respectively. The basic premises are

1. the elemental layers have elemental bulk densities;

2. the volume per atom ($1/\rho$) in the intermixed region is the same as in the pure element so that the local atomic density ρ_{mix} can be expressed in terms of bulk atomic density ρ_i.

The calculations of the intermixed region show that Ti interacts strongly with UMo in comparison to Zr and Nb. On the other hand, the intermixed region of Zr with Al is much larger than of Ti and of Nb. Among them, Nb is relatively inert to both UMo

and Al. The intermixed region in the UMo/Mo/Al trilayer cannot be estimated since the depth profile of U almost overlaps with that of Al in the Mo layer. The intermixed regions estimated for the UMo/X/Al trilayer (X = Ti, Zr, and Nb) are given in Table 6.2. In addition to the intermixed region, steps found in the RBS spectra after irradiation suggest the existences of irradiation-induced phases. A step near the UMo/Ti interface, i.e. at the channel number ~ 390, has been found in the UMo/Ti/Al trilayer. Also a step has been found near the Mo/Al interface (at the channel number ~ 380), in the UMo/Mo/Al trilayer. These steps can be assigned to constant compositions. The irradiation-induced steps in RBS spectrum are consequently characterized by μ-XRD.

$\Delta h_{UMo/X}$ (nm)	X	$\Delta h_{X/Al}$ (nm)
246	Ti	364
87	Zr	530
53	Nb	110

Table 6.2: The intermixed regions of the UMo/X/Al trilayer (X = Ti, Zr, and Nb) have been derived by using Eq. 6.1.
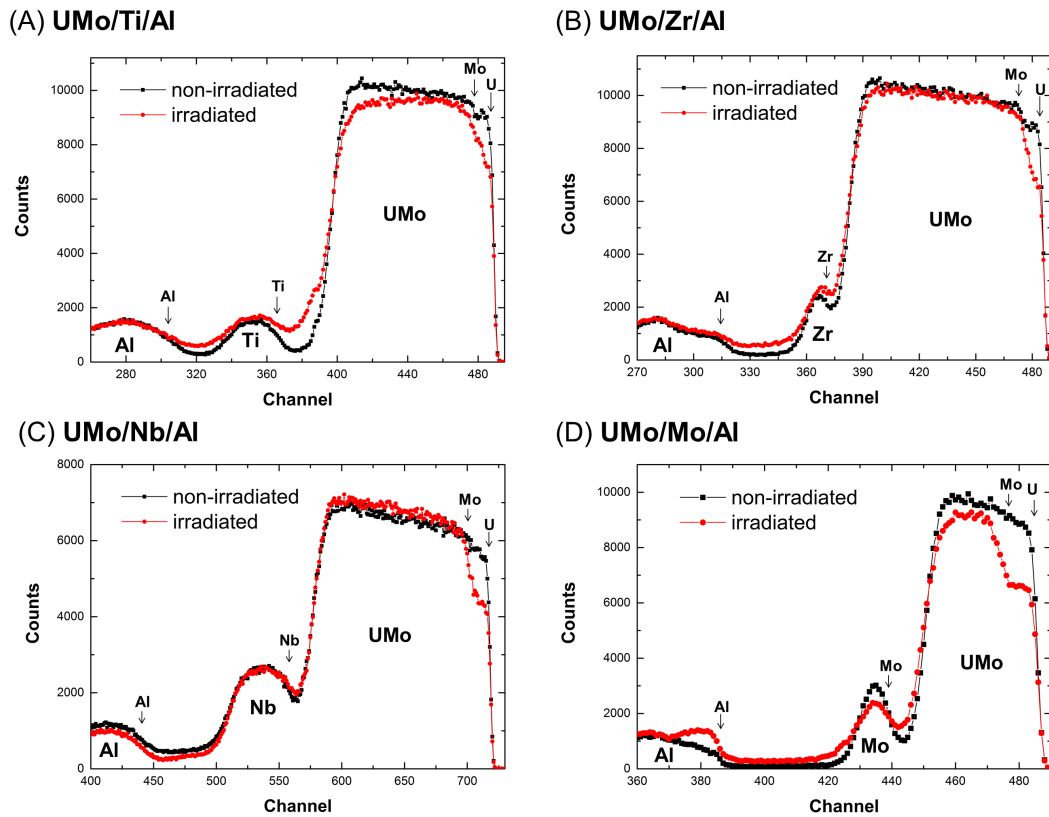
Figure 6.3: RBS spectra from both the non-irradiated and the irradiated areas of each UMo/X/Al trilayer (X = Ti (A), Zr (B), Nb (C), and Mo (D))
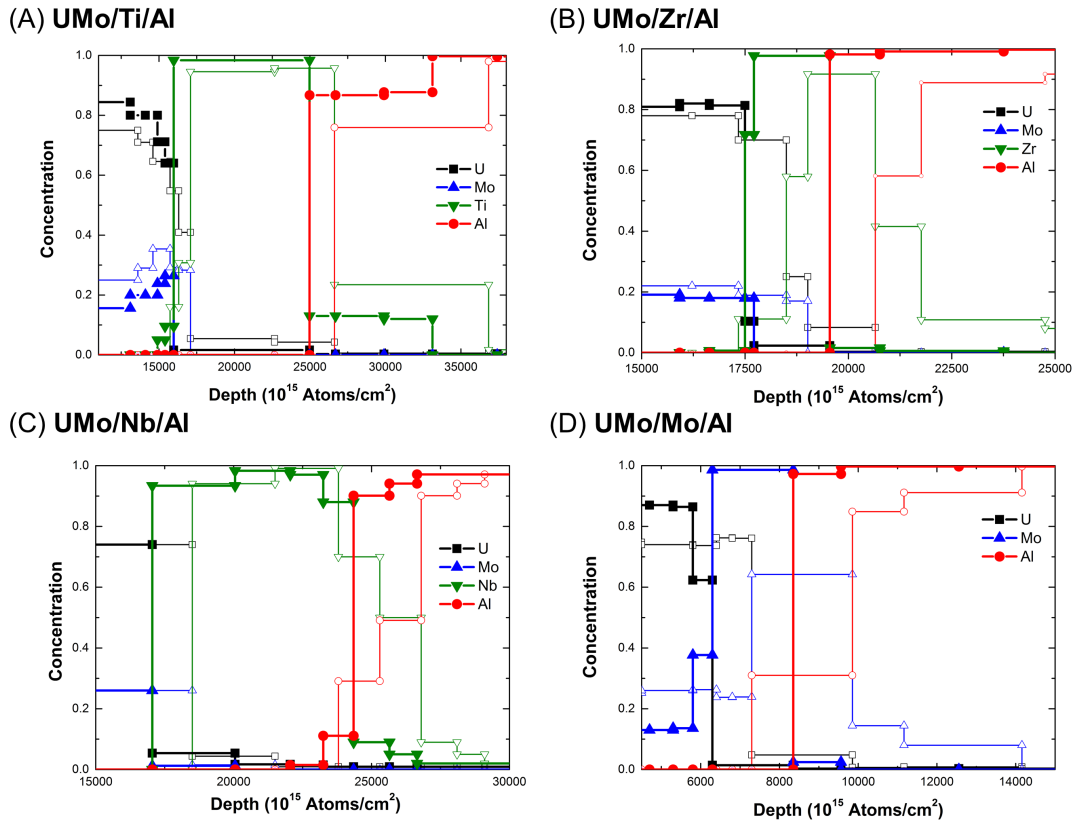
Figure 6.4: Elemental depth profiles at the respective non-irradiated area (solid lines) and irradiated area (dashed lines) of UMo/X/Al trilayer samples: X = Ti (A), Zr (B), Nb (C), and Mo (D). These depth profiles indicate the atomic mixing at interfaces after the irradiation process.

μ-XRF also gives the elemental depth profiles of the UMo/X/Al trilayer (X= Ti, Zr, Nb, and Mo). After the processing via the software PyMca [85], the qualitative elemental depth profiles can be obtained as shown in Figure 6.5. Due to the difference in the atomic scattering factors f, e.g. $f_U \sim 9 f_{Al}$, μ-XRF failed to detect Al signals. Since the elemental depth profiles provided by μ-XRF are given in intensities versus distance that the intermixing can be seen directly. The sizes of the intermixed region between U and Ti, Zr, Nb, and Mo are 4 μm, 1.15 μm, 1 μm, and 1.6 μm, respectively.

6.6   X-ray diffraction data analysis

6.6.1   Rietveld refinement

The 2D X-ray diffraction patterns have been corrected for dark field and converted into a 1D pattern using the software package Fit2D [81]. The phase identification has been processed by the software Match! [127] based on the data bank Inorganic Crystal Structure Database (ICSD) [128]. Accordingly Rietveld refinement analysis has been applied using the software package Fullprof [82]. Deformation and recrystallization texture by swift heavy ion irradiation have been taken into consideration in the Rietveld
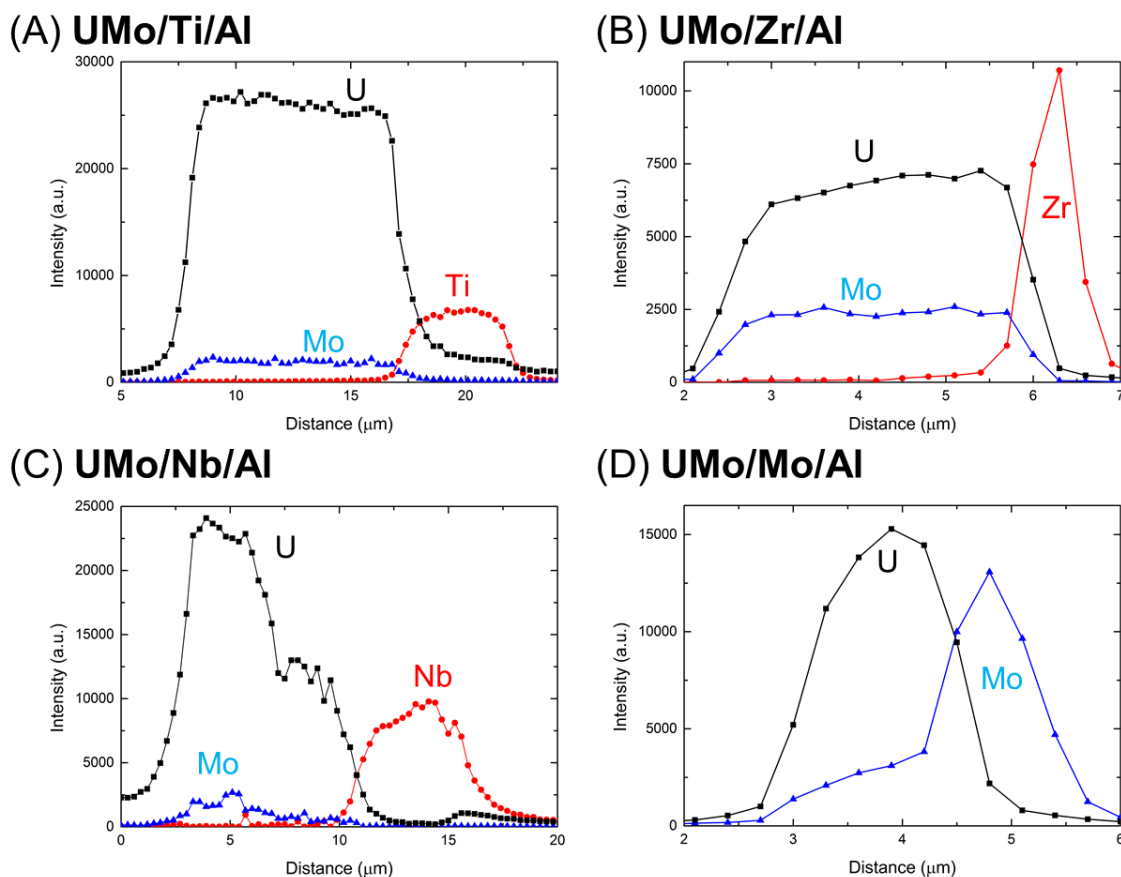
Figure 6.5: Elemental depth profiles measured by μ-XRF of UMo/X/Al trilayer samples: X = Ti (A), Zr (B), Nb (C), and Mo (D).

calculation: applying March-Dollase multiaxial preferred orientation after refining peak shapes (Pseudo-Voigt peak function).

6.6.2   UMo/Ti/Al trilayer

Figure 6.6 shows μ-XRD patterns of the UMo/Ti/Al trilayer from the UMo region (Figure 6.6A), the UMo/Ti interface (Figure 6.6B), and the Ti/Al interface (Figure 6.6C). At the UMo region, γ-UMo (space group symmetry: Im-3m), and UO_2 (Fm-3m) have been presented. The Cu pattern (Fm-3m) comes from the copper grid. UMo (Im-3m) and an intermetallic solid solution $Ti_{0.04}U_{0.96}$ (Cmcm) at the UMo/Ti interface have been identified. $Ti_{0.04}U_{0.96}$ results from a martensitic transformation of γ-U in the presence of a super-saturated Ti [129] once the irradiation terminated. The crystal structure of $Ti_{0.04}U_{0.96}$ is essentially the same as that of α-U with a slight difference in their lattice parameters. The orthorhombic α-U phase is undesired in UX fuel since it degenerates the corrosion resistance and the irradiation stability: α-U alloys cause anisotropic growth or deformation in dimension during the thermal cycling process [130]. Nevertheless, Ti additions up to 2% can effectively increase the strength, hardness and corrosion resistance of martensitic U (α-U) but decrease the ductility as well [131, 132, 133]. At the Ti/Al interface UMo (Im-3m) and the intermetallic solid solution $Al_{0.3}Ti_{1.7}$ ($P6_3/mmc$) are present. The crystal structure of $Al_{0.3}Ti_{1.7}$ is

isostructural to Ti and during irradiation this intermetallic solid solution will undergo an anisotropic deformation accompanying a lattice expansion. However, because of the partially filled d sub-shell of Ti the interatomic bonding strength of $Al_{0.3}Ti_{1.7}$ is expected to be higher than that of pure Al. In this case, $Al_{0.3}Ti_{1.7}$ could then protect the interface from further atomic mixing induced by ion irradiation. According to the Hume-Rothery rule [134], both $Ti_{0.04}U_{0.96}$ and $Al_{0.3}Ti_{1.7}$ belong to substitutional alloys. Upon the irradiation process solute Ti atoms of $Ti_{0.04}U_{0.96}$ and Al of $Al_{0.3}Ti_{1.7}$ have been transported to the respective solvents α-U and Ti by replacing the native atoms to form the solid solutions. Refined atomic parameters and concentrations of the phases found in the irradiated UMo/Ti/Al trilayer are listed in Table 6.3.

region	phase	concentration	space group	lattice parameter $\left(\overset{\circ}{A}\right)$
(A) UMo	γ-UMo	81%	Im-3m	3.4068 (3)
	UO_2	19%	Fm-3m	5.4327 (26)
(B) UMo/Ti interface	γ-UMo	82%	Im-3m	3.4065(1)
	$Ti_{0.04}U_{0.96}$	18%	Cmcm	a = 2.8482(15) b = 5.8307(19) c = 4.9519(27)
(C) Ti/Al interface	γ-UMo	75%	Im-3m	3.4094(9)
	$Al_{0.3}Ti_{1.7}$	25%	$P6_3/mmc$	a = 2.9686(3)
				c = 4.7852(9)

Table 6.3: Crystallographic information and concentrations of phases identified in the irradiated UMo/Ti/Al trilayer

6.6.3   UMo/Zr/Al trilayer

Figure 6.7 presents μ-XRD patterns of the UMo/Zr/Al trilayer. At the UMo region (Figure 6.7A), UMo (Im-3m) and UO_2 (Fm-3m) are detected. Near the UMo/Zr interface (Figure 6.7B), UMo (Im-3m) and Mo (Im-3m) have been identified detected. The Mo phase comes from Mo segregation out of UMo alloy. This segregation can be explained from the viewpoint of thermodynamics: the high positive enthalpy of mixing ΔH_m between Zr and Mo (36 kJ/mol) prevents Mo atoms inside UMo alloy from mixing with Zr and consequently the Mo phase forms. This Mo segregation causes a decrease of Mo concentration inside UMo alloy locally and this could decrease the γ-UMo stability [23, 135, 136]. However, there is no sign of γ-UMo decomposition into α-U, or any further destructive features at the UMo/Zr interface. A similar result has been reported that during the hot-rolling process of the UMo/Zr/Al monolithic fuel, Mo-rich precipitates occur. However, instead of in a form of Mo segregation, Mo_2Zr has been found [137]. At the Zr/Al interface, Zr ($P6_3/mmc$), UMo (Im-3m), and the irradiation-induced compound Al_3Zr (Pm-3m) are identified. The intermetallic compound Al_3Zr typically crystallizes in the tetragonal I4/mmm structure whereas the metastable cubic Al_3Zr (Pm-3m) can be produced by rapid solidification or grown

from a supersaturated solid solution [138, 139]. Cubic intermetallics are usually preferred phases due to their high ductility. In addition, Al_3Zr is densely packed with much stronger interatomic bonds compared to Zr. Such an intermetallic compound can prevent further atomic mixing of Zr and Al during the irradiation process. However, according to the broad Bragg's peaks, the crystallinity of Al3Zr in the UMo/Zr/Al might be poor, e.g. nanocrystalline, which will affect its mechanical properties. Details of phase information of the UMo/Zr/Al trilayer are summarized in Table 6.4.

region	phase	concentration	space group	lattice parameter $\left(\overset{\circ}{A}\right)$
(A) UMo	γ-UMo	92%	Im-3m	3.4080(1)
	UO_2	8%	Fm-3m	5.4497(11)
(B) UMo/Zr interface	γ-UMo	80%	Im-3m	3.4077(4)
	Mo	20%	Im-3m	3.1318(23)
(C) Zr/Al interface	γ-UMo	4%	Im-3m	3.4079 (4)
	Zr	38%	$P6_3/mmc$	a = 3.2594(4) c = 5.0278(135)
	Al_3Zr	58%	Pm-3m	4.1297(7)

Table 6.4: Crystallographic information and concentrations of phases identified within the irradiated UMo/Zr/Al trilayer sample

6.6.4 UMo/Nb/Al trilayer

Rietveld analysis with μ-XRD data of the three different regions UMo, UMo/Nb, and Nb/Al in the UMo/Nb/Al trilayer are graphically demonstrated in Figure 6.8. There are the expected phases: UMo (Im-3m) and UO_2 (Fm-3m) in the UMo region (Figure 6.8A); UMo (Im-3m) and Nb (Im-3m) at the UMo/Nb interface (Figure 6.8B). The Nb/Al interface (Figure 6.8C) displays UMo (Im-3m), Nb (Im-3m), $Mo_{0.1}Nb_{0.45}U_{0.45}$ (Im-3m), and Nb_3Al (Pm-3n) in a poor crystalline state. The ternary alloy $Mo_{0.1}Nb_{0.45}U_{0.45}$ formed usually by heat treatments, e.g. alloying [140], has better performance than the corresponding binary UX-alloys to improve the U-based fuel properties, such as irradiation resistance and corrosion resistance [141, 142]. Besides, a Nb addition of 1- 4% in the U-Mo-Nb system allows to retard transformations in γ-UMo alloys [143, 144]. Nb_3Al (Pm-3n) can be created at extremely high temperatures (T $\geq$ 2060°C) [145] or under He ion irradiation [146]. Nb_3Al has been used for high temperature applications because of its high stability and strength. Therefore, this phase can serve as a barrier against the Nb-Al interdiffusion. However, note the poor crystallinity of Nb3Al in the UMo/Nb/Al trilayer could degenerate its stability and strength. Refined structural parameters and concentrations of all phases found in the UMo/Nb/Al trilayer are given in Table 6.5.

region	phase	concentration	space group	lattice parameter $\left(\mathring{A}\right)$
(A) UMo	γ-UMo	99%	Im-3m	3.3965 (1)
	UO_2	1%	Fm-3m	5.4164 (274)
(B) UMo/Nb interface	γ-UMo	26%	Im-3m	3.4134 (1)
	Nb	74%	Im-3m	3.3244 (4)
(C) Nb/Al interface	γ-UMo	6%	Im-3m	3.4184 (1)
	Nb	82%	Im-3m	3.3191 (7)
	$Mo_{0.1}Nb_{0.45}U_{0.45}$	11%	Im-3m	5.1130(11)
	Nb_3Al	1%	Pm-3n	3.3264 (2)

Table 6.5: Crystallographic information and concentrations of phases identified within the irradiated UMo/Nb/Al trilayer sample

6.6.5   UMo/Mo/Al trilayer

μ-XRD patterns of the phases within the irradiated UMo/Mo/Al trilayer sample are shown in Figure 6.9. At the UMo region (Figure 6.9A) UMo (Im-3m) and UO_2 (Fm-3m) are present; UMo (Im-3m) and Mo (Im-3m) coexist near the UMo/Mo interface (Figure 6.9B); UMo (Im-3m), Mo (Im-3m) and an irradiation induced compound $Al_{12}Mo$ (Im-3) have been observed at the Mo/Al interface (Figure 6.9C). $Al_{12}Mo$ can be formed in thermal processes at 400°C $\leq$ T $\leq$ 661°C where the critical Mo content is lower than 10 at% [147]. This alloy shows a high-strength due to the covalent directional bonding [148, 149] which configures a densely packed layer. Hence, the presence of $Al_{12}Mo$ can be advantageous at the Mo/Al interface to prevent further degeneration of the interface due to ion collisions. Refined structural parameters and concentrations of all phases found in the UMo/Mo/Al trilayer are given in Table 6.6.

region	phase	concentration	space group	lattice parameter $\left(\mathring{A}\right)$
(A) UMo	γ-UMo	89%	Im-3m	3.4131(1)
	UO_2	11%	Fm-3m	5.4504(17)
(B) UMo/Mo interface	γ-UMo	94%	Im-3m	3.3998(2)
	Mo	6%	Im-3m	3.1398(1)
(C) Mo/Al interface	γ-UMo	44%	Im-3m	3.4035(5)
	Mo	33%	Im-3m	3.1504(16)
	$Al_{12}Mo$	23%	Im-3	7.6014(28)

Table 6.6: Crystallographic information and concentrations of phases identified within the irradiated UMo/Mo/Al trilayer sample

6.7 Discussion

6.7.1 Ion beam mixing: ballistic effects

Ion beam mixing due to ballistic effects has been simulated for the UMo/X/Al trilayer (X = Ti, Zr, Nb, and Mo) by means of TRIDYN code [87]. TRIDYN simulates dynamic changes of thickness and composition of multicomponent targets during high-dose ion irradiation and allows to calculate the depth profiles of different atomic species in the target as function of the incident fluence. For those trilayers with a thick UMo layer (i.e. X = Ti, Zr, and Nb), the elemental depth profiles of the diffusion barriers are almost unchanged after irradiation. TRIDYN calculations show that ballistic effects only contribute to an intermixed region of ~ 10 nm in these trilayers, which is is beyond the resolution of RBS and relatively small compared to the RBS observations. For the UMo/Mo/Al trilayer, with a relatively thin UMo layer, ion beam mixing by ballistic effects is more prominent - see Figure 6.10A. A comparison between the simulated and the initial Mo depth profiles points out that atomic mixing induced by ballistic effects is around 100 nm in the UMo/Mo/Al trilayer. In addition, a comparison of the UMo/Mo/Al trilayer between the TRIDYN calculations and the RBS spectrum is illustrated in Figure 6.10B. The deviation of Mo peak ($\sim$ channel number 600) of the TRIDYN calculations from the experimental result comes from the surface oxidation, which was not considered in TRIDYN calculations. The width of Mo peak remains after swift heavy ion irradiation, indicating atomic mixing is below depth resolution of RBS. Furthermore, the tail of the RBS spectrum extended to low energies suggests the existence of another diffusion phenomenon. The discrepancy of TRIDYN calculations and the RBS spectrum indicates that ion beam mixing by ballistic effects is relatively small and can be practically neglected for the investigated ion fluence.

6.7.2 Thermodynamic effects in ion mixing

When considering the UMo/Zr/Al and the UMo/Nb/Al trilayers, both of which should have the same ballistic response to ion mixing because their nearly identical parameters for ion-solid interactions: atomic density, atomic number, and atomic mass. The RBS data indicates that it is well-intermixed at interfaces in the UMo/Zr/Al trilayer, while it is relatively unchanged after irradiation in the UMo/Nb/Al trilayer. This disparity might result from the difference in ΔH_m of two trilayers. Miedema model [61, 62, 64, 65] has been applied for the ΔH_m calculations and the calculated chemical formation enthalpies of the U-X and the X-Al binary solid solutions are illustrated in Figure 6.11. The result in Figure 6.11A shows that Ti has a tendency to form a U-Ti alloy whereas other transition metals are relatively inert. Nb has a larger $+\Delta H_m$ against forming the U-Nb alloy in comparison to Zr. On the other hand, Figure 6.11B indicates that the applied transition metals are all in favor of forming X-Al solid solutions and Zr has a high tendency comparing to Ti, Nb and Mo. The tendency prediction by ΔH_m agrees well with the observation of RBS and μ-XRF. In combination of the result from TRIDYN and the good agreement of ΔH_m prediction, one can assume that chemical potentials dominate in the atomic mixing process during swift heavy ion irradiation. Nevertheless, further irradiation experiments will be necessary to clarify the exact mechanism.

6.7.3   RBS v.s. μ-XRD

The steps in the RBS spectra of the UMo/Ti/Al and the UMo/Zr/Al trilayers can be explained by the presence of $Ti_{0.04}U_{0.96}$ and $Al_{12}Mo$, respectively, based on their typical reflections in space-resolved μ-XRD pattern. A part of the intermetallic compounds identified in μ-XRD can be seen in the elemental depth profiles of RBS, as well. Nb_3Al in the UMo/Nb/Al trilayer has been observed in the elemental depth profile at the Nb/Al interface, giving the atomic ratio of Nb: Al = 7: 3 (see Figure 6.4C near the depth 25000×10^{15} $atoms/cm^2$). $Al_{12}Mo$ in the UMo/Mo/Al trilayer is in the ratio of Al: Mo = 9: 1 (see Figure 6.4D in the depth 13000×10^{15} $atoms/cm^2$). The deviated atomic ratio of RBS from the results in μ-XRD might come the limited resolution of RBS in probing the UMo/X/Al trilayer system: the UMo layer has high density (17.7 g/cm^3) and this layer is relatively thick compared to most RBS studies, i.e. of the order of 100 nm.

The combination of RBS and μ-XRD gives an overall understanding of the UMo/X/Al trilayer after irradiation. From the RBS measurements we have obtained the information about atomic mixing via elemental depth profiles, which is not trivial in μ-XRD mainly due to extremely different atomic scattering factors in the UMo/X/Al trilayer. On the other hands, qualitative and quantitative phase analysis can be performed with space-resolved μ-XRD data. In turns, several desired intermetallic compounds can be identified in UMo/X/Al systems.

6.8   Summary

The current study shows that the application of a diffusion barrier using transition metals in UMo/X/Al allows suppressing the UMo-Al interactions completely. Besides, atomic mixing at interfaces, such as UMo-X and X-Al intermixing, was limited maximal up to ~ 0.5 μm. Ti, Zr, Nb and Mo form intermetallics with Al, and these irradiation-induced compounds can act as additional interdiffusion barriers at the X/Al interface. However, Ti and Zr as the diffusion barriers might lead to γ-UMo decomposition by forming the orthorhombic U-Ti compound and segregating Mo from UMo, respectively. Nb as the diffusion barrier behaves stable at both the UMo/Nb and the Nb/Al interfaces while the poor crystallinity of the Nb-Al compound can be a concern. In conclusion Mo is the most promising candidate for diffusion barriers in UMo/X/Al systems with its high strength Mo-Al compound to protect the interface from further ion collisions.
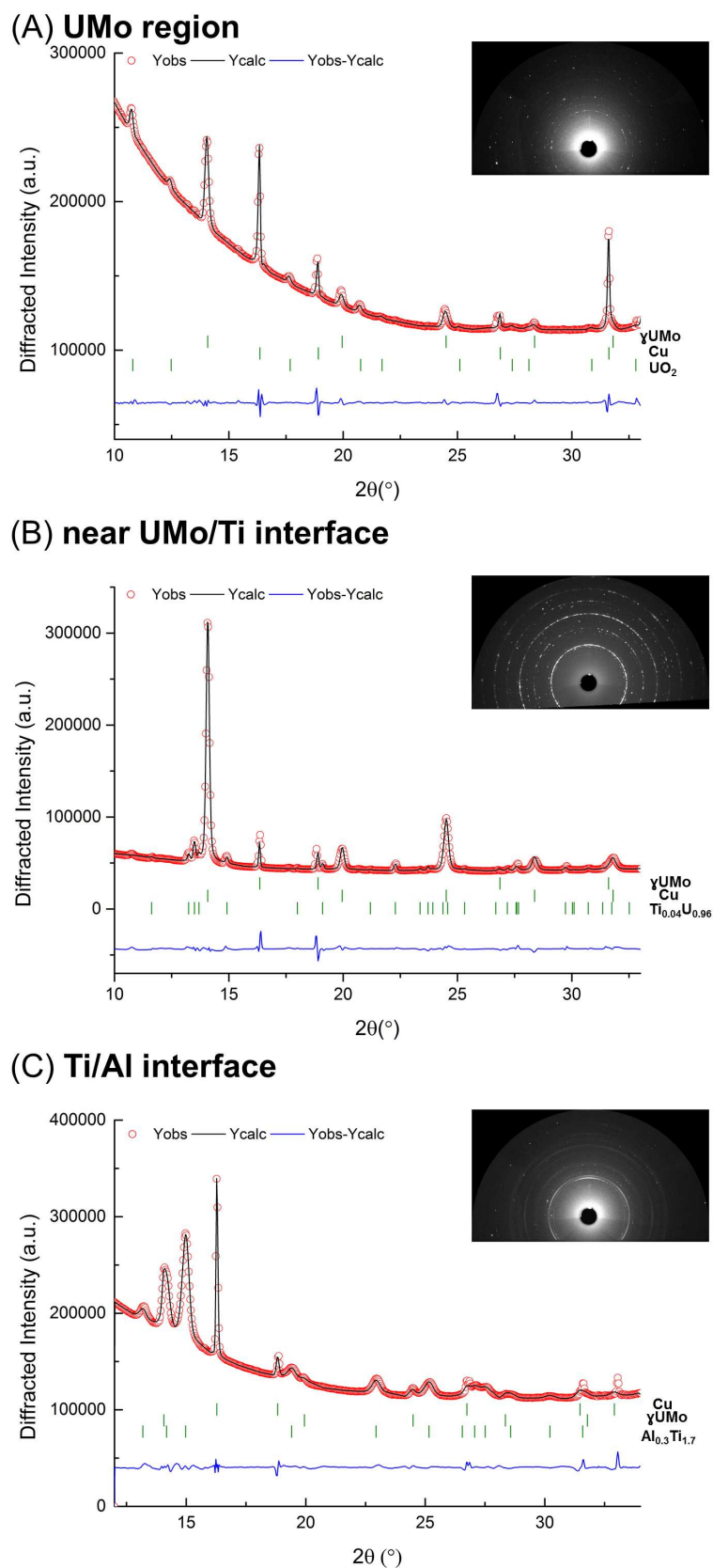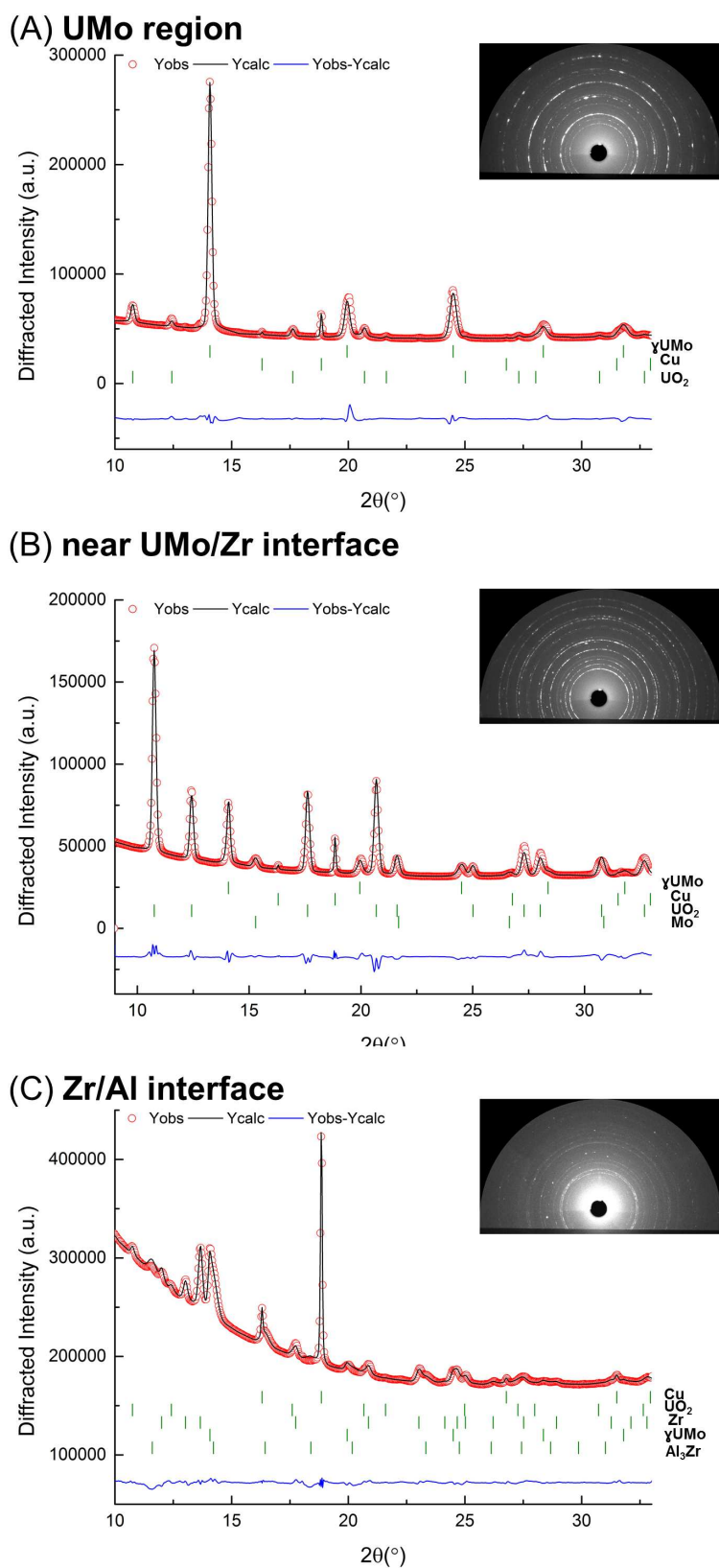
Figure 6.6: Spatially-resolved μ-XRD patterns of the UMo/Ti/Al trilayer: observed (open circles) and calculated (solid line) intensities meausred (A) in the UMo region; (B) at the UMo/Ti interface; and (C) at the Ti/Al interface of the UMo/Ti/Al sample. A flat difference profile at the bottom demonstrates a highly reliable agreement of observed intensities with those from Rietveld calculations with all identified phases given within each graphic. The bars indicate their reflection positions including those from the Cu sample holder.

(A) UMo region

(B) near UMo/Zr interface

(C) Zr/Al interface

Figure 6.7: Spatially-resolved μ-XRD patterns of the UMo/Zr/Al trilayer: observed (open circles) and calculated (solid line) μ-XRD patterns from different locations within the UMo/Zr/Al trilayer sample (A) at the UMo region; (B) in the UMo/Zr interfacial region; and (C) in the Zr/Al interfacial region.
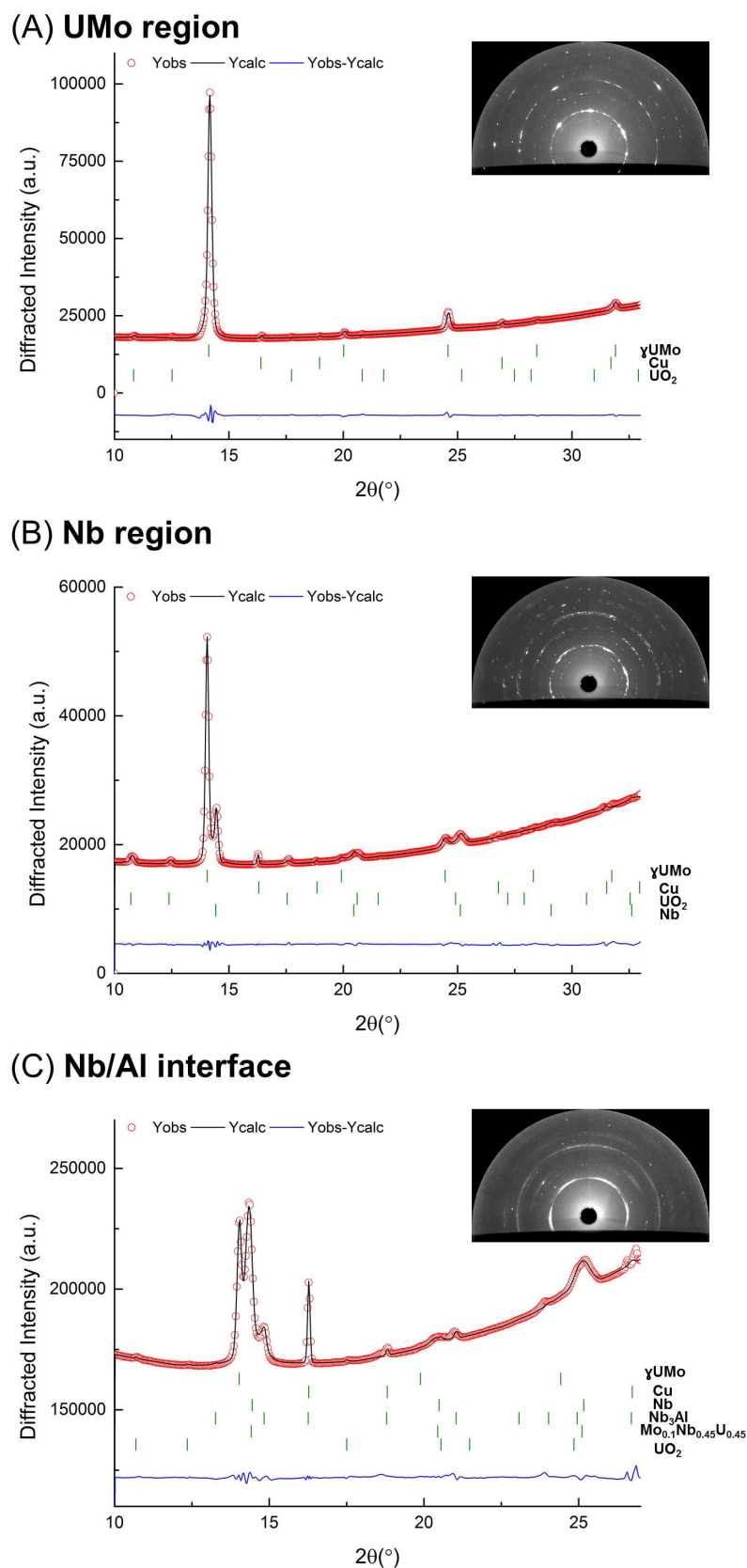
Figure 6.8: μ-XRD patterns of (A) the UMo region, (B) the UMo/Nb interfacial region, and (C) the Nb/Al interfacial region of the UMo/Nb/Al trilayer are presented. The flat discrepancy profiles given at the bottom demonstrate well-performed Rietveld calculations with all identified phases (bars) at the UMo layer (UMo, U-oxide), at the UMo/Nb interface (UMo, U-oxide and Nb), and at the Nb/Al interface (UMo, U-oxide, Nb, Nb_3Al and $Mo_{0.1}Nb_{0.45}U_{0.45}$) along with Cu.
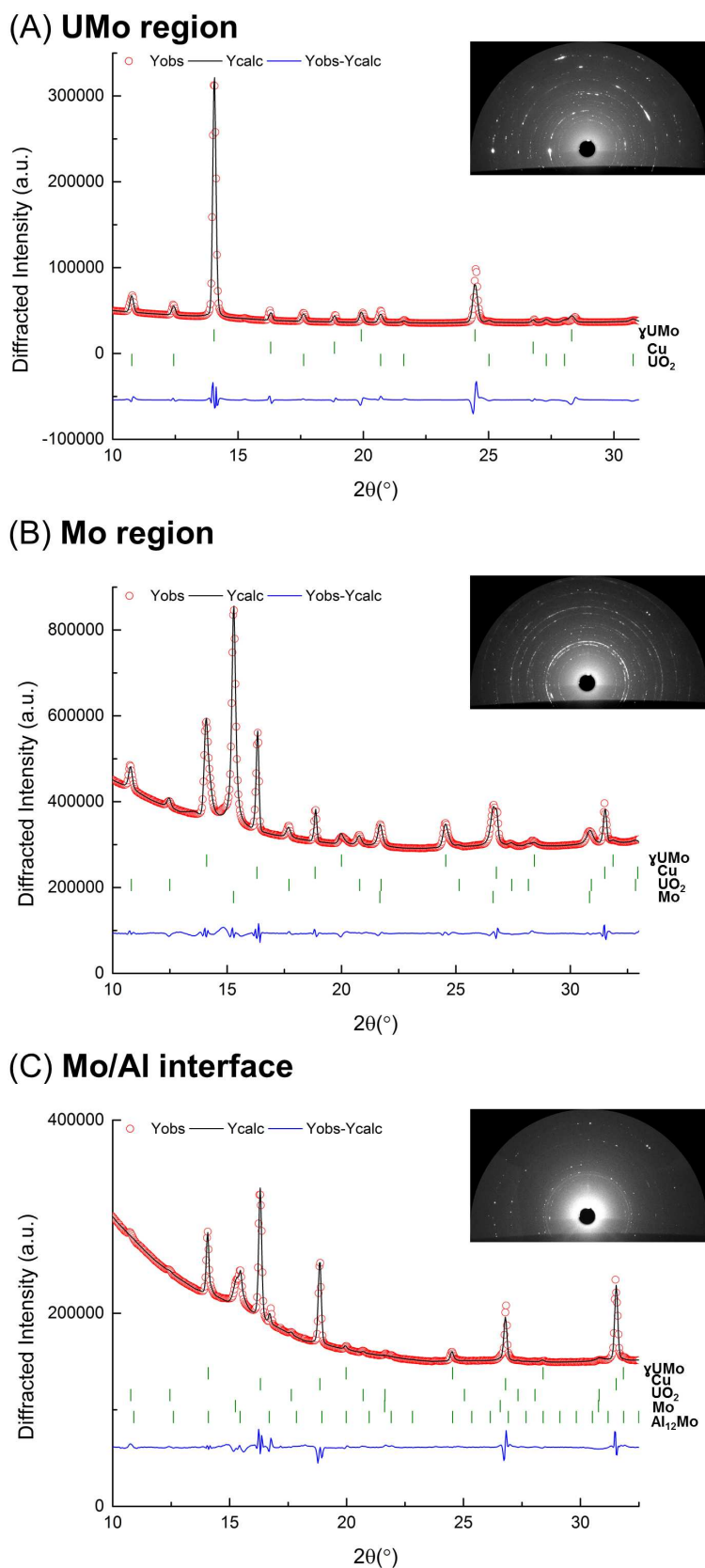
Figure 6.9: μ-XRD patterns of (A) the UMo region, (B) the UMo/Mo interfacial region, and (C) the Mo/Al interfacial region of the UMo/Mo/Al trilayer. The flat discrepancy profiles given at the bottom demonstrate well-performed Rietveld calculations with all identified phases (bars) at the UMo layer (UMo, U-oxide), at the UMo/Mo interface (UMo, U-oxide and Mo) and at the Mo/Al interface (UMo , U-oxide, Mo and $Al_{12}Mo$) along with Cu.
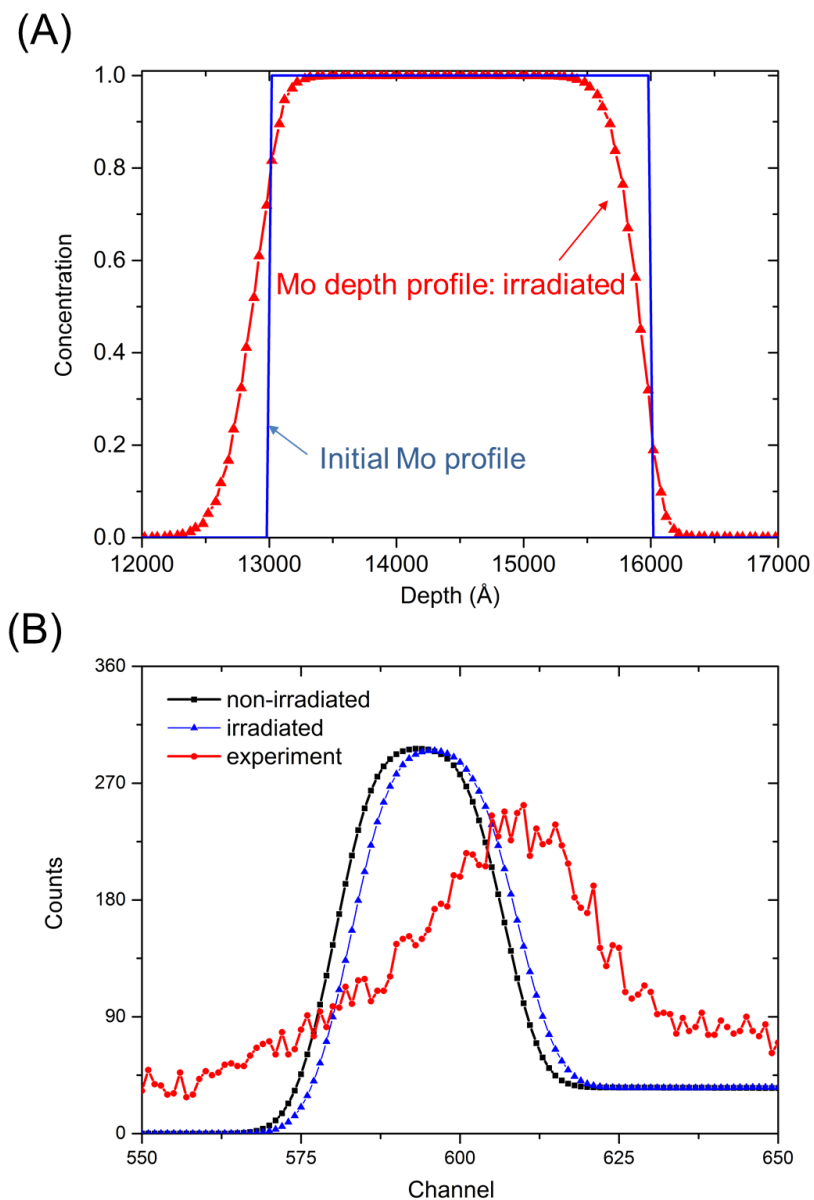
Figure 6.10: (A) Mo depth profile of the UMo/Mo/Al trilayer evaluated from simulated swift heavy ions irradiation-induced ballistic effects using TRIDYN; (B) A comparison of the TRIDYN simulation with the observed RBS spectrum of the UMo/Mo/Al trilayer.
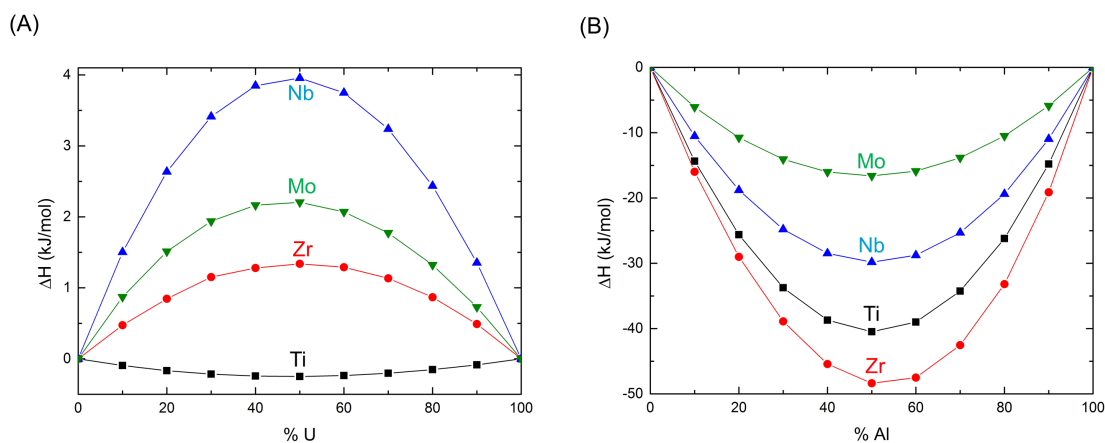
Figure 6.11: Enthalpies of chemical formation of the binary solid solutions (A) the U-X and (B) X-Al have been calculated based on Miedema model [61, 62, 64, 65]. (A) shows that Ti has a tendency to form a U-Ti alloy whereas other transition metals are relatively inert. Nb has a larger $+\Delta H_m$ against forming the U-Nb alloy in comparison to Zr. On the other hand, (B) indicates that the applied transition metals are all in favor of forming X-Al solid solutions and Zr has a high tendency comparing Ti, Nb, and Mo.

Chapter 7

Conclusion and Outlook

Swift heavy ion irradiation has been demonstrated to be an adequate technique to evaluate the stability of the UMo fuels efficiently. In the UMo/Al bilayer, swift heavy ion irradiation well reproduces the IDL which has the same structure, amorphous with a comparable nearest neighbor distance, as the one produced during in-pile irradiation. Besides, a band composed of voids has been found inside the IDL, which indicates that Kirkendall effect takes place in the UMo-Al diffusion process. Those voids are assumed to be the accommodation sites at the early stage of fission gas collisions.

Material selection of the UMo fuels using swift heavy ion irradiation shows that the interdiffusion reactions can be successfully detained by using Mg as the matrix material and by applying transition metals Ti, Zr, Nb, and Mo as the diffusion barrier. In the UMo/Mg bilayer, the amorphization at the interface suggests an interdiffusion layer occurs in a form of the U-Mo-Mg mixture. In the UMo/Mg bilayer irradiated at 200°C, the mixture has been identified as an immiscible U-Mg alloy $U_{0.9}Mg_{0.1}$. This result demonstrates that elements which are immiscible to one another can be alloyed by swift heavy ion irradiation. Furthermore, their immiscibility can lead to spinodal decomposition. The application of transition metals X (X = Ti, Zr, Nb, and Mo) as the diffusion barrier in the UMo/Al fuels exhibits a complete suppression of the UMo-Al interdiffusion. The atomic mixing at the UMo/X and the X/Al interfaces induced by swift heavy ion irradiation has been limited to 0.5 μm. In addition, irradiation-induced phases in the UMo/X/Al trilayer have been identified: $Ti_{0.04}U_{0.96}$ and $Al_{0.3}Ti_{1.7}$ in the UMo/Ti/Al trilayer, Al_3Zr in the UMo/Zr/Al trilayer, $Mo_{0.1}Nb_{0.45}Mo_{0.45}$ and Nb_3Al in the UMo/Nb/Al trilayer, and $Mo_{12}Al$ in the UMo/Mo/Al trilayer. These irradiation-induced phases usually form thermally at much higher temperatures (e.g. $Mo_{12}Al$ at 400°C and Nb_3Al at 2060°C) or by rapid solidification from a supersaturated alloy (e.g. $Ti_{0.04}U_{0.96}$ and Al_3Zr). The formation of the irradiation-induced phases implies a high local temperature or an enhancement of atomic diffusivities during swift heavy ion irradiation.

Studies on irradiation-induced diffusion are essential in order to figure out the exact diffusion mechanism dominating in a non-equilibrium state. This question can be answered by performing a series of swift heavy ion irradiation experiments by varying the energy, the fluence, and the temperature. Speaking of the applying energy, as discussed in Sec. 4.7.3, the different dominating stopping powers can give rise to different diffusion rates and material modifications. Therefore, swift heavy ion irradiation should

be performed at least two energy regimes, i.e. few MeV to 70 - 90 MeV, to precisely simulate in-pile irradiation where both electronic stopping power and nuclear stopping power contributing comparably. By varying the final fluence (e.g. $5 \times 10^{15} - 1 \times 10^{17}$ $ions/cm^2$), one can achieve a correlation between the fluence and the concentration profile. For the case of UMo/Al bilayer, the ion dose threshold of forming an IDL can be obtained. This ion dose threshold gives a hint about the mechanism of the phase formation under swift heavy ion irradiation. The UMo/Mg bilayer experiment in Chap. 5 shows that the irradiation temperature greatly influences diffusion reactions. To clarify the thermal contribution to irradiation-induced diffusion, swift heavy ion irradiation should be applied at low temperatures (e.g. room temperature or even 0°C) to minimize or eliminate the thermal effects. An important quantity, diffusion coefficient, is essential for the irradiation-induced diffusion study and can be obtained by varying these three parameters (i.e. energy, fluence, and temperature). Once this quantity is known, the radiation damages of the UMo fuels induced by fission fragments can be simulated so that a prediction of the life time of the fuel element can be made. However, one should keep in mind that the diffusion coefficient changes once the irradiation-induced phase forms, e.g. from Al into IDL in the case of the UMo/Al bilayer. Therefore, a complete study of diffusion coefficient should be achieved to complete the prediction of fuel life time, including the diffusion coefficient of UMo/Al at low doses and at high doses the diffusion coefficient of UMo/IDL and of IDL/Al.

Bibliography

[1] A. Röhrmoser et al., *Reduced enrichment program for the FRM II* in proceedings of the 26th Reduced Enrichment for Research and Test Reactors (RERTR), Vienna, 2004

[2] J.P. Durand et al, *LEU fuel development at CERCA: status as of October 1993* in proceedings of the 16th Reduced Enrichment for Research and Test Reactors (RERTR), Oarai, 1993

[3] C.W., Jocob, B.E. Warren, Journal of the American Chemical Society 59 (1937) 2588

[4] G.L. Hofman, L.C. Walters, *Metallic fast reactor fuels* in Material Science and Technology Volume 10A, Nuclear Materials, VCH Verlagsgesellschaft mbH, Weinheim, 1994

[5] W.H. Zachariasen, Acta Crystallographica 1 (1948) 265

[6] M.C. Udy, F.W. Boulger, Transactions of the American Institute of Mining, Metallurgical and Petroleum Engineers 200 (1954) 207

[7] E.K. Halteman, Acta Crystallographica 10 (1957) 166

[8] N.C. Baenziger, R.E. Rundle, A.I. Snow, A.S. Wilson, Acta Crystallographica 3 (1950), 34

[9] M.K. Meyer et al, Journal of Nuclear Materials 278 (2000) 358

[10] G.L. Hofman, Journal of Nuclear Materials 150 (1987) 238

[11] D.H. Gurinsky, G.J. Dienes, Nuclear Fuels, D. Van Nostrand, New York, 1956

[12] B. Frost, Material Science and Technology Volume 10A, Nuclear Materials, VCH Verlagsgesellschaft mbH, Weinheim, 1994

[13] M.K.Meyer et al., Journal of Nuclear Materials 304 (2002) 221

[14] M.P. Johnson, W.A. Holland, *Irradiation of U-Mo base alloys*, Technical Report NAA-SR-6262, Atomics International, 1964

[15] M.A. Leeser et al., *Radiation stability of fuel elements for the Enrico Fermi power reactor* in proceedings of the 2nd on the Peaceful Uses of Atomic Energy 5 (1958) 587

[16] R.M- Hengstler et al., Journal of Nuclear Materials, 402 (2010) 74

[17] A. Bonnin et al., Z. Kristallogr. Proc. 1 (2011) 29

[18] C.D. Cagle, L.B. Emlet, *Slug ruptures in the Oak Ridge National Laboratory pile*, Technical Report ORNL-170, Oak Ridge National Laboratory, 1948

[19] G.L. Hofman et al., *Post irradiation analysis of low enriched U-Mo/Al dispersion fuel miniplate tests RERTR 4&5* in proceedings of the 26th Reduced Enrichment for Research and Test Reactors (RERTR), Vienna, 2004

[20] P. Lemoine et al., *UMo dispersion fuel results and status of qualification programs* in proceedings of the 8th Research Reactor Fuel Management (RRFM), Munich, 2004

[21] S. van den Berghe et al., Journal of Nuclear Materials, 375 (2008) 340

[22] S.L. Hayes et al., *Modelling RERTR experimental fuel plates using the palte code* in proceedings of the 25th Reduced Enrichment for Research and Test Reactors (RERTR), Chicago, 2002

[23] J.M. Park et al., *Phase stability and di.usion characteristics of U-Mo-X (X=Si, Al, Zr or Ti) alloys* in proceedings of the 27th Reduced Enrichment for Research and Test Reactors (RERTR), Boston, 2005

[24] A. Leenaers, *EPMA results obtained on the IRIS-TUM fuel* in proceedings of the 30th Reduced Enrichment for Research and Test Reactors (RERTR), Washington, 2008

[25] W.C. Thurber, R.J. Beaver, *Development of Silicon modified 48wt%U-Al alloys for aluminum plate type fuel elements*, Technical Report ORNL-2602, Oak Ridge National Laboratory, 1959

[26] M. Rodier et al., *Effects of Ti in the UMo/Al system: preliminary results* in proceedings of the 11th Research Reactor Fuel Management (RRFM), Lyons, 2007

[27] R.O. Williams, *Terminal report on ORNL slug problem - causes and prevention*, Technical Report CF-50-7-160, Oak Ridge National Laboratory, 1950

[28] L.S. DeLuca et al., *Rate of growth of di.usion layers in U-Al and U-AlSi couples*, Technical Report KAPL-1747, Knolls Atomic Power Laboratory, 1957

[29] A. Izhutov et al., *The status of LEU U-Mo fuel investigation in the MIR reactor* in proceedings of the 31th Reduced Enrichment for Research and Test Reactors (RERTR), Bejing, 2009

[30] R. Jungwirth et al., Journal of Nuclear Materials, 434 (2013) 296

[31] D.D. Keiser et al., *Microstructural analysis of irradiated U-Mo fuel plate: recent results* in proceedings of the 16th IResearch Reactor Fuel Management (RRFM), Prague, 2012

[32] H-Y. Chiang et al., Journal of Nuclear Materials, 440 (2013) 117

[33] C.K. Gupta, Materials in Nuclear Energy Applications Volume 1, CRC Press Inc. 1989

[34] D. Smidt, Reaktortechnik I/II G. Braun-Verlag, Karlsruhe, 1976

[35] Hyperphysics, http://hyperphysics.phy-astr.gsu.edu/hbase/nucene/fisfrag.html

[36] D. Emendörfer, K.H. Höcker, Theorie der Kernreaktoren, Wissenschaftsverlag, Berlin, 1982

[37] M. Nastasi, J.W. Mayer, J.K. Hirvonen, Ion-Solid Interactions: Fundamentals and Applications, Cambridge Press, 1996

[38] F. Seitz, J.S. Koehler, *Displacement of Atoms During Irradiation* in *Solid State Physics* editted by F. Seitz and D. Turnbull, Volume 2, Academic Press, New York, 1956

[39] P. Sigmund, Applied Physics Letter, 25 (1974) 169

[40] J.A. Brinkman, Journal of Applied Physics, 25 (1954) 961

[41] J.A. Brinkman, American Journal of Physics, 24 (1956) 246

[42] J.W. Mayer, S.S. Lau, *Ion Beam Mixing* in Surface Modification and Alloying by Laser, Ion, and Electron Beams editted by J.M. Poate, G. Foti, D.C. Jacobson, Plenum Press, New York, 1983

[43] S. Matteson et al., Nuclear Instruments and Methods in Physics Research B, 182 (1981) 43

[44] P.G. Shewmon, Diffusion in Solids, McGraw-Hill, New York, 1963

[45] Y.T. Cheng, M. van Rossum, M.-A. Nicolet, W.L. Johnson, Applied Physics Letters, 45 (1984) 185

[46] Y. Adda, M. Beyeler, G. Brebec, Thin Solid Films, 25 (1975) 107

[47] K.C. Russel, Progress in Material Science, 28 (1984) 229

[48] R. Sizmann, Journal of Nuclear Materials, 69 (1978) 386

[49] H. Mehrer, Diffusion in Solids, Springer Series in Solid-State Sciences, Vol. 155, 2007

[50] H. Hsieh et al., Physical Reviews, B40 (1989) 9986

[51] L.E. Rehn, P.R. Okamoto, Journal of Nuclear Instruments and Methods, B39 (1989) 104

[52] M. Nastasi, J.W. Mayer, Radiation Effects & Defects in Solids, 120-1 (1994) 367

[53] M. Nastasi, J.W. Mayer, J. Hirvonen, Ion-Solid Interactions: Fundamentals and Applications, Cambridge University Press, Cambridge, 1996

[54] J.L. Brimhall, H.E. Kissinger, L.A. Charlot, Radiation Effects, 77 (1983) 237

[55] B.X. Liu, W.L. Johnson, M.A. Nicolet, S.S. Lau, Applied Physics Letter, 42 (1983) 45

[56] H.M. Naguib, R. Kelly, Radiation Effects, 25, 1 (1975)

[57] M. Hillert, Acta Materialia, 9 (1961) 525

[58] R.A.L. Jones, Soft Condensed Matter, Oxford University Press, 2004

[59] S. Van den Berghe, A. Leenaers, C. Detavernier, *The SELENIUM Fuel Experiment – Progress Report After 2 Cycles* in proceedings of the 34th Reduced Enrichment for Research and Test Reactors (RERTR), Warsaw, 2012

[60] MCNP Library, www.atom.kaeri.re.kr

[61] A.R. Meidema, A.K. Niessen, F.R. Boer, R. Boom, W.C.M Mattens, Cohesion in Metal: Transition Metal Alloys (1989) Amsterdam: North-Holland

[62] H. Bakker, Enthalpies in Alloys: Miedema's Semi-Empirical Model, Trans Tech Publications, Zurich, 1998

[63] L. Pauling, The Nature of the Chemical Bond, Cornell University Press, Ithaca, 1952

[64] R. F. Zhang, B.X. Liu, Applied Physics Letters, 81 (2002) 1219

[65] R. F. Zhang, B.X. Liu, Applied Physics Letters, 86 (2002) 216104

[66] W. Schmid, *Construction of a sputtering reactor for the coating and processing of monolithic U–Mo nuclear fuel*, Ph. D thesis, Technische Universität München, 2011

[67] Homepage of Maier-Leibnitz-Laboratorium, www.bl. physik.tu-muenchen.de

[68] R. Jungwirth, Irradiation behaviour of modified high performance nuclear fuels, Ph. D thesis, Technische Universität München, 2011

[69] A. Röhrmoser, W. Petry, *Fuel plate temperature during operation of FRM II* in proceedings of the 13th Research Reactor Fuel Management (RRFM), Vienna, 2009

[70] K.N. Choo et al., *Contribution of HANARO irradiation facilities to national nuclear R&D* in proceedings of International Symposium on Material Testing Reactor (ISMTR), Columbia, USA, 2012

[71] J.B. Pawley, Handbook of Biological Confocal Microscopy, Springer, Berlin, 2006

[72] Gwyddion homepage, www.gwyddion.net

[73] Y. Wang, M. Nastasi, Handbook of Modern Ion Beam Materials Analysis, Materials Research Society, Warrendale, 2009

[74] M. Mayer, SIMNRA home page, www.simnra.com

[75] M. Mayer, Nuclear Instruments and Methods in Physics Research B, 266 (2008) 1852

[76] C. Waltenberg, Carl Zeiss Microscopy GmbH, private communications

[77] FindIt, www.fiz-karlsruhe.de/icsd_home

[78] G. Martínez-Criado et al., Synchrotron Radiations, 19 (2012) 10

[79] J.-C. Labiche, O. Mathon, S. Pascarelli, M. A. Newton, G. Guilera Ferre, C. Curfs, G. Vaughan, A. Homs, C. Fernandez, Rev. Sci. Instrum. D 78 (2007) 09130

[80] C.G. Shroer et al., Nuclear Instruments and Methods in Physics Research A, 616 (2010) 93

[81] H. Hammersley,FIT2D homepage, www.esrf.eu/computing/scientific/FIT2D

[82] J. Rodriguez-Carvajal, Fullprof homepage, www.ill.eu/sites/fullprof

[83] H.S. Peiser, H.P. Rooksby, A.J.C. Wilson, X-ray Diffraction by Polycrystalline Materials, The Institute of Physics, London, 1955

[84] P.J. Goodhew, J. Humphreys, R. Beanland, Electron Microscopy and Analysis, Taylor & Francis, London, 2001

[85] PyMca homepage, www.pymca.sourceforge.net

[86] J.F. Ziegler, SRIM homepage, www.srim.org

[87] W. Möller, W. Eckstein, Nuclear Instruments and Methods in Physics Research B, 2 (1984) 814

[88] M. Mirandou et al., Journal of Nuclear Materials, 323 (2003) 29

[89] H. Palancher et al., Journal of Applied Crystallography, 40 (2007) 1064

[90] N. Wieschalla et al., Journal of Nuclear Materials, 357 (2006) 191

[91] H. Palancher et al., Journal of Nuclear Materials, 385 (2009) 449

[92] T. Zweifel, et al., *Heavy ion irradiation on UMo/Al systems : Temperature influence* in proceedings of the 14th Research Reactor Fuel Management (RRFM), Rome, 2011

[93] D. Olander, Journal of Nuclear Materials, 372 (2008) 94

[94] P. Scherrer, Göttinger Nachrichten Gesell., Volumne 2, 1918

[95] A. Patterson, Physical Reviews 56 (1939) 978

[96] A. Monshi et al., World Journal of Nano Science and Engineering, 2 (2012) 154

[97] Digitalmicrograph, www.gatan.com

[98] D.R.G. Mitchell, Microscopy Research and Technique, 71 (2008) 588

[99] Fityk Howepage, www.fityk.nieto.pl

[100] W.V. Vaidya, K. Ehrlich, Journal of Nuclear Materials, 113 (1983) 149

[101] A.E. Dwight, Journal of Nuclear Materials, 2 (1960) 81

[102] R.A. Andrievskii, The Physics of Metals and Metallography, 110 (2010) 229

[103] H. M. Rietveld, Journal of Applied Crystallography, 2 (1969) 65

[104] B.S. Seong et al., Journal of Nuclear Materials, 277 (2000) 274

[105] K. Tangri, G.I. Williams, Journal of Nuclear Materials, 4 (1961) 226

[106] G. Rousseau et al., Journal of Nuclear Materials, 355 (2006) 10

[107] H. Palancher et al., Powder Diffraction, 28-S2 (2013) 371

[108] R.C. Birtcher, P. Baldo, Nuclear Instruments and Methods in Physics Research B, 242 (2006) 487

[109] J. Gan et al., Journal of Nuclear Materials, 396 (2010) 234

[110] J. Gan et al., Journal of Nuclear Materials, 424 (2012) 43

[111] A. Leenaers et al., Journal of Nuclear Materials, 335 (2004) 39

[112] A.D. Smigelskas, E.O. Kirkendall, Trans. AIME, 171 (1947) 130

[113] E. Perez, Y.H. Sohn, D. Keiser, Metallurgy and Materials Transactions A, 44A (2012) 584

[114] C. Matano, Japanese Journal of Physics, 1933

[115] A.A. Nayeb-Hashemi and J.B. Clark, Phase Diagrams of Binary Magnesium Alloys, 1988

[116] D.D. Keiser et al., *Microstructural analysis of irradiated U-Mo fuel plates: recent results* in proceedings of the 16th Research Reactor Fuel Management (RRFM), Prague, 2012

[117] International Atomic Energy Agency, *Viability of Inert Matrix Fuel in Reducing Plutonium Amounts in Reactors*, IAEA-TECDOC-1516, 2006

[118] R.L. Fleischer, P.B. Price, R.M. Walker, Nuclear Tracks in Solids, Principles and Applications, University of California press, Berkeley, 1975

[119] S.T. Knobeevsky et al., *Some physical properties of uranium, plutonium and their alloys* in proceedings of the 2nd International Conference on the Peaceful Uses of Atomic Energy, Geneva, 1958

[120] A.J. Bradley, Proc. Phys. Soc. 52 (1960) 650

[121] J.A. Alonso, L.J. Gallego, J.A. Simozar, Nuovo Cimento, 12 (1990) 587

[122] B.M. Ditchek, L.H. Schwartz, Ann. Rev. Mater. Sci. 9:219 (1979) 53

[123] G.A. Birzhevoy et al., *Results of post-irradiation examination of the (U-Mo) - Aluminum matrix interaction rate* in proceedings of the 11th Research Reactor Fuel Management (RRFM), Lyons, 2007

[124] D.D. Keiser et al., *Characterization and testing of monolithic RERTR fuel plates* in proceedings of the 11th Research Reactor Fuel Management (RRFM), Lyons, 2007

[125] K. Huang et al., Journal of Phase Equilibria and Diffusion Volume 34, 4 (2013) 307

[126] F.W. Walter, J.R. Parrington, F. Feiner, Nuclides and Isotopes, General Electric Company, 1989

[127] Match! homepage, www.crystalimpact.com/match

[128] ICSD homepage, www.fiz-karlsruhe.de/icsd

[129] A.M. Ammons, Physical Metallurgy of Uranium Alloys, edited by J.J. Burke, D.A. Colling, D.A.Gorum, J. Greenspan, pp. 511-585. Chestnut Hill, MA: Brook Hill

[130] N. E. Golovkina and V.K. Grigorovich, *Behavior of roller and normalized a-U alloys under conditions of thermal cycling* in Physical Chemistry of Alloys and Refractory Compounds of Thorium and Uranium edited by O.S. Ivanov, Keter Press (1972) 24

[131] Linard, M., *Study of Uranium-Titanium Alloys with a Low Titanium Content (0-1.5 Percent) by Weight*, translated from the French for Oak Ridge National Laboratory Tennessee, U.S. Atomic Energy Commission Contract Report No. ORNL-TR-2S79, 1971

[132] D. J. Murphy, Trans. ASM, 50 (1958) 884

[133] D.L. Douglass, Trans. ASM, 53 (1961) 307

[134] W. Hume-Rothery, R.E. Smallman, C.W. Haworth, The Structure of Metals and Alloys, The Institute of Metals, London, 1969

[135] S. Dubois et al., *Development of dispersed UMo fuel : An oxide layer as a protective barrier of the UMo particles* in proceedings of the 28th Reduced Enrichment for Research and Test Reactors (RERTR), Cape Town, 2006

[136] G. Cabane, Journal of Nuclear Materials, 4 (1959) 364

[137] J.F. Jue et al., Journal of Nuclear Materials, 448 (2014) 250

[138] E. Nes, Acta Metall. 20 (1972) 499

[139] T. Ohashi, R. Ichikawa, Metall. Trans, 3A (1972) 2300

[140] G.H. Bannister, J.R. Murry, Journal of Less-Common Metals, 2 (1960) 372

[141] L. Castaldelli, C. Fizzotti, A.G. Gandini, *Transformation Processes in Some Uranium Alloys Low in Molybdenum and Niobium* translated from the Italian for Sandia laboratories, Albuquerque, New Mexico, U. S. Atomic Energy Commission Contract Report No. SC-T-72-2457, 1972

[142] V.B. Kishinevskii, L. I. Gomozov, O.S. Ivanov, *Corrosion Resistance in Water of Some Alloys of Uranium with Zirconium, Niobium and Molybdenum* translated from Russian for University of California, Lawrence Radiation Laborator-y, Livermore, U.S. Atomic Energy Commission Contract Report No. UCRL-Trans-10455, 1970

[143] R.J. van Thyne, D.J. McPherson, Amer. Soc. Metals Transactions 50 (1957) 576

[144] W.M. Justusson, Journal of Nuclear Materials, 4 (1961) 37

[145] J.L. Jorda, R. Flükiger, J. Muller, Journal of Less-Common Metals, 75 (1980) 227

[146] N. Li et al., Journal of Applied Phyics, 105 (2009) 123522

[147] L.K. Walford, Philos Mag., 9 (1964) 513

[148] G.T. Laissardiere, D.N. Manhm, D. Mayou, Progress in Material Science, 50 (2005) 679

[149] H. Niu et al., Scienitific report, 2 (2012) 718

Acknowledgements

This work would not be achieved without the exceptional supports from my supervisors, colleagues, collaboration partners, friends and family:

Own Publications

- **H-Y. Chiang**, R. Jungwirth, T. Zweifel, W. Schmid, W. Petry, F. Kraus, **Interactions between UMo/Al fuel and diffusion barriers Nb and TiN under heavy ion irradiation**, Transactions RERTR 2011, Santiago, Chile

- **H-Y. Chiang**, T. Zweifel, H. Palancher, A. Bonnin, L. Beck, P. Weiser, M. Döblinger, C. Sabathier, R. Jungwirth, W. Petry, **Evidence of amorphous interdiffusion layer in heavy ion irradiated U–8wt%Mo/Al interfaces**, Journal of Nuclear Materials, 440 (2013) 117

- **H-Y. Chiang**, M. Mayer, T Zweifel, R. Jungwirth, W. Petry, **RBS studies on heavy ion irradiation induced diffusion in UMo/Transition metal/Al fuel**, Transactions RRFM 2013, St. Petersburg, Russia

- **H-Y. Chiang**, M. Döblinger, S.-H. Park, L. Beck, W. Petry, **Ion beam induced spinodal decomposition and amorphization in the immiscible bilayer system UMo/Mg**, Journal of Nuclear Materials, 453 (2014) 41

- **H-Y. Chiang**, S.-H. Park, M. Mayer, K. Schmid, M. Balden, U. Boesenberg, R. Jungwirth, G. Falkenberg, T. Zweifel, W. Petry, **Swift heavy ion irradiation induced interactions in the UMo/X/Al trilayer system (X= Ti, Zr, Nb, and Mo)**, Journal of Alloys and Compounds, submitted on 15.7.2014